Report Number 94-31

Research

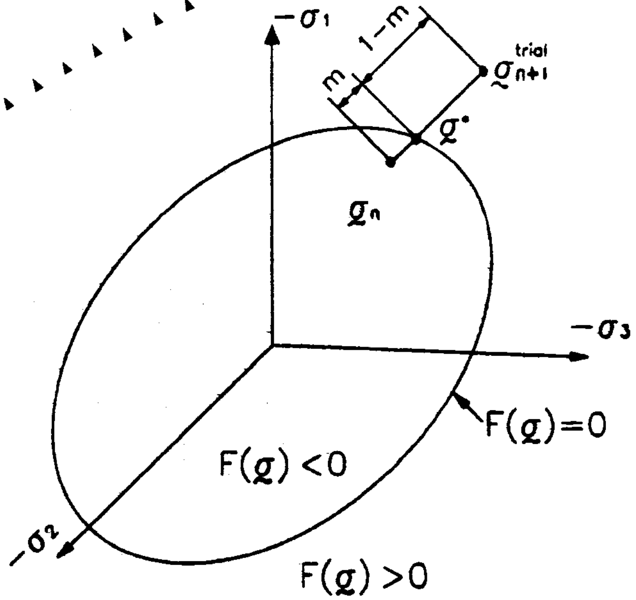

Development of Simulation Software for Modelling Pavement Response at Mn/ROAD

MnROAD
Minnesota Road Research Project

Report Documentation Page

1. Report No.
MN/RC - 94/31

2.

3. Recipient's Accession No.

4. Title and Subtitle
Development and Simulation Software for Modelling Pavement Response at Mn/ROAD

5. Report Date
March 1994

6.

7. Author(s)
Zhonglan Zhang, Henryk K. Stolarski and
David E. Newcomb

8. Performing Organization Report No.

9. Performing Organization Name and Address
Civil & Mineral Engineering Department
University of Minnesota
122 Civil & Mineral Engineering Building
500 Pillsbury Dr. SE
Minneapolis, Mn 55455

10. Project/Task/Work Unit No.

11. Contract(C) or Grant(G) No.
(C) Mn/DOT 69061 TOC #80

12. Sponsoring Organization Name and Address
Minnesota Department of Transportation
Office of Research Administration
200 Ford Building-Mail Stop 330
117 University Avenue
St. Paul, Mn. 55155

13. Type of Report and Period Covered
Final Report

14. Sponsoring Agency Code

15. Supplementary Notes

16. Abstract (Limit: 200 words)

This report presents the development of simulation software for modelling dynamically loaded pavement response. The analysis is carried out by employing the finite element method and by integrating the resulting discrete equations of motion through the central difference method. The lower pavement layers (base, subbase and subgrade) are assumed to be elasto-plastic and are described by using the flow theory of plasticity. The mapped infinite elements are used instead of viscous boundaries to mitigate the wave reflection from the boundaries of the model. The predicted pavement responses are compared with the experimental results obtained by a Falling-Weight Deflectometer (FWD). Dowel bar load transfer mechanism is also analyzed.

17. Document Analysis/Descriptors
Finite Element Method
Elasto-Plastic Materials
Infinite Elements
Pavement Models
Dynamic Loads
Dowel Bars
FWD Test Results
Drucker-Prager Yield Function
Perfectly Plastic Material
Central Difference Method
Pavement Response

18. Availability Statement
No restrictions. This document is available through the National Technical Information Services, Springfield, Va. 22161

19. Security Class (this report)
Unclassified

20. Security Class (this page)
Unclassified

21. No. of Pages
133

22. Price

DEVELOPMENT OF SIMULATION SOFTWARE FOR MODELLING PAVEMENT RESPONSE AT Mn/ROAD

Final Report

Prepared by

Zhonglan Zhang
Research Assistant

Henryk K. Stolarski
Associate Professor

and

David E. Newcomb
Associate Professor

University of Minnesota
Department of Civil and Mineral Engineering

Submitted to

Minnesota Department of Transportation
Office of Research Administration
200 Ford Building, 117 University Avenue
St. Paul, MN 55155

March, 1994

ACKNOWLEDGEMENT

Support of the Minnesota Department of Transportation is gratefully acknowledged.

SUMMARY

A study was undertaken to develop simulation models for pavement systems by the finite element method. Two separate models were developed. One model was called MNROAD-93 and was designed assuming a continuous pavement surface. The lower pavement layers (base, subbase and subgrade) were treated as elasto-plastic materials by using the flow theory of plasticity. The material may be assumed as either perfectly plastic or isotropically work-hardening. Mapped infinite elements were used as boundaries to mitigate the wave reflection from the boundaries of the model. Singly, doubly and triply infinite elements were generated to simulate the half-space by which the pavement structure was best modelled.

Another model, called MNSLAB, was specifically designed to model rigid pavements. This is a two-dimensional, linear elastic, dynamic model treating the pavement slab as a plate on elastic foundation.

The results obtained from MNROAD-93 were compared with FWD test data, and the results from MNSLAB were compared with the results from other models. For the MNROAD-93 model among all combinations of linear elastic and elasto-plastic material, and viscous boundaries and infinite element boundaries, there was no single combination which would provide the consistently good results for problems discussed in this report. However, the infinite element boundaries provided better agreement with experiments than viscous boundaries.

For the MNSLAB model, in addition to accurate material properties, the key aspect is proper formulation of the dowel bar stiffness matrix. In the past, this has been done by treating the imbedded in concrete part of the dowel as semi-infinite beam on elastic foundation. No such assumptions were made in the present research and the dowel-slab interaction was modelled realistically by using the finite element method. To further improve the results, incorporation of the aggregate interlock may be necessary in the future. Also another time integration method should be considered and possibly should replace the central difference method to allow for a longer time step and to reduce the computer time. Many other modifications can be made in the future in order to improve MNSLAB capabilities; they may include moisture effects, variable subgrade support conditions, etc.

TABLE OF CONTENTS

APPENDIX

LIST OF TABLES

LIST OF FIGURES

LIST OF SYMBOLS

A	cross section area
$\underset{\sim}{B}$	standard B matrix which relates strains and displacements
$\underset{\sim}{B_b}$	bending B matrix
$\underset{\sim}{B_s}$	shear B matrix
C	space between dowel bars (30 cm) or cohesion
$\underset{\sim}{C}$	damping coefficient matrix (diagonal)
$\underset{\sim}{d}$	displacement vector
$\underset{\sim}{\dot{d}}$	velocity vector
$\underset{\sim}{\ddot{d}}$	acceleration vector
$\underset{\sim}{D}$	constitutive matrix representing material properties
e^p	effective plastic strain
E	Young's modulus
$\underset{\sim}{f}^{int}(\underset{\sim}{d})$	nodal internal force vector
$\underset{\sim}{f}^{ext}(t)$	applied external force vector
F	yield function or vertical force
G	shear modulus
h	thickness of the slab
H	plastic modulus

I	moment of inertia
I_1	first invariant of stress tensor
J_2	second invariant of deviatoric stress tensor
k	composite modulus of subgrade reaction
k_1, k_2	material constant
k_R	resilient modulus of subgrade reaction
$\underset{\sim}{K}$	element stiffness matrix
$\underset{\sim}{K_b}$	bending stiffness matrix
$\underset{\sim}{K_s}$	transverse shear stiffness matrix
$\underset{\sim}{K_f}$	stiffness matrix of the elastic foundation
L	element length
M	moment
$\underset{\sim}{M}$	mass matrix (diagonal)
M_1, $M_2 \ldots M_8$	mapping function
N_1, $N_2 \ldots N_8$	standard shape function
$\underset{\sim}{N}$	shape function matrix
$u(x,y,z)$	displacement in x direction
U	strain energy
$U(x,y)$	displacement in x direction
$v(x,y,z)$	displacement in y direction

$V(x,y)$	displacement in y direction
V_1, V_2, V_3	displacement
$w(x,y,z)$	displacement in z direction
$W(x,y)$	displacement in z direction
α	material constant
$\gamma,\ \gamma_x,\ \gamma_y$	transverse shear strain
$\underset{\sim}{\epsilon}$	strain vector
$\underset{\sim}{\epsilon}^{e}$	elastic strain vector
$\underset{\sim}{\epsilon}^{p}$	plastic strain vector
ζ	local coordinate
η	local coordinate
θ	first stress invariant or rotation
$\theta_1,\ \theta_2,\ \theta_3$	rotation of dowel bar element
$\theta_x,\ \theta_y$	rotation of slab
κ	material constant or curvature
κ_0	material constant
$\kappa_x,\ \kappa_y,\ \kappa_{xy}$	curvature
λ	positive scalar factor of proportionality
ν	Possion's ratio
ξ	local coordinate

ρ	mass density
$\underset{\sim}{\sigma}$	stress vector
σ_3	minor principal stress
σ_d	stress difference
$\underset{\sim}{\sigma}^*$	stress vector which is on the yield surface
ϕ	internal friction
ω	lateral displacement
Δ	increment
Ω	element domain

CHAPTER 1

INTRODUCTION

MOTIVATION

The complexity of the analysis and design of pavement structures can be attributed to many factors. They include dynamic and stochastic loadings, heterogeneous (layered) materials with complex mechanistic responses, changing environmental conditions (temperature, moisture), etc. Under such diverse and complex conditions neither an experimental nor analytical approach alone is capable of providing the designer with sufficient capabilities to predict pavement performance. This was particularly so before widespread use of computers when the potential for significant calculations and the collection and processing of experimental data were rather limited. As a result, until recently, the design process was based mainly on the experience accumulated over many years of observations. Recent development of powerful computers enhanced the capabilities of gathering and processing experimental data as well as opened new opportunities for more realistic, complex calculations. As a results the design process can now be made more rational.

Recognizing the situation described above, Minnesota Department of Transportation (Mn/DOT) constructed a very large experimental facility (called Mn/ROAD and described more extensively below) and, at the same time, is interested in parallel analytical studies of pavement structures. Such an attitude reflects the need for a coordinated dual approach (experimental and analytical) necessitated by the complexity of pavements. This report describes some research on the analytical side of this effort. However, to put this analysis in proper context, a short description of the experimental facility Mn/ROAD is presented next.

Mn/ROAD

Mn/ROAD (Minnesota Road Research Project) is a pavement technology test facility constructed by the Minnesota Department of Transportation. It is located parallel to I-94 in Wright County approximately 60 km (40 miles) northwest of the Twin Cities. The major research objectives of this project include verifying existing pavement design models, analyzing factors that affect pavement performance, developing new design models and intensively analyzing instrumentation. There are 40 pavement test sections, each test section is approximately 150 m (500 feet) in length with transitions separating the sections. The sections have several pavement designs consisting of a variety of thicknesses and materials for testing of various factors. Each test section is monitored by an extensive network of sensors tied to a central database system. Sensors located within each pavement structure layer measure and record load response parameters such as strain, deflection and pressure.

Basic Philosophy of The Present Research

The experimental data collected at the Mn/ROAD facility are primarily to enrich the understanding of the behavior of pavement structures. The understanding of that behavior leads to analytical models, allowing for reasonably accurate predictions of the response with limited experimental input. Only when this level of understanding is reached can experimental and analytical tools be of real use in the design process. To reach that level, however, an initial analytical model has to be developed based on available information and subsequently improved as new data and new insight become available.

As the models in this report were being developed, the Mn/ROAD project was in the construction phase and much data was not available for comparison. However, considering that the pavement at Mn/ROAD are tested under normal traffic conditions, it is clear that the collected data will reflect real dynamic loading effects, real material properties and the actual design of the pavement. Thus, comparison of the tests with analytical results could only be meaningful if those basic features of the experimental conditions were accounted for in the analysis. Thus, the basic premise of this project was to consider dynamic effects, more realistic material behavior and some features of the actual pavement design. Among existing analytical models (reviewed later in this report), the majority of them deal with static loading conditions. Those few dealing with dynamic situations were developed under very particular assumptions, too restrictive to relate to the conditions existing in Mn/ROAD. Thus, it was decided that computer programs should be developed to analyze dynamically loaded pavement structures allowing for inelastic properties of material in flexible pavements and better describing the dowel bar load transfer mechanism in rigid pavements. The methods used to describe the above features have been known for some time, but they do not seem to have been used in the context of the pavement analysis.

The choice of the basic features (emphasized in the previous paragraph) incorporated in this research is justified below. They seem to reflect the dominant characteristics of the experimental environment, and this should lead to a meaningful comparison of the measurements at Mn/ROAD. It should be emphasized however that many features present at the Mn/ROAD facility (such as environmental conditions, random heterogeneity of the subgrade and even all characteristics of the materials used) are not incorporated in these calculations. As a result some discrepancy between calculations and experiments should be expected. Further improvements are possible in the future, but they are beyond the scope of this specific project. Nevertheless, it is fair to say that, even with many additional improvements, full agreement between experiments and numerical results is impossible for a system as complex as pavements.

To justify the emphasis on inelasticity we note that pavement systems inherently incorporate materials which may exhibit significant inelastic (nonlinear) behavior. Proper understanding and analysis of inelastic behavior, particularly under dynamic conditions, might lead to better designs in which occurrence of prohibitively large permanent distortions in the pavement would be significantly delayed.

The effects of dynamic loads on the mechanical response of pavement structures are invariably more critical than those of static loads. For a given load intensity both the stresses and strains experienced by a structure are usually higher in the dynamic case than in the static case. It may be advantageous to include dynamic effects in the analysis and design process in which stresses or strains affect engineering conclusions and design parameters. These quantities can be effectively obtained by means of numerical simulation. The usual method of accounting for the effects of dynamic loading is based on the static analysis with an "adequately" magnified static load. While this could be justified for materially homogeneous, linearly elastic structural problems, it is more difficult to find similar justification for nonlinear problems with clearly identifiable layers of different materials, such as pavements. Waves reflecting from the interfaces between the layers may superpose to give localized areas of high stress and strain intensity. These effects are not defined in static analyses. Simulating dynamic loads by considering only the static case with a magnified load level may not be adequate.

Another important approach which could answer many questions related to dynamic loading is experimentation, and numerical simulations (finite element method) can greatly assist experiments. They are less expensive and time-consuming than experiments and are more appropriate to use for various parametric studies. One can therefore envision the situation in which a small number of viable solutions is first selected by numerical simulations from a bigger class of possibilities and then the experimental investigations are restricted only to a small, select group.

The determination of stresses and deflections in rigid pavements that have joints and/or cracks has been a subject of major concern for many years. Originally, the analytical solutions are based on the assumptions that the pavement has an infinite length and that the loading is static, they cannot be used for the analysis of jointed or cracked concrete slabs with dynamic load. More recently, with the advent of high-speed computers, the powerful finite element method of analysis has been used to analyze the behavior of discontinuous pavements. Various models have been developed for analyzing rigid pavement systems by using finite element modeling techniques. However, few dynamic programs have been developed to incorporate the modeling of joints that have load transfer systems.

OBJECTIVES

The main goal of this project is to provide analytical tools for predicting stresses and strains in the pavement structures under conditions resembling those in Mn/ROAD. Those quantities (stresses and strains) are principal data used in the design process. Further improvement in the approach alleviating discrepancies between filed test results and those obtain in this initial analytical study, could be incorporated in the future.

Considering the complexity of the pavement structures, the only possible choice for the analytical study is numerical modelling. In this project the finite element method has been selected. The method consists in dividing the volume of the pavement structure into smaller pieces (called elements), approximating the unknown displacements in each element and matching these approximations between different elements. As a result the behavior of the entire system is described by motion of the selected finite number of points. This motion is described by a coupled system of ordinary differential equations (see Appendix A).

One of the difficulties associated with modelling of pavement structures is caused by the fact that subgrade, which is a part of the system, extends to infinity. To have a finite number of unknowns two options are available. First, one can only analyze a finite region, encompassing an area far enough from the loading point to assume that the effects of this truncation of the volume is negligible. Second, one can use elements that extend from some fixed location in space to infinity and thus, one can cover the actual infinite volume of the pavement system. While neither of these two options cause problems in static analysis, in dynamic cases the first approach is associated with some difficulties dealing with the propagation of waves caused by dynamic loads and by the reflection of those waves from the boundaries of the truncated volume of the pavement systems. These reflected waves are spurious since it is only the computational model that has the boundary at the location of the truncation, not the actual system. The reflected waves come back to the analyzed volume and pollute the results. To mitigate such wave reflections special viscous absorbers are often introduced at the truncated boundary. Their description needs special parameters which to some extent can be determined rationally, but even then some wave reflection still takes place. A more natural approach seems to be the one using infinite elements, which eliminate the artificial boundaries altogether. However, it is unclear how infinite elements would handle dynamic situations, since no results concerning this has been identified in the literature.

In view of the situation described above the principal objectives of this research are as follow. In the past a finite element program MNROAD [Prakasha, 1990] was developed to analyze three-dimensional, linear elastic, layered pavement structures under dynamic loads with viscous boundaries. The first objective of this research project was to modify the existing program MNROAD to calculate the displacements and stresses of pavement systems considering base, subbase and subgrade as elasto-plastic materials. The second objective was to use infinite elements as boundaries instead of viscous boundaries. The modified program incorporating the above two tasks is called MNROAD-93. The predicted pavement responses will be compared with the FWD (Falling-Weight Deflectometer) results. Finally, the third objective was to develop a two-dimensional, linear elastic, dynamic model to simulate the load transfer mechanism of rigid pavements. To accomplish this, the finite element program MNSLAB was written.

Details of analysis and further explanation of various terms can be found in the Appendices.

SCOPE

The research presented in this report treats the materials in the lower layers (base, subbase and subgrade) of the pavement as elasto-plastic materials by using flow theory of plasticity with Drucker-Prager yield function (see Appendix B). The associated flow rule is used. The materials may be assumed to be perfectly plastic or isotropically work-hardening. The strain softening characteristic of soils can also be simulated. It is known that some geological materials do not obey the associated flow rule. This feature can be easily incorporated if a need of that kind emerges.

The mapped infinite elements are used instead of viscous boundaries to eliminate the wave reflection from the boundaries of the model (see Appendix C). The singly, doubly and triply infinite elements that are elements extending to infinity in only one, two or all three spacial directions are generated to simulate the half-space by which the pavement structure is best modelled.

This research also provides a simple dynamic model for rigid pavement structures. This model focuses on modelling of the load transfer mechanism. It consists of 9-node Lagrangian plate elements. Only one layer (slab) can be modelled. The subbase and subgrade are considered as a Winkler foundation with a composite modulus of subgrade reaction, k. The whole finite element model for analysis of rigid pavement structures consists of the following two submodels: (1) concrete slabs connected by dowel bars dynamic model and (2) dowel bar and slab static interaction analysis model. The details are provided in the Appendix D.

CHAPTER 2

REVIEW OF PREVIOUS WORK

LITERATURE REVIEW

Finite Element Method

The finite element method has been successfully applied to many engineering problems. The finite element analysis [Duncan et al., 1968; Thompson, 1982; Hoffman and Thompson,1982] of a pavement system began by dividing the pavement structure into many small axisymmetric finite elements as shown in Figure 2.1. The element stiffness matrix and nodal forces are calculated by assuming displacement variations within the element along with a knowledge of stress-strain behavior of the element material. The response of each individual element influences (and is influenced by) the responses of surrounding elements. Equilibrium of the whole model is expressed by means of the principle of virtual work. These equations are used to solve for the unknown displacements. Once the displacements of all the nodal points have been calculated, the stresses and strains for each element can be readily obtained from constitutive and kinematic relationships. Detailed descriptions of the finite element method and its applications to a wide variety of problems are contained in a number of publications [Bathe, 1982; Hughes, 1987; Owen and Hinton, 1980; Cook et al., 1989].

The finite element method offers a means of solving practical problems by numerical techniques. An analytical procedure of that type provides a very powerful tool for determining the mechanical behavior of a pavement structure because of modeling flexibility. With sufficient attention devoted to determination of appropriate physical property values and simulation of

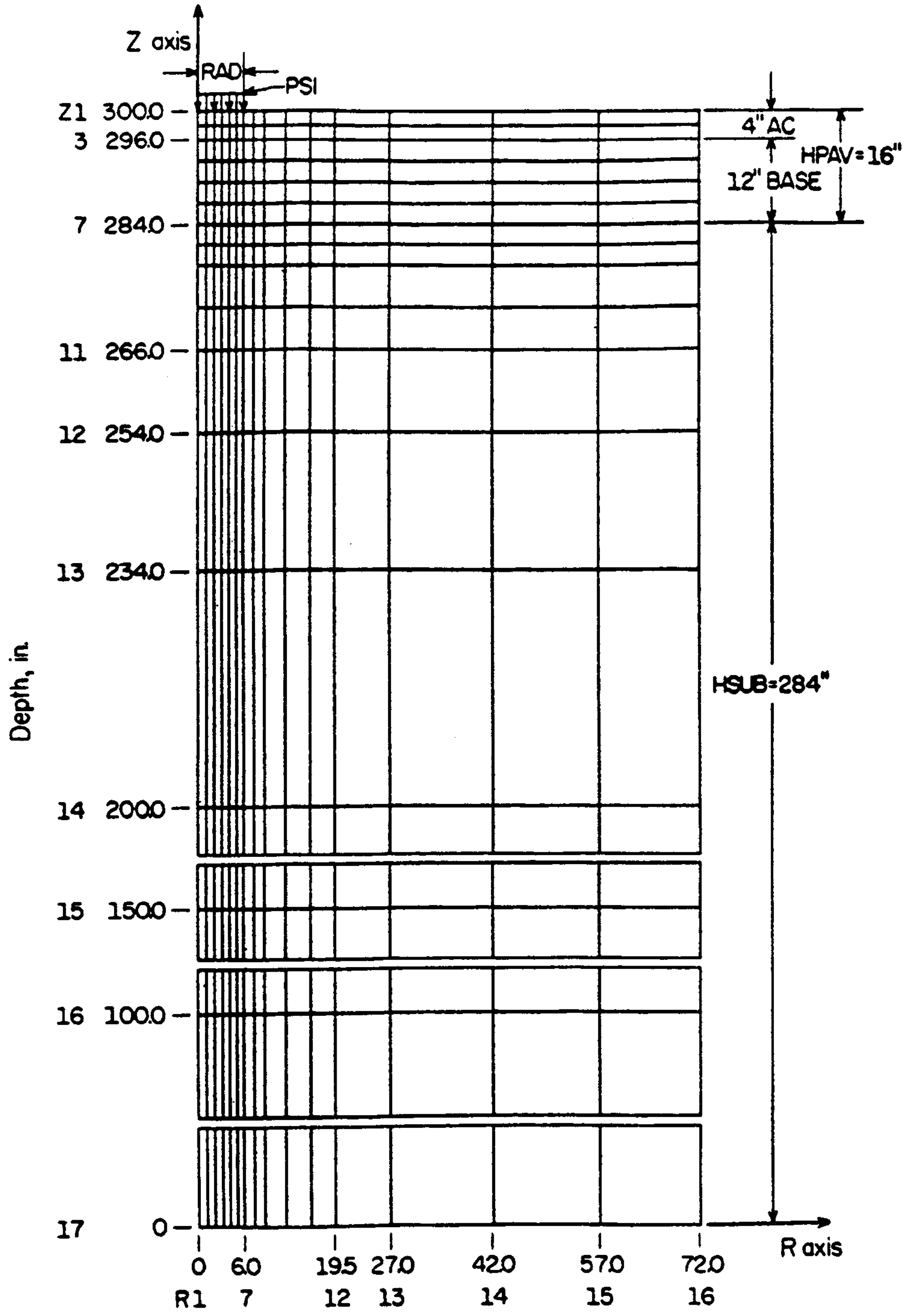

Figure 2.1. Finite element configuration (ILLI-PAVE)

[after Thompson,1982].

actual boundary and loading conditions, the finite element method promises to afford improved understanding of the behavior of pavement structures under load. The finite element method is preferred since it offers four major advantages. First, dynamic analysis of pavement structures can be modelled. Second, non-linear elastic or any other material behavior such as viscoelastic, viscoplastic or elasto-plastic can be incorporated. Third, the practical boundary conditions can be modelled. Fourth, the types of applied surface loadings may be varied to include vertical, horizontal, flexible and rigid loading (flexible loading means that the pressure is distributed uniformly under the load, while rigid loading means that the displacements are uniform under the load).

In 1967, A. Waterhouse presented the first finite element program for the analysis of pavement structure [Hoffman and Thompson, 1982; Prakasha, 1990]. It is an axisymmetric model and can incorporate any number of layers which are assumed to be linear elastic. The pavement structure is divided into a number of axisymmetric triangular elements.

Flexible Pavement Analysis Models

Early computer programs for mechanistic analysis (such as CHEV5L, BISAR, ELSYM5, etc.) [Hicks et al., 1978], which are analytical programs, were developed for linear elastic analysis considering only static loading. In these programs each pavement layer is assumed to extend infinitely in the horizontal direction and the three-dimensional problem is reduced to an axisymmetric two-dimensional problem. The superposition principle is used to consider the effects of multiple loads. The main drawbacks of these linear elastic layer programs are that they cannot model nonlinear resilient behavior of the materials and dynamic loading and they may yield tensile stresses in granular material which cannot physically occur [Harichandran et al.,1990].

WIL67 is a linear elastic, static, axisymmetric finite element model [Raman, 1972]. The model is shown in Figure 2.2. The pavement structure is divided into a number of prismatic 4-node quadrilateral elements. All the nodes on the boundary (except the two bottom corner nodes) are restrained against moving in a direction perpendicular to the boundary. The two bottom corner nodes are completely restrained.

The finite element program ILLI-PAVE is based on the code initially developed by E.L. Wilson [1965]. It was modified and/or adapted by Barksdale [1969]; Duncan, Monismith, and Wilson [1968]; the research staff of the Construction Engineering Laboratory at Champaign, Illinois; and Hoffman and Thompson of the University of Illinois [Thompson, 1982]. The plane radial section is shown as a meshed rectangular half-space in Figure 2.3. The boundary conditions of this analysis are such that the inner and outer vertical boundaries can move only in the vertical. The lower boundary can move neither vertically nor horizontally. The loading condition can be specified in terms of surface contact pressure and radius of loaded area. The loading is of the "flexible plate" type and only one load can be accommodated. It can incorporate both nonlinear and linear stress-strain behavior of component pavement materials. Four different material models are available [Thompson, 1982], which are

1. Materials with elastic modulus as a function of minor principal stress, σ_3.
2. Materials with modulus as a function of stress difference, σ_d.
3. Materials with constant modulus, i.e., linear elastic materials.
4. Materials with modulus as a function of the first stress invariant, θ.

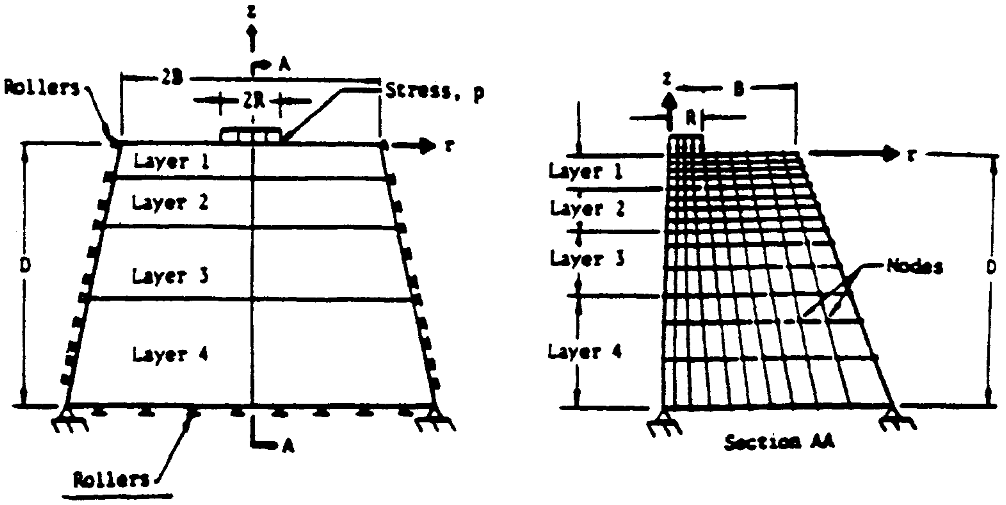

Figure 2.2. Finite element idealization of pavement system (WIL67 code) [after Kumar, 1986].

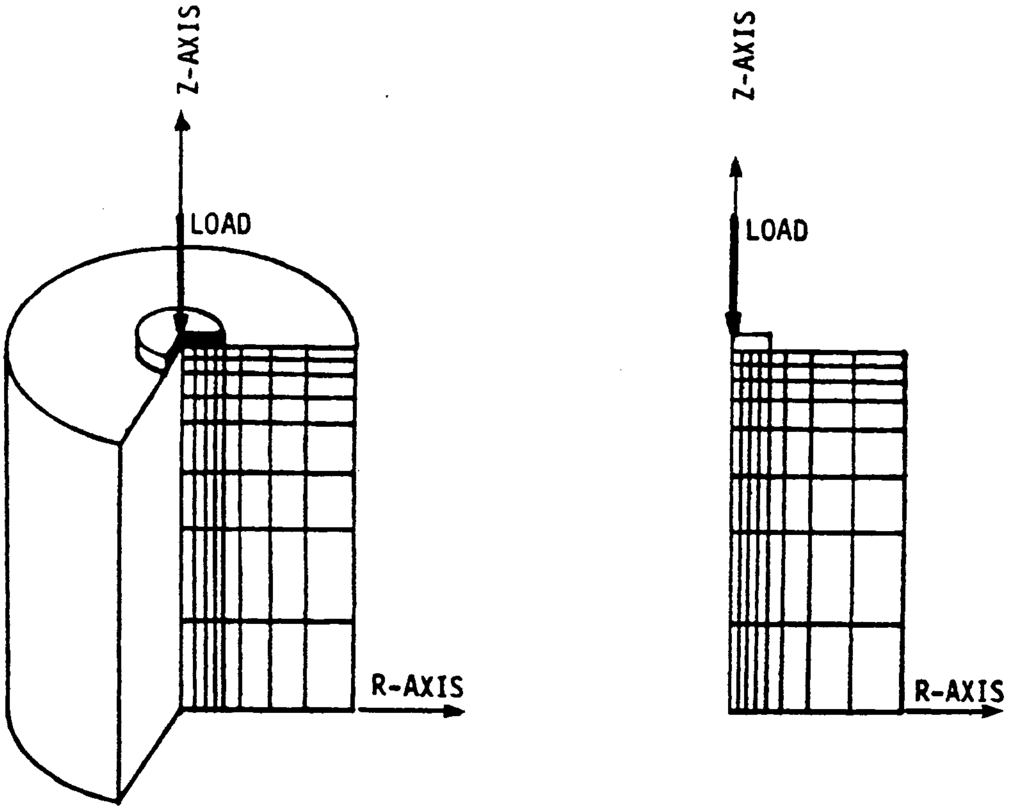

(a)

(b)

Figure 2.3. ILLI-PAVE model, (a) Cylindrical pavement configuration; (b) Rectangular half space of an axisymmetric solid [after Thompson,1982].

In 1986, Kumar presented a paper on the analysis of flexible pavements using finite and infinite elements [Kumar, 1986]. He analyzed an axisymmetric, static model like ILLI-PAVE. He improved the model by using infinite elements at the boundaries. This gives more accurate results and the results are very close to analytical results. It consumes less computer time since the number of elements required to achieve reasonable accuracy is reduced. Kumar assumed the materials in each layer to be isotropic, homogeneous and linear elastic.

MICH-PAVE [Harichandran et al., 1990] which was developed by Michigan State University for the Michigan Department of Transportation (MDOT) is a nonlinear finite element program for analysis of flexible pavements. The program has three major features. First, it utilizes a newly developed flexible boundary concept for pavement analysis. Second, it uses performance models for the prediction of fatigue life and rut depth. Third, it is "user-friendly". The resilient modulus model was chosen to represent a nonlinear material. The resilient modulus model characterizes the resilient stress-strain properties of soils through a stress-dependent modulus and a constant Poisson's ratio. The Mohr-Coulomb failure criterion is used to modify the principal stresses of each element in granular layers and roadbed soil after each iteration so as not to exceed the Mohr-Coulomb failure envelope. Thompson used this algorithm in the ILLI-PAVE program. A similar algorithm was developed for MICH-PAVE. A flexible boundary, which accounts for displacements that occur beneath it, is used with finite elements above it [Harichandran et al., 1988].

ABAQUS, a three-dimensional, dynamic finite element program (3D-DFEM), has the capability to simulate actual pavement loading conditions (moving loads at various speeds). ABAQUS developed by Hibbitt, Karlsson and Sorensen, Inc. [1989] was used to analyze flexible pavements by Zaghloul and White [1993]. A number of material models were used to represent actual material characteristics. Asphalt mixtures were modeled as viscoelastic materials. Granular material, which could consist of base course, subbase, and subgrade in some cases, were modeled using the Drucker-Prager model. The Cam-Clay model was used for clays.

Concrete Pavement Analysis Models

Considerable effort has been devoted to the representation of rigid pavement structures with finite elements in the last 20 years. A number of programs have been developed to model the response of rigid pavements with different features and degrees of sophistication. There are 19 analysis and design models reviewed in the reference book by Mueller et al., [1990].

ILLI-SLAB is a two-dimensional finite element program, based on medium-thick plate theory, developed at the University of Illinois in 1977 [Tabatabaie and Barenberg, 1978]. ILLI-SLAB was modified continually. The most important modification in 1984 was the incorporation through an iterative procedure of the deflection-dependent resilient modulus of subgrade reaction k_R [Ioannides et al., 1984]. In 1991, ILLI-SLAB was modified to generate influence functions, which are combined with the dynamic loads under the wheels of a truck to predict the strain time histories at points of interest in the pavement [Nasim et al., 1991]. ILLI-SLAB is a static model, it was modified to calculate influence functions by adding a subroutine that runs the model sequentially with a unit load applied at each point along a defined wheelpath.

ILLI-SLAB has many capabilities and also has some limitations [Mueller, et al., 1990]. Various types of load transfer systems, such as keyways, dowel bars, aggregate interlock, or a combination of dowels and aggregate interlock can be considered at joints and cracks.

Nonuniformly-spaced dowel configurations may be considered. A second pavement layer such as an overlay (bonded and unbounded) or a base course layer may be modeled. However, a maximum of only two pavement layers in addition to the subgrade can be modeled. A combination of slabs such as multiple traffic lanes, traffic lanes and shoulders (with or without tie bars), or a series of transverse cracks may be modeled. Variable subgrade support conditions including complete loss of support at any location or combination of locations beneath the slab may be considered. Four distinct subgrade models, which include Winkler (dense liquid), Vlasov (two-parameter system), Boussinesq (elastic solid), and the resilient subgrade formulation, may be specified. A linear thermal gradient may be modeled to examine slab curling stresses. But moisture effects and the drainability of the pavement section are not considered.

Other programs [Tabatabaie and Barenberg, 1978; Huang and Wang, 1973; Chou, 1980; Tie et al., 1987; Tayabji and Colley, 1986], most being functionally similar to the ILLI-SLAB program, have been developed.

PMARP (Purdue Model for Analysis of Rigid Pavement) [Larralde, 1985; Kopperman, et al., 1986] is an iterative, nonlinear finite element program used to analyze reinforced or unreinforced jointed concrete pavements. The procedure, developed at Purdue University, is based on modifications of the ILLI-SLAB program to include a fatigue damage model.

RISC [Heinrichs, et al., 1989; Majidzadeh et al., 1984] is a computer program developed by Resource International. The program couples a finite element slab model, employing the theory of a flat thin elastic shell, with an elastic solid foundation of up to three discrete layers.

The three-dimensional finite element program GEOSYS [Ioannides and Donnelly, 1988] can be used to analyze flexible and rigid pavements. GEOSYS was originally developed in the early 1970s by a group of engineers, members of the technical staff of Agbabian Associates, in El Segundo, California. The linear, isoparametric, three-dimensional hexahedral brick element was employed. This element occupied prismatic, three-dimensional part of the volume of the pavement has eight nodes located at the vertices of that volume with three degrees of freedom per node and uses linear approximating functions of x, y, and z. The materials were considered as linear elastic. The term "isoparametric" means "same parameters" and it means that displacements and coordinates can be interpolated from nodal values. The typical three-dimensional finite element mesh is shown in Figure 2.4.

PREVIOUS WORK AT THE UNIVERSITY OF MINNESOTA

MNROAD [Prakasha, 1990] is a three-dimensional, linear elastic, static-dynamic finite element program for pavements (Figure 2.5), which was developed by Prakasha, K.S. at the University of Minnesota and funded by the Minnesota Department of Transportation. The model consists of tri-linear, eight-node brick elements. The program, based on input data, can automatically discretize the domain using the principle of isoparametric mapping. All the layers in the pavement structures are assumed to be linear elastic. Dashpots are provided at the boundaries of the finite mesh to absorb the waves caused by the dynamic loads, i.e, to simulate silent (or absorbing, or transmitting) boundaries. The analysis is carried out by solving the dynamic equilibrium equation through the central difference method which is an explicit integration procedure. The force equilibrium equations are solved to find the displacements, which in turn are used to calculate the stresses and strains.

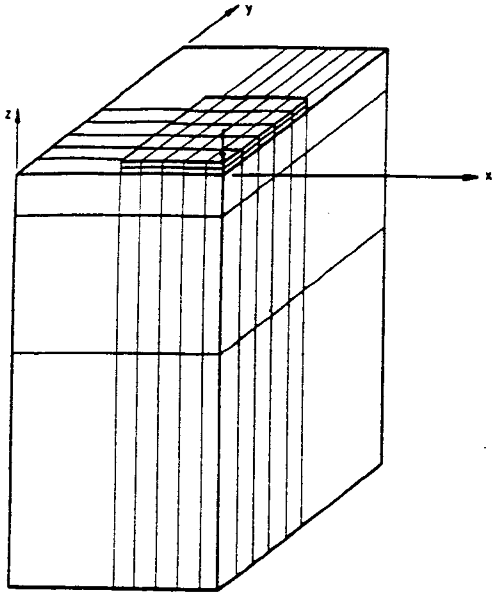

Figure 2.4. Typical 3-dimensional finite element mesh [after Ioannides and Donnelly, 1988].

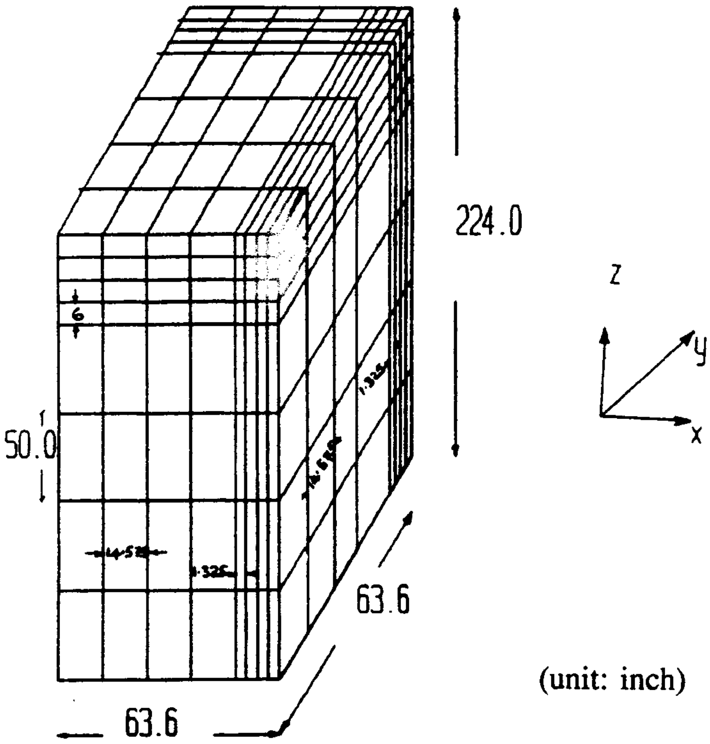

Figure 2.5. Model configuration [after Prakasha, 1990].

CHAPTER 3

PROGRAM DESCRIPTIONS

PROGRAM MNROAD-93 DESCRIPTION

Introduction

The program MNROAD-93 is capable of solving static and dynamic problems. The lower pavement layers can be considered as either linear elastic or elasto-plastic material. The boundary conditions can be treated as either viscous boundaries or infinite element boundaries. It can solve three-dimensional problems only, and is not suitable to solve two-dimensional problems. It is not capable of solving axi-symmetric problems. So far, it can only be compiled, linked and executed in the CRAY systems (supercomputer).

Program MNROAD-93 Structure

The source code of the program MNROAD-93 is about 3800 lines in Fortran 77. The program structure is illustrated in Figure 3.1. This program takes the data from the input file supplied by user and returns the displacements and stresses. The input file includes the basic data required for the mesh generation, external applied loads, boundary condition data and material property data. This gives user the maximum flexibility in using this program. There is no system of units assumed by the program. Rather, it is the user's responsibility to specify data in the consistent units of his or her choice.

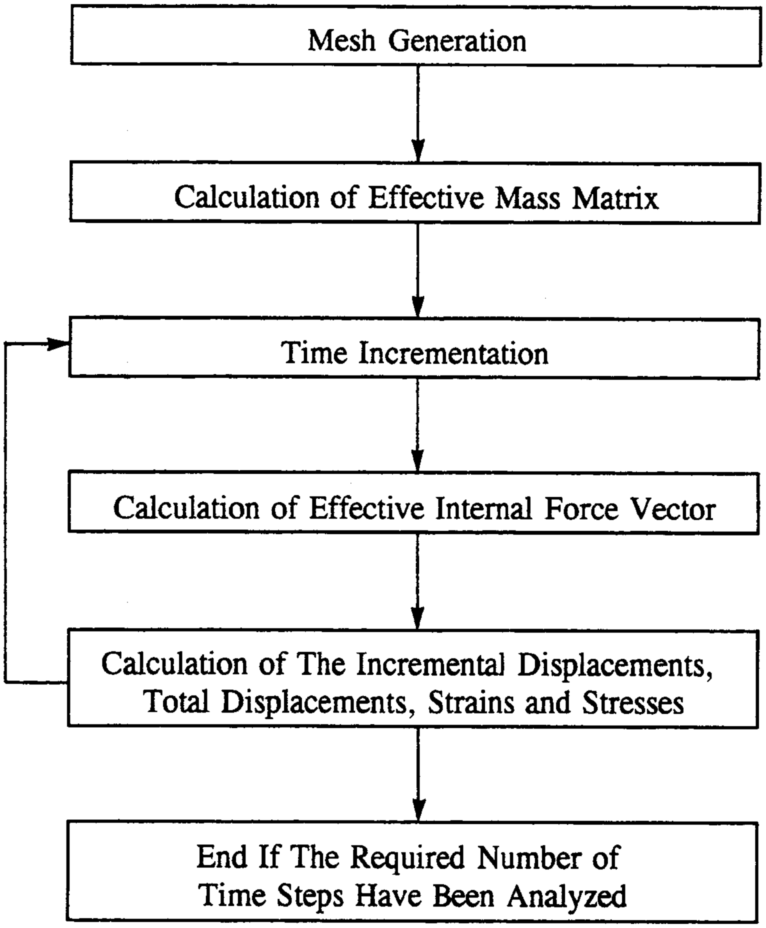

Figure 3.1. Flow chart for the program MNROAD-93.

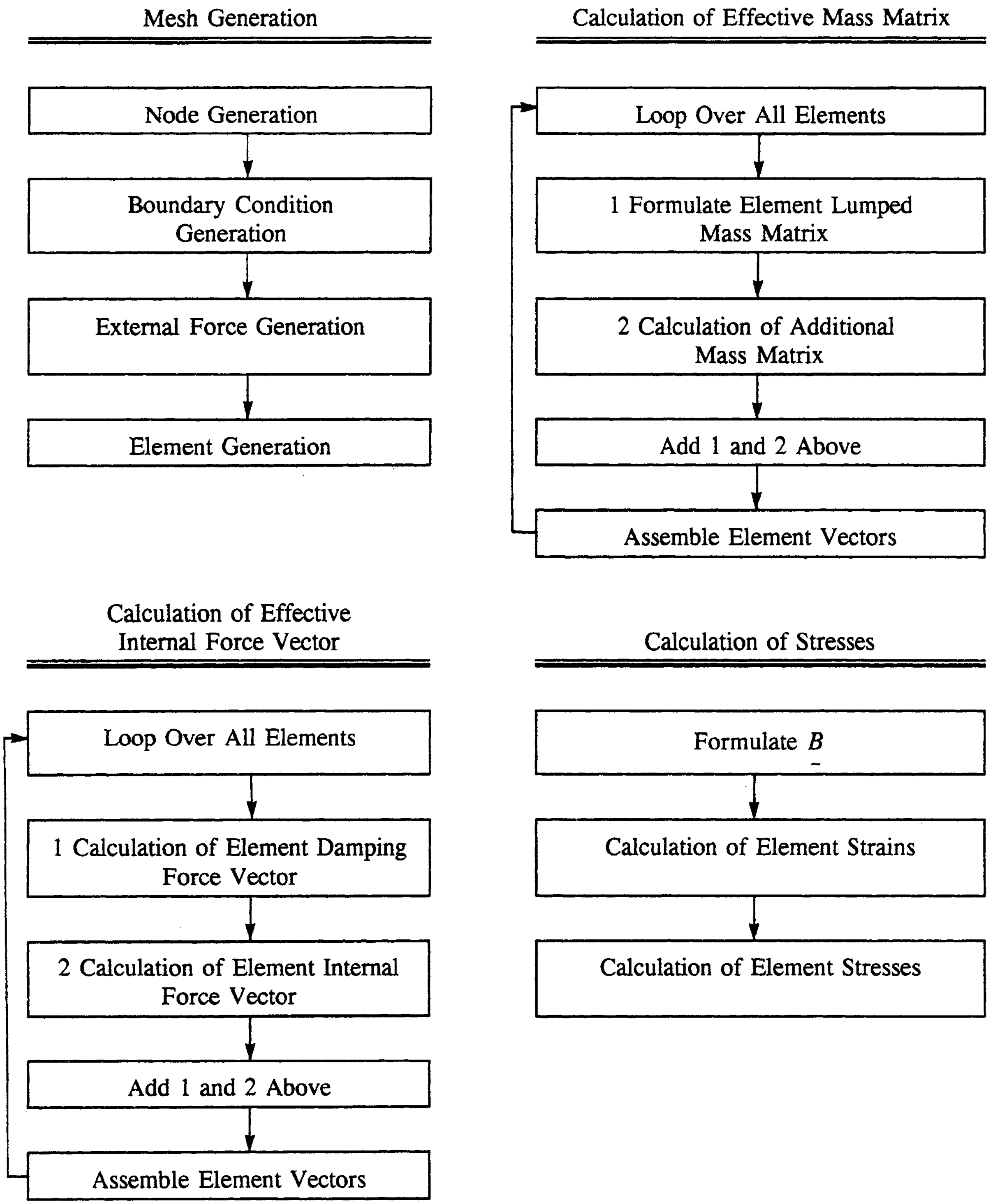

Figure 3.1. Flow chart (continued).

Model Configuration

The pavement structure is modelled as a three-dimensional pavement domain. Finite element discretization is introduced by using 8-node brick elements (Figure 3.2). It is recommend to keep the boundary surfaces (except bottom) vertical. For determining the model size, the criteria developed experimentally by Duncan, Monismith and Wilson [1968], which is suitable for both static and dynamic models, is recommended. These recommendations are:

1. The depth (vertical) to width (horizontal) ratio of the elements should not exceed 5 to 1.
2. The lower boundary should be placed at least at an approximate depth of 50 times the width of the applied load.
3. The outside boundary should be specified at a minimum distance of 12 widths of the applied load.

Program Structure of Elasto-plastic Material Model

The subroutine "STRCAL" in the original program MNROAD is used to calculate the stresses and strains of each element. In order to model the elasto-plastic material, the subroutine "STRCAL" needs to be modified and some elasto-plastic material properties need to be added in the input data.

Program Implementation for Infinite Element Boundaries

To simulate the infinite elements, there is nothing to be changed in the input data, i.e., the mesh, the number of nodes, the number of elements and the connectivity of elements etc. are same as in MNROAD. For the infinite element boundaries model (Figure 3.3), the

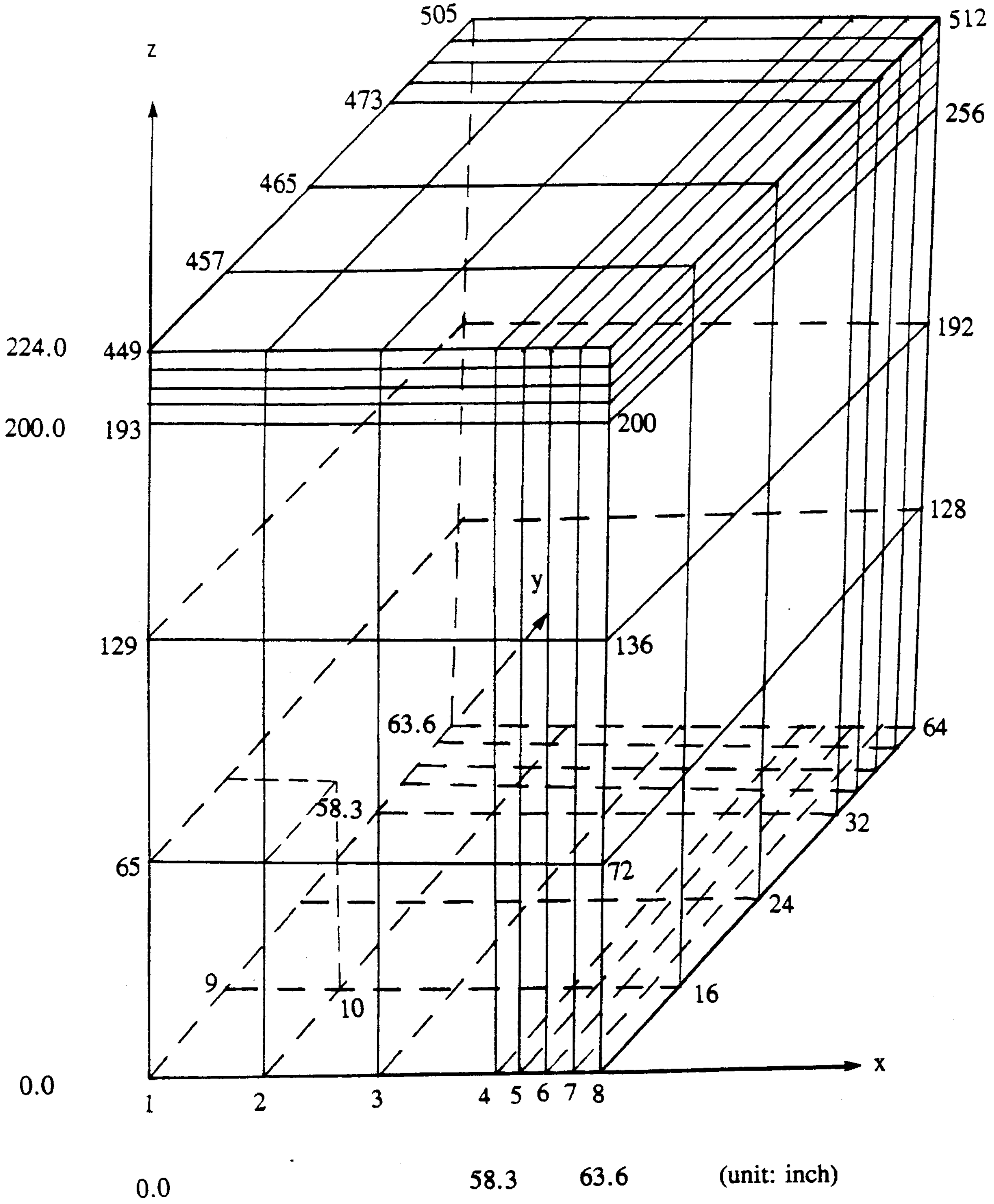

Figure 3.2. MNROAD-93 model mesh configuration.

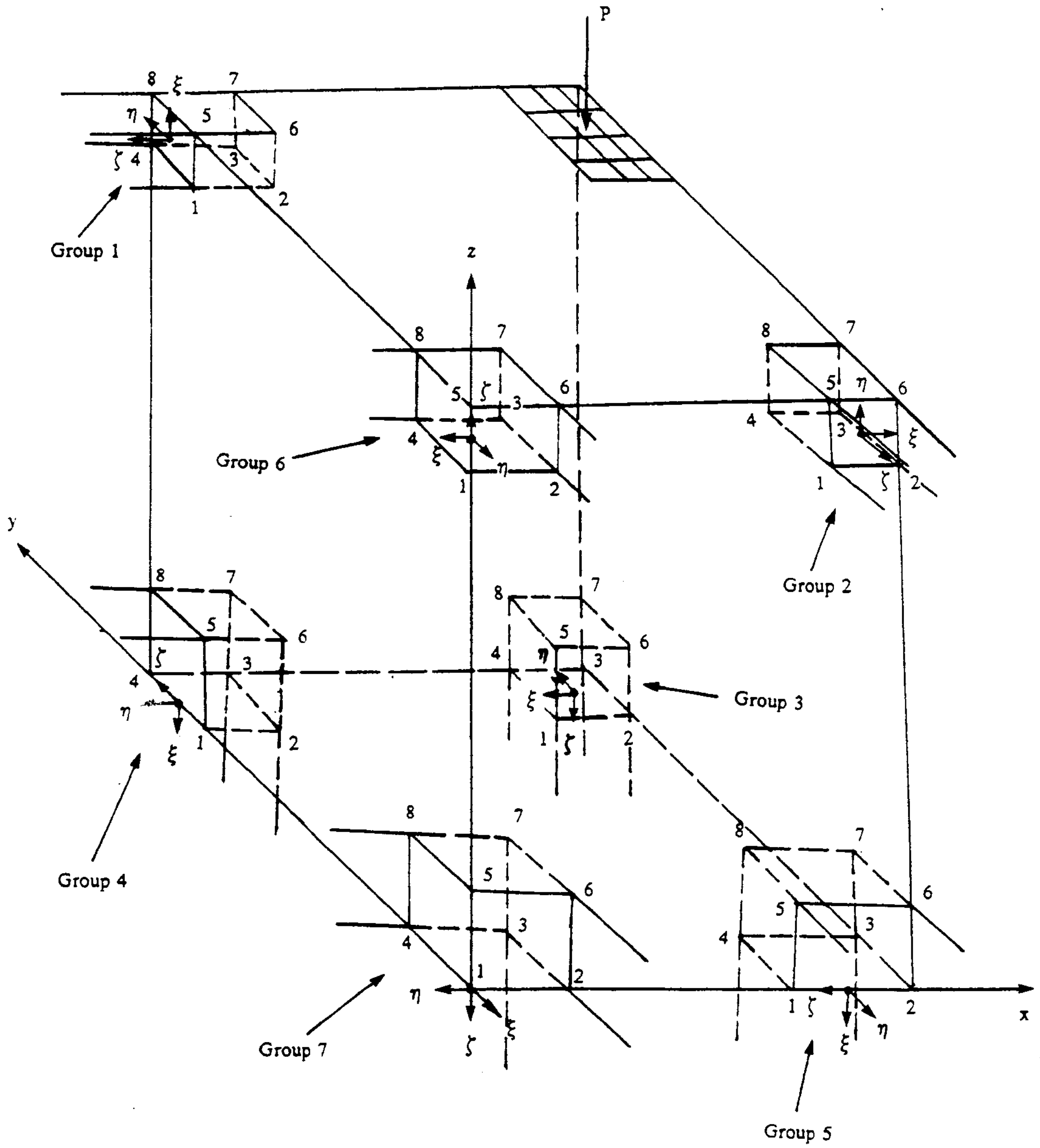

Figure 3.3. Infinite element boundaries model.

boundaries x = 0.0 , y = 0.0 and z = 0.0 are considered as infinite boundaries instead of the viscous boundaries. The infinite elements are categorized into 7 groups as shown in Figure 3.3. Groups 1, 2 and 3 are singly infinite elements. Groups 4, 5 and 6 are doubly infinite elements. Group 7 is a triply infinite element. The relationships between nodes of each group and nodes of infinite elements shown in Figures C.2-C.4 is listed in Table 3.1.

Considering the infinite element boundaries instead of the viscous boundaries, the subroutines "EMJAC1", "SFUNSQ1" and "BMAT1" in MNROAD-93 are used instead of the subroutines "EMJAC", "SFUNSQ" and "BMAT" in the program MNROAD, respectively. The subroutines "DAMPER", which calculates the damping force, and "DELMAS", which calculates

Table 3.1. The corresponding node relationships.

Nodes of group 1	1	2	3	4	5	6	7	8
Nodes of element in Figure C.2	5	1	4	8	6	2	3	7
Nodes of group 2	1	2	3	4	5	6	7	8
Nodes of element in Figure C.2	5	6	2	1	8	7	3	4
Nodes of group 3	1	2	3	4	5	6	7	8
Nodes of element in Figure C.2	6	5	8	7	2	1	4	3
Nodes of group 4	1	2	3	4	5	6	7	8
Nodes of element in Figure C.3	3	2	6	7	4	1	5	8
Nodes of group 5	1	2	3	4	5	6	7	8
Nodes of element in Figure C.3	7	3	2	6	8	4	1	5
Nodes of group 6	1	2	3	4	5	6	7	8
Nodes of element in Figure C.3	3	4	1	2	7	8	5	6
Nodes of group 7	1	2	3	4	5	6	7	8
Nodes of element in Figure C.4	7	6	5	8	3	2	1	4

the additional mass due to lag of velocity, are changed, because the damping force and the additional mass due to lag of velocity do not need to be calculated for the infinite boundaries.

PROGRAM MNSLAB DESCRIPTION

Introduction

The complete finite element model MNSLAB consists of two submodels: one is "Concrete Slabs Connected by Dowel Bars Model", which is called MNSLAB-1, another one is "Dowel Bar and Slab Interaction Analysis Model", which is called MNSLAB-2. The program MNSLAB-1 is capable of solving a two-dimensional, linear elastic and dynamic problems. Only one layer (slab) can be modelled. The subbase and subgrade are considered as a Winkler foundation by the composite modulus of subgrade reaction, k. The program MNSLAB-2 is a three-dimensional, linear elastic and static model. The objective of this model is to find out the relative deformations between dowel bars and concrete slabs.

Usually, we first use the program MNSLAB-2 to find out the relative deformations between dowel bars and concrete slabs, then put this relative deformations into the program MNSLAB-1 to analyze the pavement responses. The program MNSLAB-2 can be compiled, linked and executed in the DOS system (personal computer) and the program MNSLAB-1 can be compiled, linked and executed in the SUN systems (workstation) or the CRAY systems (supercomputer).

Model Configurations

The finite element mesh configurations of MNSLAB-1 and MNSLAB-2 are shown in Figure 4.10 and Figure 3.4, respectively. Mesh configuration and element selection must be accomplished carefully with a knowledge of finite element analysis concepts to ensure accurate analysis. Some generally accepted rules of thumb for mesh configuration include:

1. The aspect ratio (length to width) of elements located near applied loads or critical output nodes should not exceed 2:1.
2. Element dimensions in the vicinity of applied loads should be about 0.6 to 0.8 times the local slab thickness.
3. Most accurate results are obtained when applied loads cover entire elements. Acceptable results may be obtained with as little as 50% coverage of a single element.

Program MNSLAB-1 Structure

The source code of the program MNSLAB-1 is about 1720 lines in Fortran 77. The structure of the program MNSLAB-1 illustrated in Figure 3.5 is very similar to the structure of the program MNROAD-93. There is no need to calculate the viscous forces and the additional mass matrix in the program MNSLAB-1. The steps involved in the displacement method of finite element analysis are as follows:

1. Mesh generation----The slab is divided into 9-node quadrilateral elements (Figure D.2). This is accomplished through the mesh generation program, which generates the nodal coordinates, element connectivity matrices, external force vectors and the boundary condition matrices.

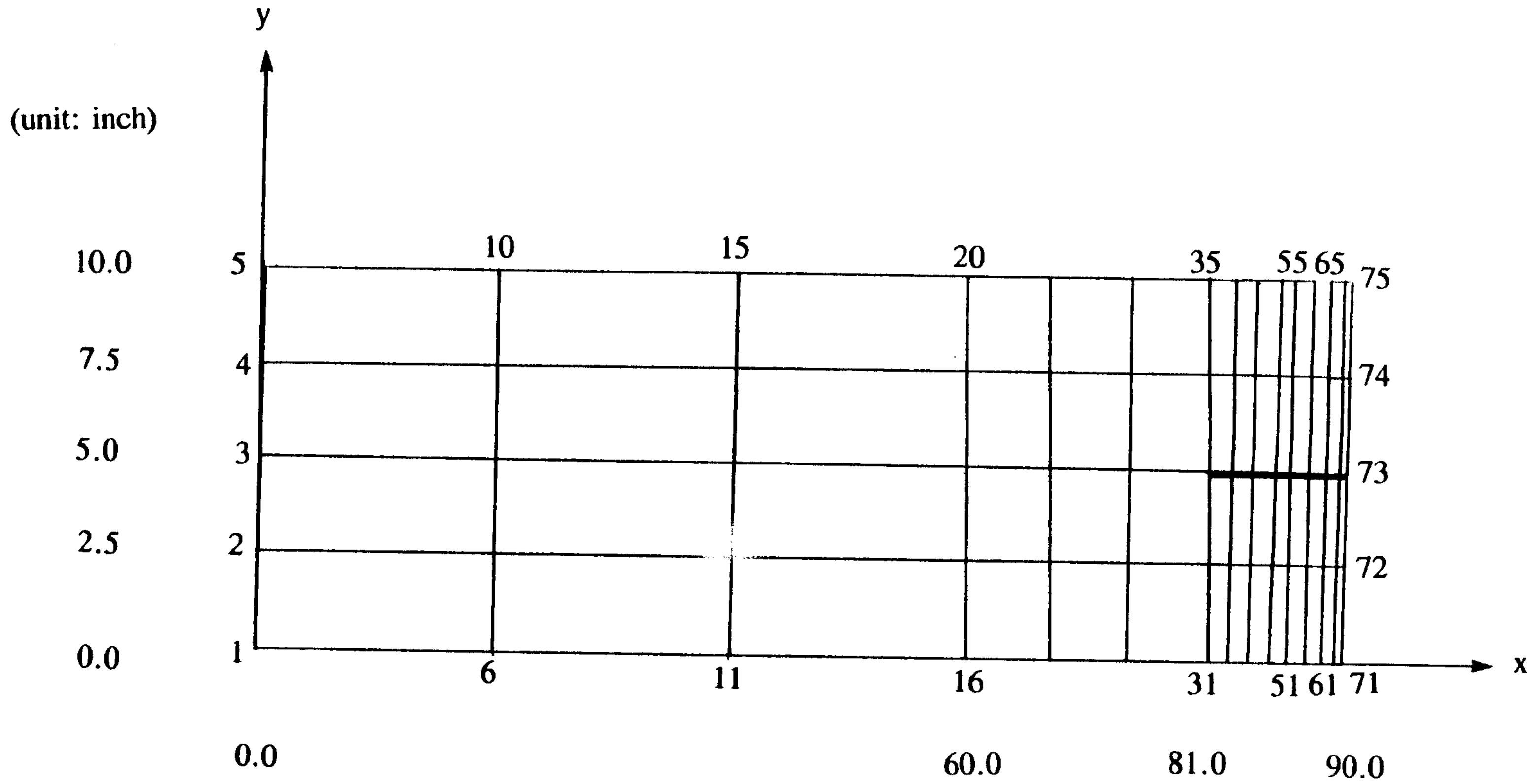

Figure 3.4. MNSLAB-2 model mesh configuration.

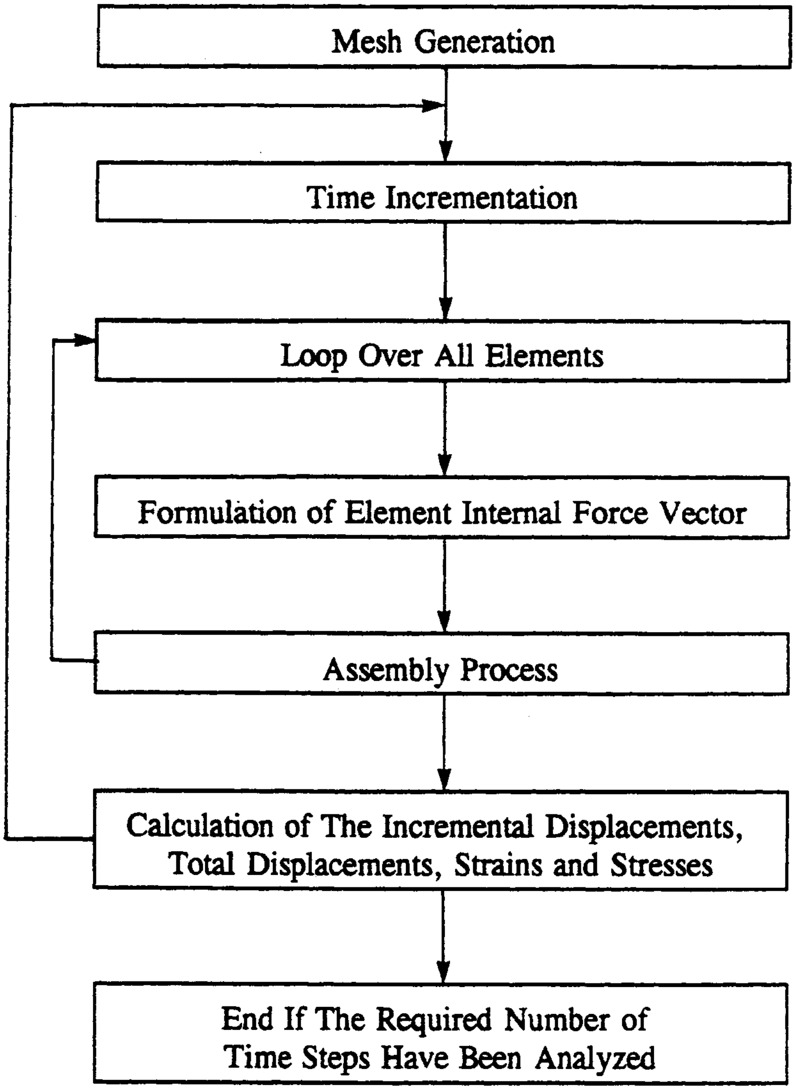

Figure 3.5. Flow chart for the program MNSLAB-1.

2. Element analysis----The internal force vectors for the elements are evaluated using the principle of virtual work. This includes the formulation of a constitutive matrix for each material and the evaluation of the standard B matrix at each Gauss point.
3. Displacement vector----This is calculated through the central difference method.
4. Formation of mass matrix----The lumped mass procedure is used which makes the mass matrix diagonal (Cook et al., 1989).
5. The element internal force vectors and mass matrices are assembled by special purpose subroutines.
6. The time dependent external load is arbitrary and described in a piece-wise linear manner.
7. Stress and strain analysis----The displacements evaluated in the above step 3 are now substituted into appropriate matrices and the resulting stresses and strains at the integration points/nodes are determined (by Eqs.(D.6), (D.7) and (D.22) in Appendix D).

Mesh Generation Program

The mesh is generated using the coordinates of the 9 nodes of the domain being descretized, which is an input to the program. The generation is accomplished by applying the principle of isoparametric mapping. For example, the x-coordinates of the nodes inside the domain bounded by the given 9 nodes are generated using the relation:

$$x = \sum x_I N_I \tag{3.5}$$

where

x = the x-coordinate of the node being generated.

x_I = the x-coordinate of the given 9 nodes.

N_I = The value of the shape functions evaluated at the point under consideration.

Similarly, the y-coordinate can be calculated.

To generate nodes within a subdomain where different spacing is to be introduced, another set of coordinates for the 9 nodes are to be input, i.e., the coordinates of the 9 nodes are to be input once for each change in spacing of nodes in any direction. The spacing and number of nodes in each direction can be varied at will. The nodal coordinates are stored in the coordinate matrix.

Once the nodes are generated, the elements are formed using the connectivity data. Then the elements are generated automatically in two directions by using the increment data. The nodes forming the elements are stored in the connectivity matrix. Simultaneously, material numbers are assigned to the elements, and this completes the geometric description of the problem. Boundary conditions and equation numbers are also generated and stored in the matrix, named ID. External force information is stored as a vector in f^{ext}. The material properties are read from the input file and a constitutive matrix is calculated for each material.

Program MNSLAB-2 Structure

The source code of the program MNSLAB-2 is about 1250 lines in Fortran 77. The structure of the program MNSLAB-2 is illustrated in Figure 3.6. This is a general structure for finite element analysis of the linear elastic systems. The mesh generation process is similar to the above "Mesh Generation Program".

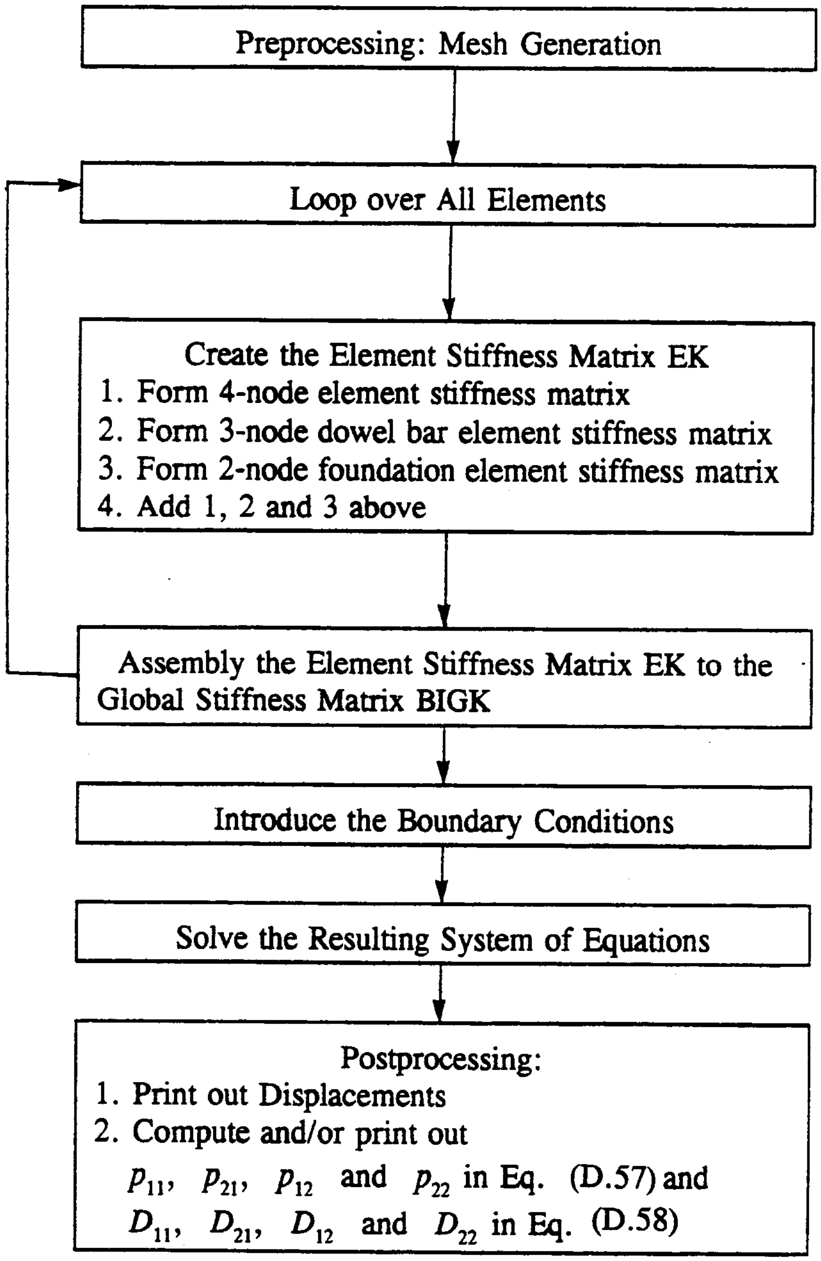

Figure 3.6. Flow chart for the program MNSLAB-2.

CHAPTER 4

RESULTS AND DISCUSSION

MNROAD-93

Introduction

Two problems were selected to evaluate the performance of MNROAD-93 in which the material can be simulated to be either elastic or elasto-plastic, and the boundary can be modelled as either a viscous boundary or an infinite boundary.

The first problem (case A) is the same as the one solved previously using elastic material model and viscous boundary (program MNROAD) [Prakasha, 1990]. Selection of this particular problem enables one to validate the present model by direct comparison with the available FWD (Falling-Weight Deflectometer) experimental results. Pavement materials in this problem can also be assumed elasto-plastic, which may actually be closer to the model materials, such as soils. Therefore the numerical simulation results for the elasto-plastic analysis are obtained here and compared with the results from elastic analysis. The comparison of the results for elastic analysis using viscous boundaries and infinite elements is also presented.

The Minnesota Department of Transportation (Mn/DOT) provided another set of FWD experimental data including loads and displacements. These field testing data were collected on April 2,1993 at station 1107.60 of the Mn/ROAD project test road. Therefore the simulations under the experimental loading condition were performed. The simulated displacements were compared with the FWD results. This is the second problem (case B) discussed in this study. The simulation results for this problem were obtained under the four different combinations of the material characteristics and boundary conditions, i.e., elasto-plastic materials with infinite element boundaries.

Any discrepancies between the model simulations and measurements may lead to conclusions revealing sources of the disagreements and ways of further improving of the models.

Descriptions of Case A

For case A, the pavement consists of four layers from top to bottom: a 6 inch asphalt concrete surface course, a 6 inch granular base course, a 12 inch granular subbase course and a 200 inch clayey subgrade as illustrated in Figure 4.1.

The characteristics of the materials used in model simulation are specified in Table 4.1. Part A of Table 4.1 includes Young'modulus, E, Poisson's ratio, ν, mass density, ρ, internal friction, ϕ, and cohesion, C. The model simulation for elastic analysis uses the first three parameters only, the perfectly plastic analysis requires all five parameters. The values of these material properties were obtained from experiments conducted by Mn/DOT. Part B and Part C of Table 4.1 provides some additional material properties required for work-hardening or work-softening analysis. The values of the material properties in Part B and Part C of Table 4.1 were estimated by model calibration which will be discussed later.

The loading plate used in FWD measurement is a circular plate with a 6 inch radius. However the load is modelled to be uniformly distributed over an equivalent square area to suit the model geometry. Due to the symmetric load distribution on the circular plate, a quarter of loading area is therefore used for the model simulation as shown in Figure 4.2. Case A was solved under the dynamic load whose time variation was taken from the FWD test, and is shown

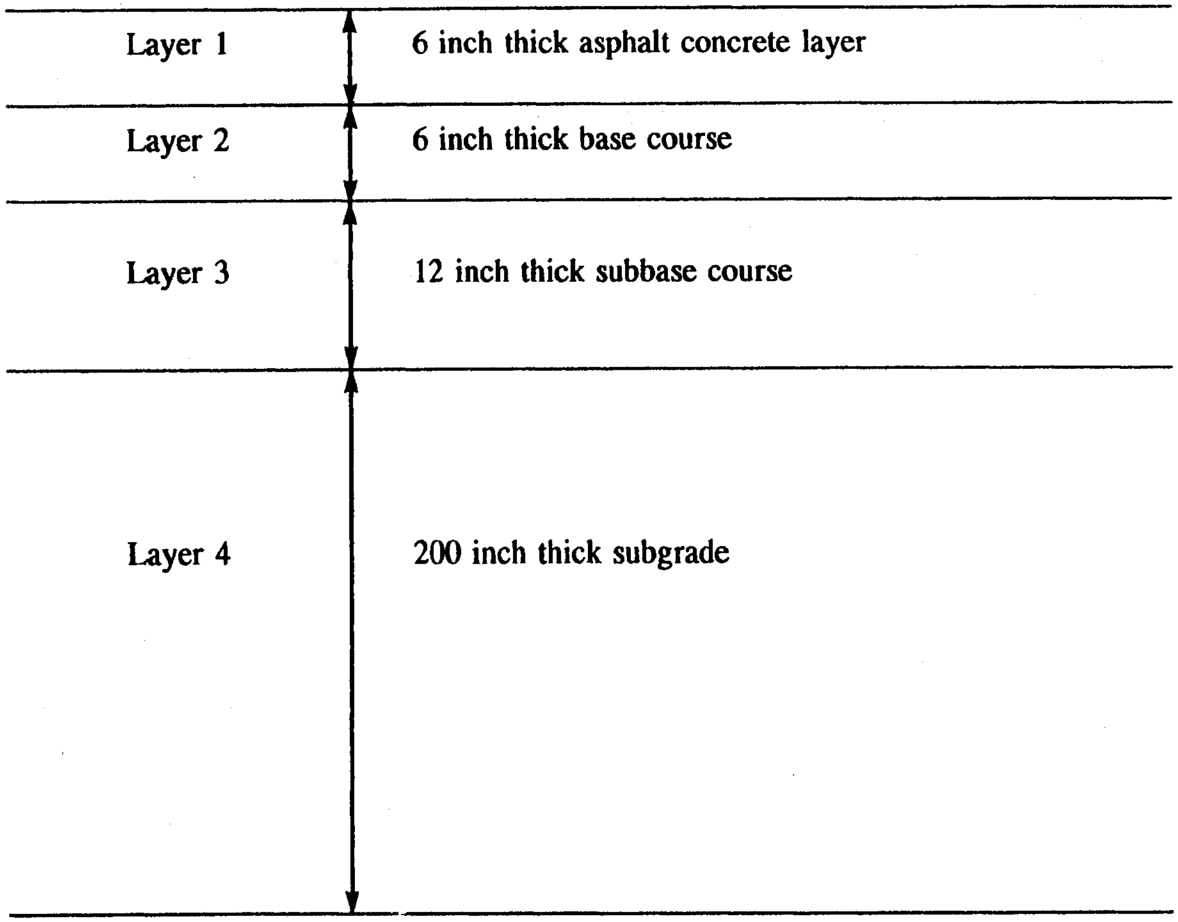

Figure 4.1. The pavement structure for case A.

Table 4.1. Material properties for case A.

PART A:

layer	Young's Modulus E (psi)	Poisson's Ratio ν	Mass Density ρ (lbf.s^2/in^4)	Internal Friction ϕ (°)	Cohesion C (psi)
1	2.7E5	0.35	19E-5	------	------
2	3.0E4	0.40	17E-5	45	0
3	2.0E4	0.40	15E-5	40	0
4	2.0E4	0.45	13E-5	15	2

PART B:

Hardening	layer 2		layer 3		Layer 4	
Segment	Plastic Modulus H (psi)	Effective Plastic Strain e^p	Plastic Modulus H (psi)	Effective Plastic Strain e^p	Plastic Modulus H (psi)	Effective Plastic Strain e^p
1	3000.0	1.0E-4	2000.0	1.0E-5	2000.0	1.0E-5
2	2000.0	5.0E-4	1400.0	5.0E-5	1400.0	5.0E-5
3	1000.0	1.0E-3	700.0	1.0E-4	700.0	1.0E-4
4	0.0	1.0	0.0	1.0	0.0	1.0

PART C:

Softening	layer 2		layer 3		Layer 4	
Segment	Plastic Modulus H (psi)	Effective Plastic Strain e^p	Plastic Modulus H (psi)	Effective Plastic Strain e^p	Plastic Modulus H (psi)	Effective Plastic Strain e^p
1	3000.0	1.0E-4	2000.0	1.0E-5	2000.0	1.0E-5
2	1000.0	5.0E-4	700.0	5.0E-5	700.0	5.0E-5
3	-1000.0	1.0E-3	-700.0	1.0E-4	-700.0	1.0E-4
4	0.0	1.0	0.0	1.0	0.0	1.0

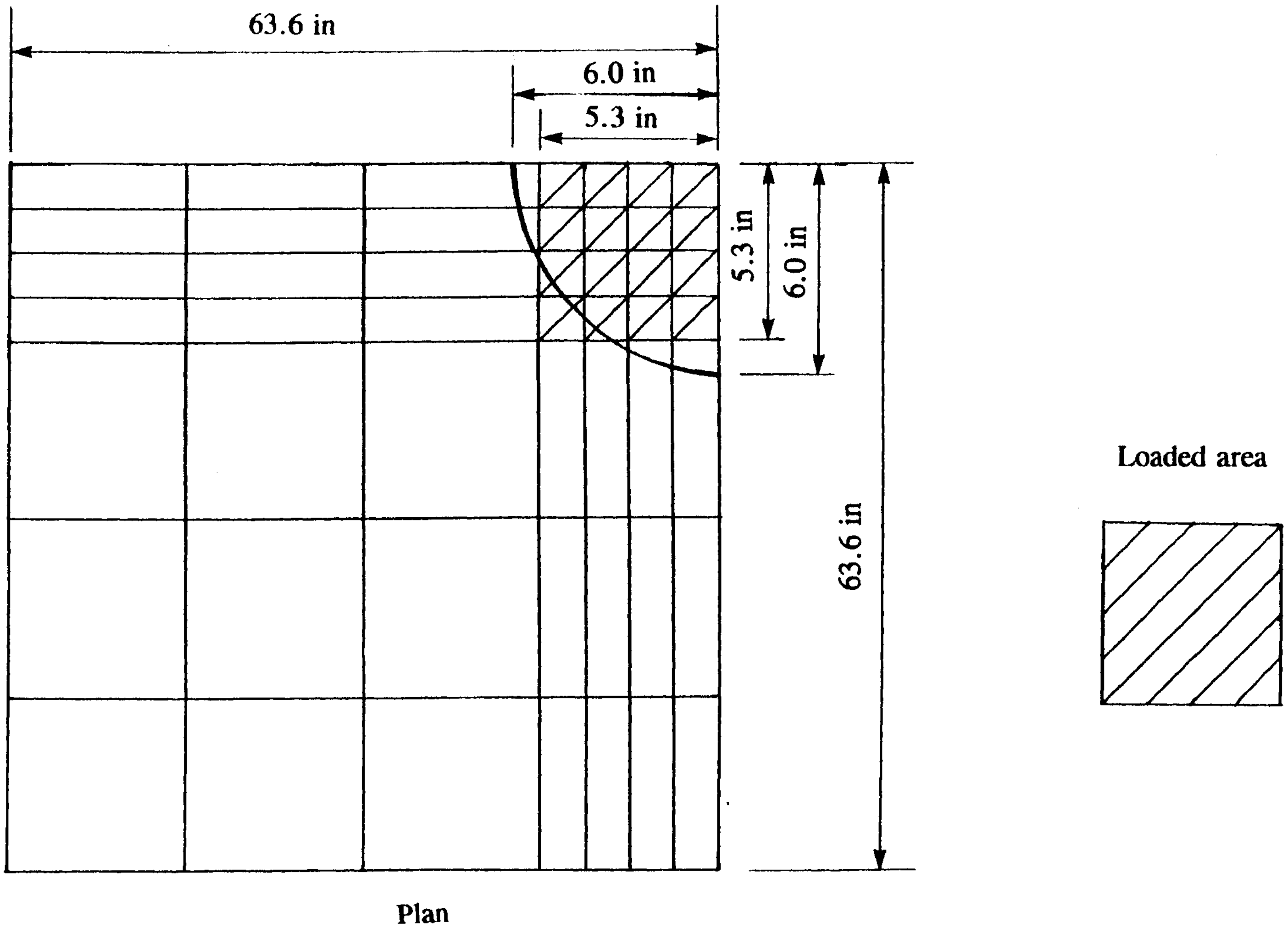

Figure 4.2. The equivalent square loading area used in model study.

in Figure 4.3. In the first 0.0012 seconds the load increased from 0 to 16,000 lbs (maximum loading value), and then decreased to 0 lbs when time is 0.028 seconds. The sampling rate used in FWD experiment is 0.0002 seconds, however the time step used in model simulation is usually on the order of 0.000001 seconds. Therefore in the model simulation the time variation of dynamic loads consists of piece-wise linear approximation of the experimental curve, the time interval used in this approximation is 0.001 seconds.

Results and Comparisons for Case A

One of the main aspects of the study for MNROAD (elastic model) was to investigate various viscous boundaries conditions which eliminate the spurious reflections. The numerical simulated results of displacements are quite strongly dependent on the boundary conditions used and, in particular, on the values of the parameters a and b defining the viscosity of the boundary [Prakasha, 1990, section 3.3.5.1]. The optimal selection of parameters a and b as described by White et al. [1977], produces satisfactory results relative to the FWD experimental results. Therefore this optimal result for the elastic model analysis using MNROAD will be compared with the results for the elasto-plastic model analysis and infinite element boundary model analysis using MNROAD-93.

In case A, the pavement materials are now assumed to be elasto-plastic materials except the asphalt concrete layer which is still elastic. These materials can be simulated by a perfectly plastic model and linear isotropic work-hardening model as described in Appendix B. The plastic modulus *H* as defined in Eq.(B.28) ($\kappa = \kappa_0 + H\,e^p$) is equal 0.0 in perfectly plastic model and has a constant value in linear work-hardening model. In these two models, the plastic

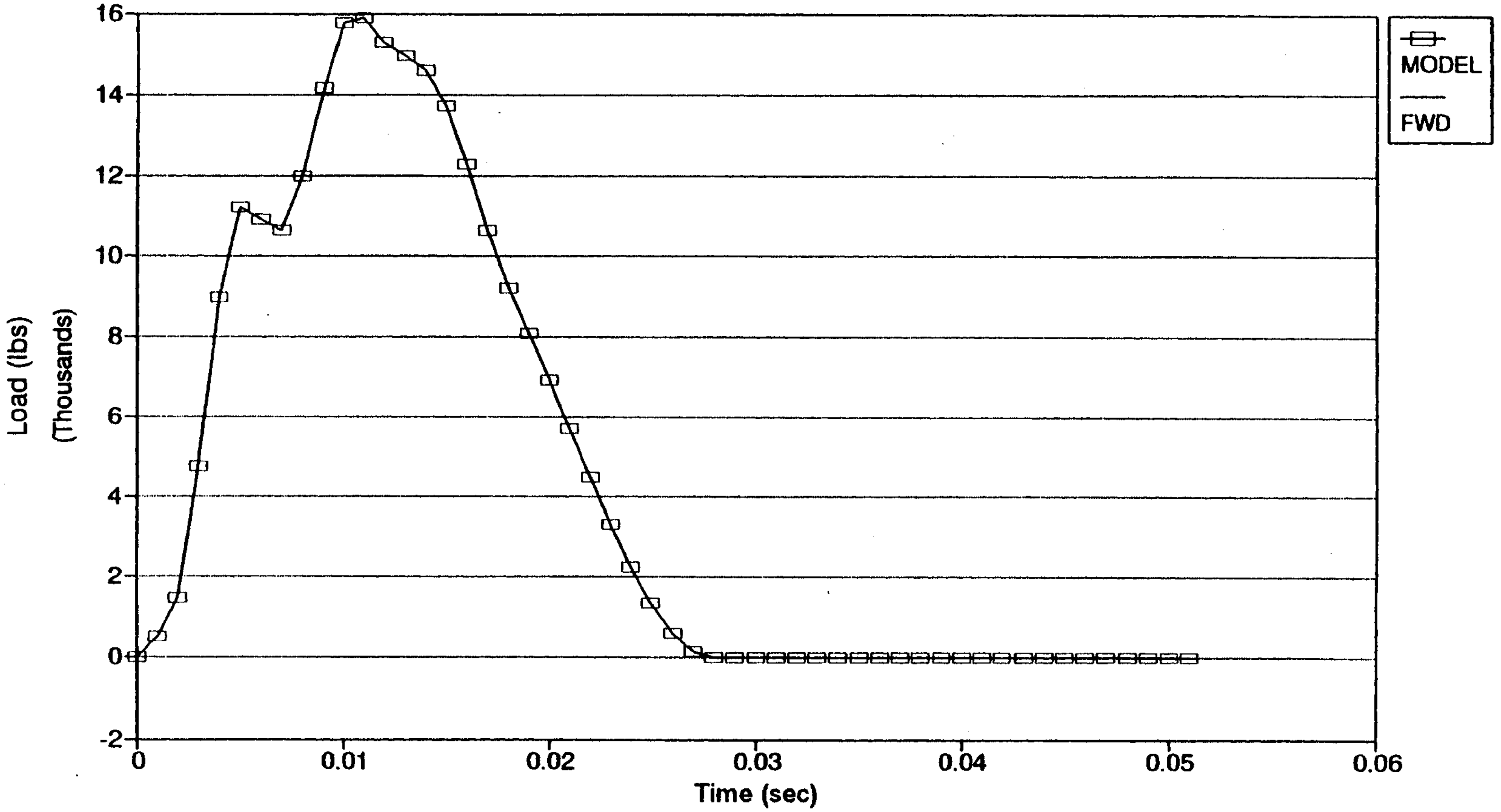

Figure 4.3. The relationship between load and time for case A.

modulus H is independent of the effective plastic strain e^p as schematically described in Figure 4.4. Another two plastic models: n segments isotropic work-hardening model and n segments isotropic work-softening model are also shown in Figure 4.4. In case A, 4 segments were used, the values corresponding to H_1, e_1^p, H_2, e_2^p, H_3, e_3^p, H_4 and e_4^p for layer 2, layer 3 and layer 4 are listed in parts B and C of Table 4.1. The value of plastic modulus H used in the first segment of n segment models may be used for linear isotropic work-hardening model.

The simulated displacement history at the center of the load using MNROAD-93 (elasto-plastic model) is presented in Figure 4.5 as well as the simulated displacement of elastic model and FWD experimental results. The displacement from the FWD experiment reaches the maximum value 0.0255 inches when the time is 0.014 seconds (the maximum load occurs at t=0.012 seconds from Figure 4.3), and then decreases to 0.0000 inches when the time is 0.031 seconds, after that the displacement slightly increases to 0.0020 inches and then almost keeps this level. The simulated displacement using elastic model reaches the maximum value 0.0252 inches, which is just a little smaller than the FWD result, when the time is 0.016 seconds which is later than the FWD result. Then the simulated displacement using elastic model decreases, but does not decrease to 0.0000 inch (this probably caused by an impractical boundary), just remains at about 0.0030 inches level, which is higher than the FWD result. The simulated displacements using the above four plastic models follow a very similar trend. At the beginning (time t<0.005 seconds), the simulated displacements using the plastic models are exactly same as the simulated displacements using the elastic model (materials do not reach the plastic range), but both are slightly smaller than the FWD results. For the perfectly plastic model, 4 segments

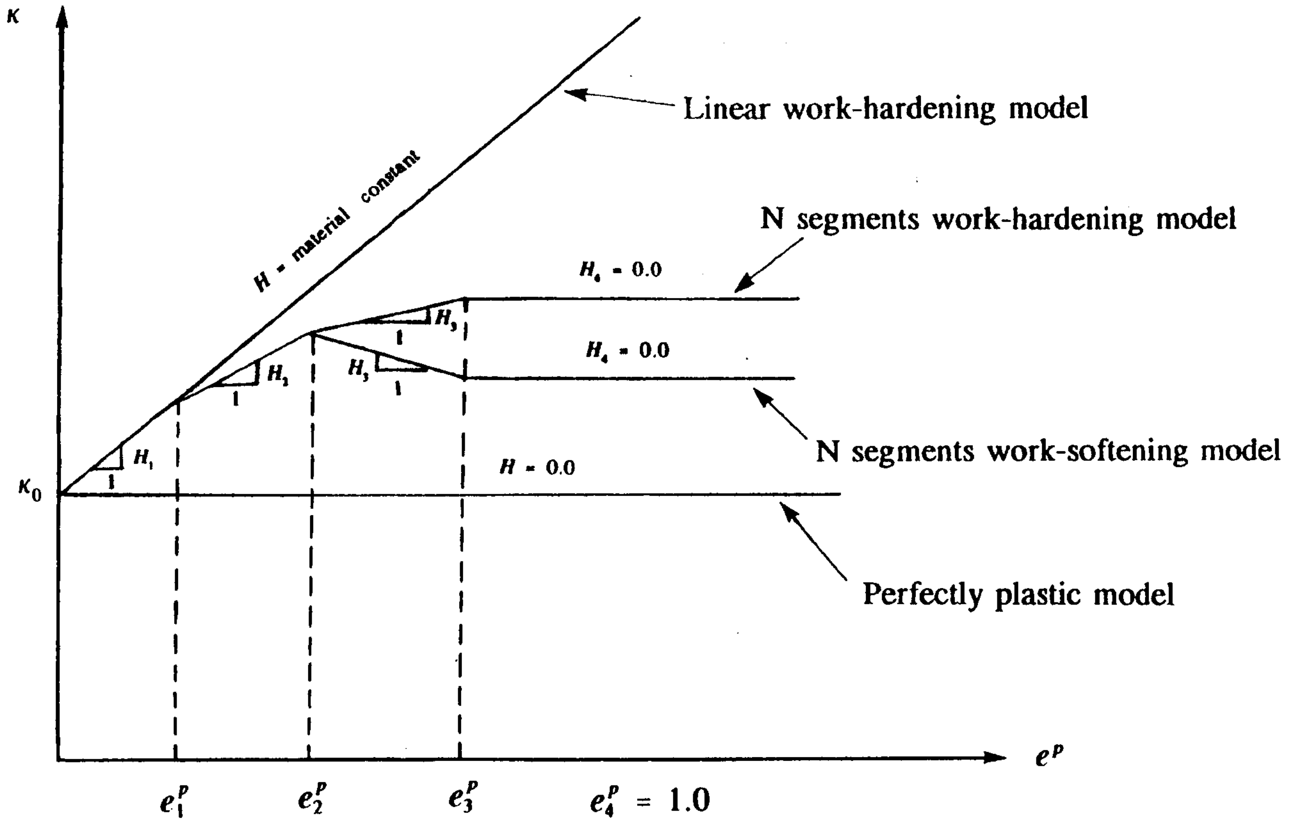

Figure 4.4. Illustration of the relationship $\kappa = \kappa_0 + H\, e^p$ for four plastic models used in case A.

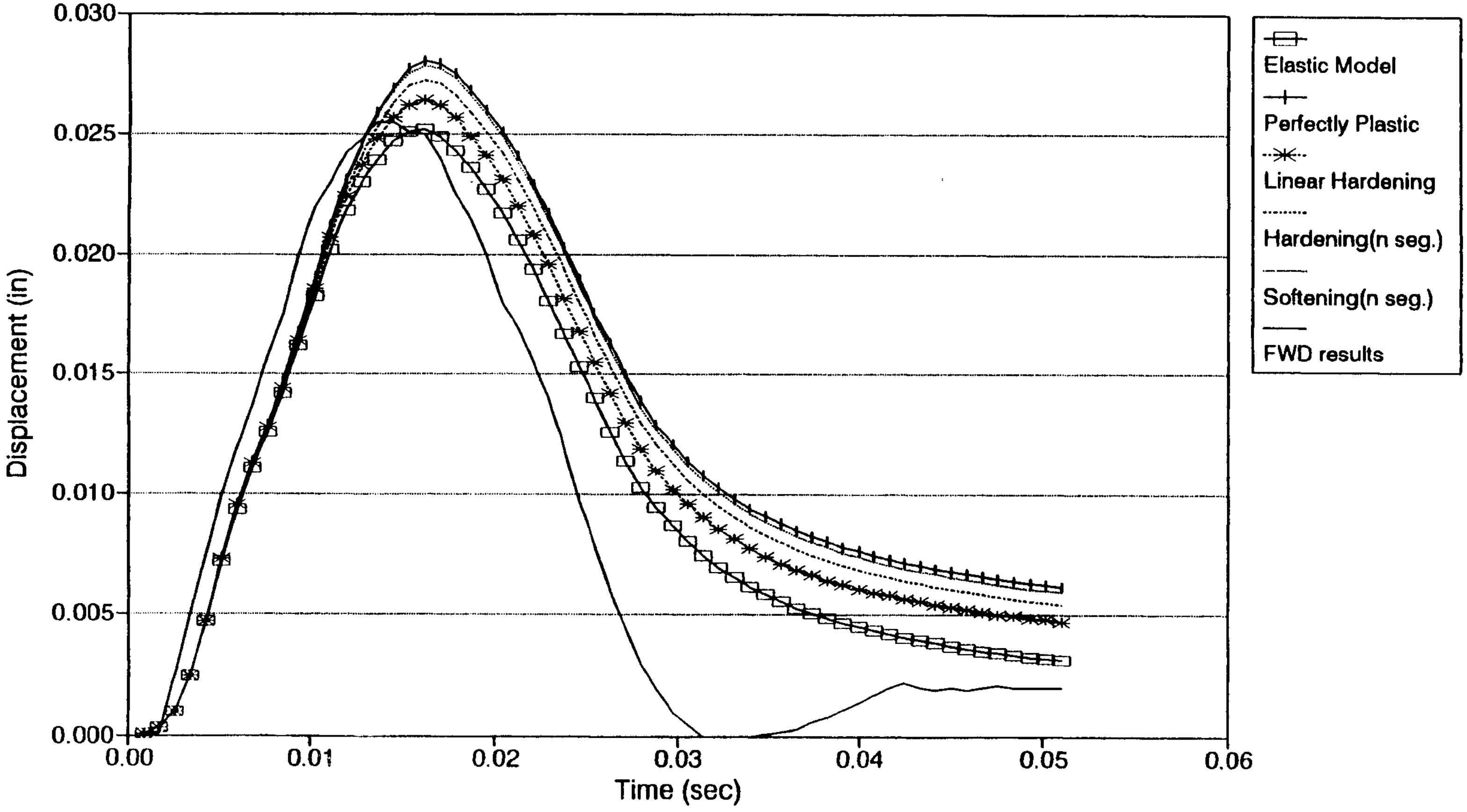

Figure 4.5. Comparisons between the simulated displacements with viscous boundaries and the FWD results.

softening model, 4 segments hardening model and linear hardening model, the displacements arrive the maximum values 0.0280, 0.0278, 0.0272 and 0.0264 inches respectively at the same time t=0.016 seconds, which is the same time as for the elastic model. Then the displacements decrease to 0.0061, 0.0059, 0.0054 and 0.0047 inches respectively and almost maintain these levels afterwards. As can be seen in Figure 4.5, the maximum simulated displacements occur 0.002 seconds later than the FWD experimental value (this may have to do with the initial conditions). In addition the final displacements (permanent displacements) obtained from the simulated models are larger than those from the FWD experiment (0.0020 inches). Overall, the displacements using the elastic model produce a better fit to the FWD results than the displacements using the plastic models from Figure 4.5.

The simulated stresses of the base layer (at middle point) under the load by using elasto-plastic models as well as the elastic model are shown in Figure 4.6. For the elastic model, the stress finally recovers to zero, but for the elasto-plastic models, a value of the tensile residual stresses remain, which are unrealistic.

Case A was also solved by using the elastic model with two different boundary conditions: viscous boundary and infinite element boundary. The simulated displacement history at the center of the load as well as the FWD results are presented in Figure 4.7. The results obtained with the infinite element boundary are slightly closer to the FWD results than those resulting from viscous boundary approximation. The maximum displacement value of the infinite element boundary case is larger than the viscous boundary case and the final displacement (permanent displacement) value of the infinite element boundary case is smaller than the viscous boundary case.

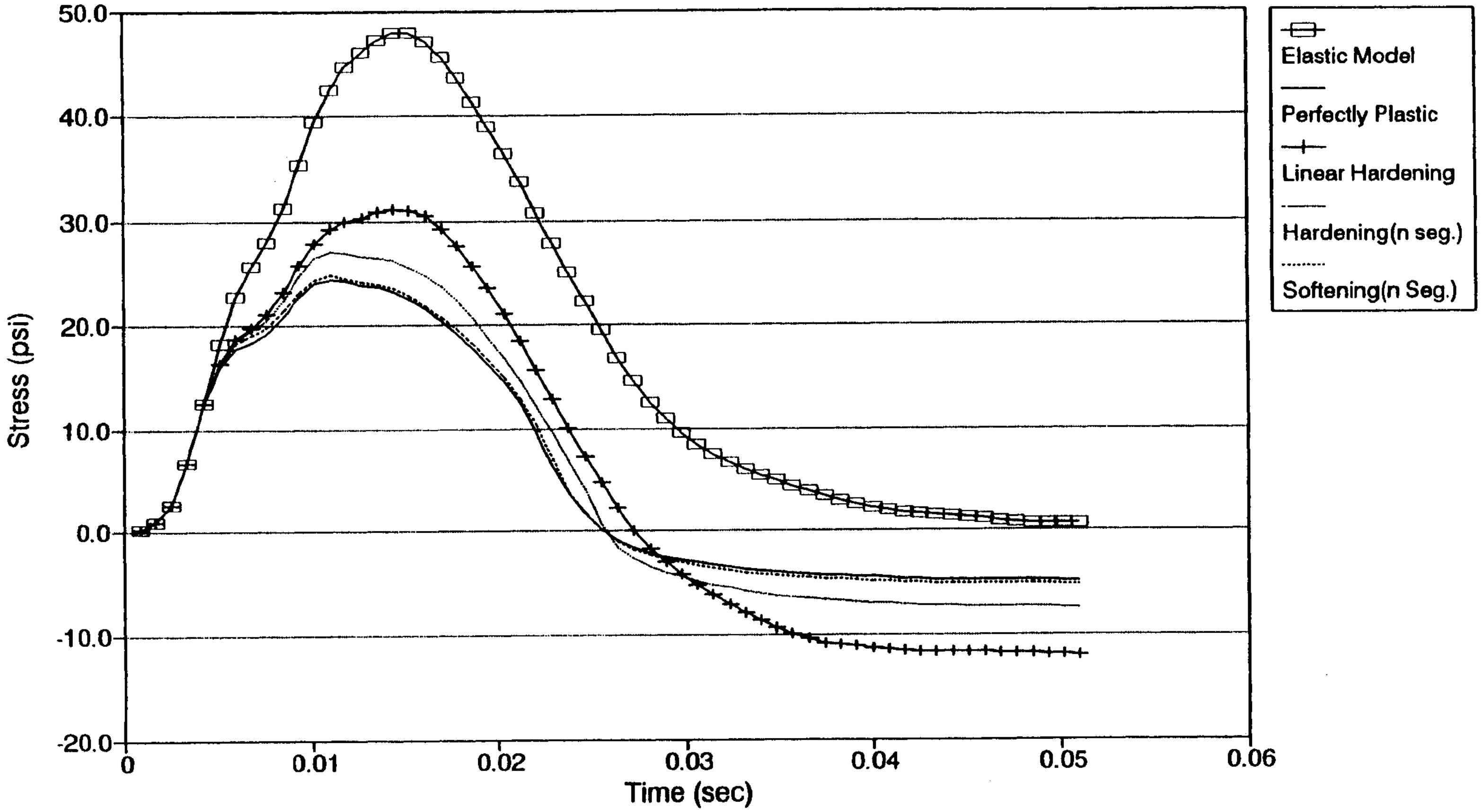

Figure 4.6. Comparisons of stresses by using the elasto-plastic models and the elastic model, both with viscous boundaries.

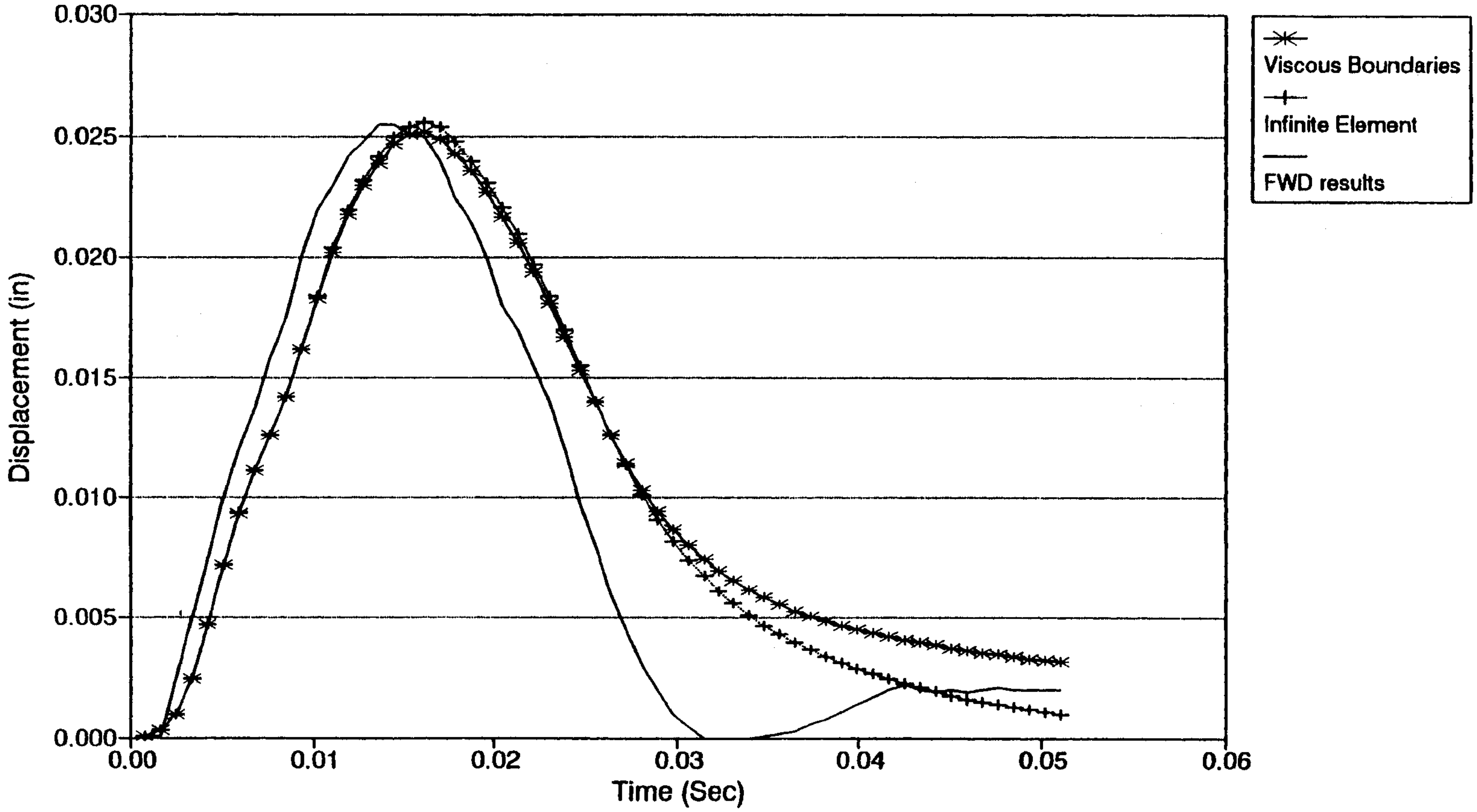

Figure 4.7. Comparison between the simulated displacements using elastic model with two boundary conditions and the FWD results.

Descriptions of Case B

Case B is similar to case A. The pavement consists of three layers: a 6 inch asphalt concrete surface course, a 36 inch granular base course and a 200 inch (used in model) silty-clay subgrade. This is Mn/ROAD section 01. The material properties are listed in Table 4.2. The FWD test data for case B was obtained from the Minnesota Department of Transportation. The dynamic load time variation was taken from the experiment is shown in Figure 4.8. The maximum load value 15218 lbs occurred when the time was 0.012 seconds, and then the load decreased to -229 lbs at time 0.030 seconds. In the numerical model this variation consisted of piece-wise linear approximation of the experimental curve as in case A.

Table 4.2. Material properties for case B.

Materials	Young's Modulus E (psi)	Poisson's Ratio ν	Mass Density ρ (lbf.s^2/in^4)	Internal Friction ϕ (°)	Cohesion C (psi)
Asphalt Concrete	1.00E6	0.35	2.15E-4	------	------
Base	1.16E4	0.40	1.87E-4	35	0.1
Silty-clay Subgrade	2.61E4	0.45	1.78E-4	29	0.3

Results and Comparisons for Case B

The simulated displacements at the center of the load obtained from MNROAD-93 as well as the FWD results are given in Figure 4.9 . The four different combinations are: elastic model with viscous boundaries; elasto-plastic model with viscous boundaries; elastic model with

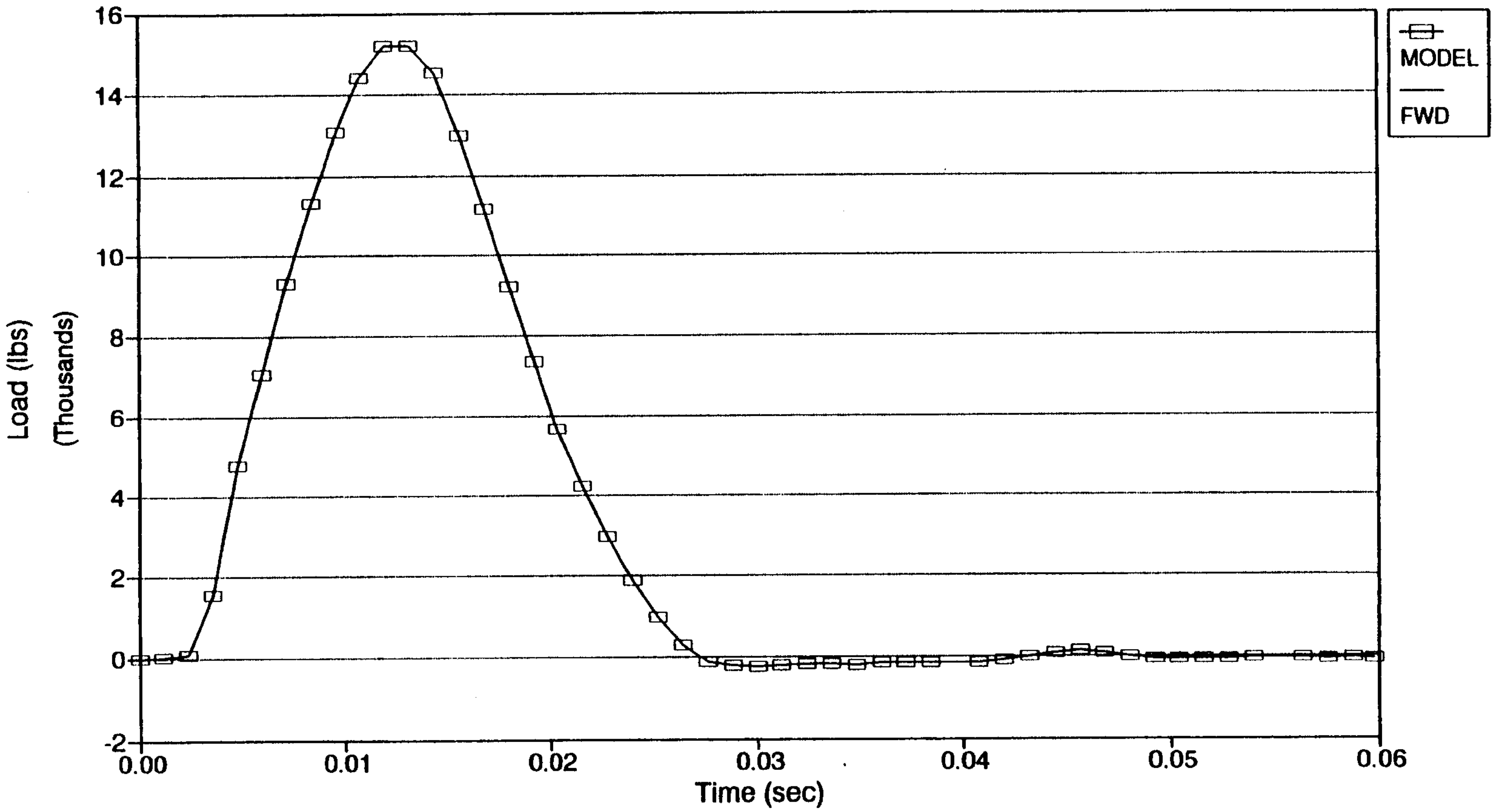

Figure 4.8. The relationship between load and time for case B.

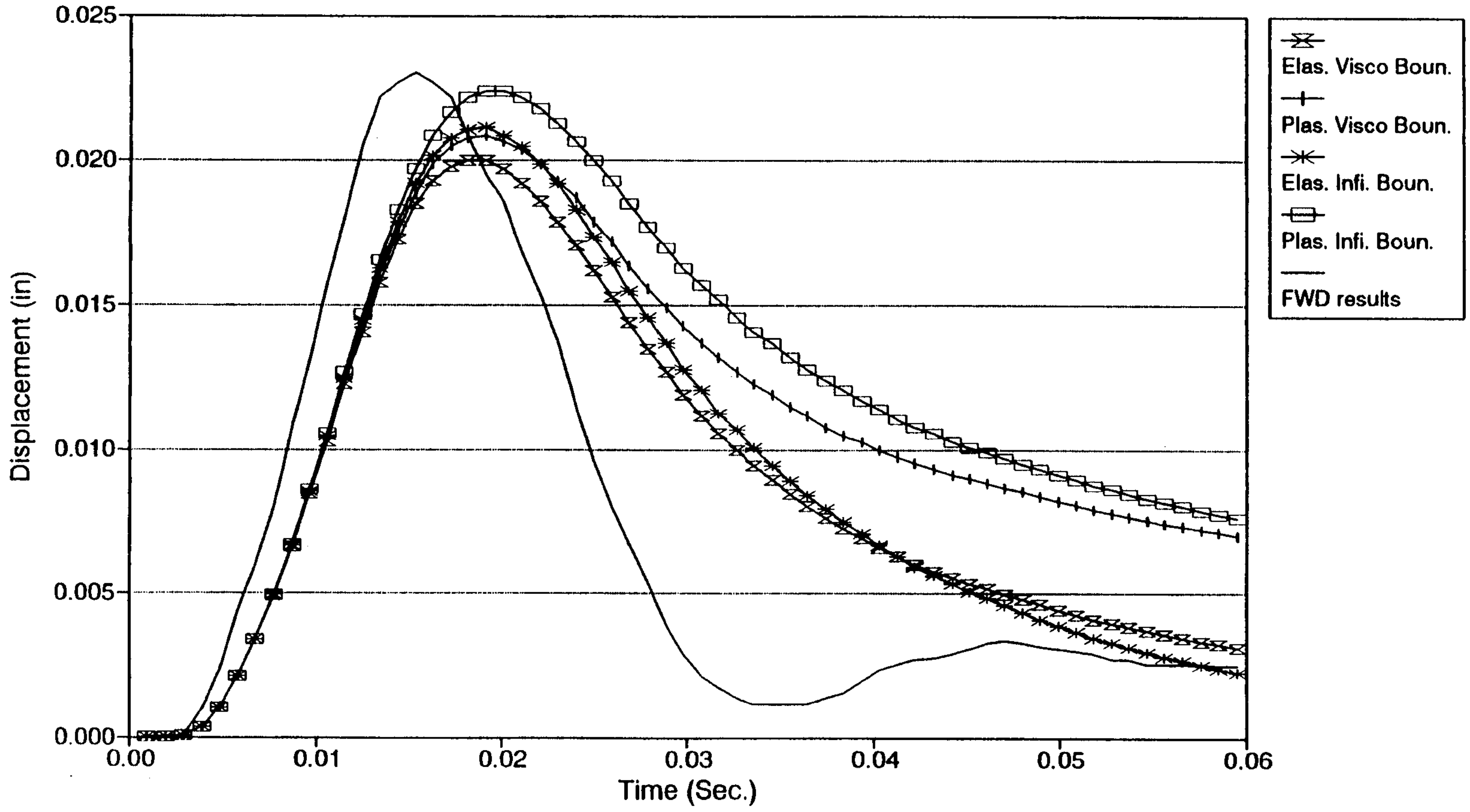

Figure 4.9. Comparison between the simulated displacements of four combinations and the FWD results.

infinite element boundaries, and elasto-plastic model with infinite element boundaries. For simplicity, in case B the perfectly plastic model was chosen as the only plastic model.

The maximum displacement simulated from the elasto-plastic model with infinite element boundaries is 0.0224 inches (t=0.020 seconds), which is much closer to the value 0.0230 inches from the FWD test (t=0.015 seconds) and is higher than those from the other three combinations. Unfortunately, this case is characterized by rather inaccurate post peak behaviors. The final displacement (permanent displacement, time t=0.0595 seconds) simulated from the elastic model with infinite boundaries was 0.0022 inches which is much closer to the value 0.0025 inches from the FWD experiment. As can be seen in Figure 4.9, each combination has regions of good and bad accuracy and it cannot be stated which combination best fits the FWD experimental results.

Discussion

For case A, the displacements (either maximum displacement or final displacement) resulting from the elastic model with viscous boundaries more closely match the results from the FWD (Figure 4.5). For case B, the maximum displacement obtained by using the elastic model with viscous boundaries is much smaller than the results from the FWD experiment, however, the maximum displacement by using the elasto-plastic model with infinite element boundaries is better to fit the result from the FWD experiment; the final permanent displacement using elastic model with infinite element boundaries is closer to the results from the FWD experiment. So, no single model yields the results matching the experimental data obtained for both case A and case B. One factor may be that the material properties do not accurately reflect the actual behavior. Another factor may be slight measurement errors in the FWD data.

There is probably a number of factors underlying the fact that the numerically simulation results do not exactly match the FWD experimental results. The sliding and separation between the asphalt concrete layer and the base course may alter the mechanical response of the structure, but this was not considered in the study. Another aspect which is probably different in the model as compared to the experiment is the distribution of the load over the area of the plate as well as the dependence of the time history of the load on the location of the load within the area underneath the plate. Note that the load was assumed uniform and the time distribution taken from Figures 4.3 and 4.8 was the same for all points of the plate. These data were obtained from the measurement of the total force variation rather than of the pressure in individual points of the plate. Finally, one should note that both the load and the model configuration were taken as square rather than as an axi-symmetric circle. All these may cause local effects which lead to discrepancies.

The results in Figures 4.7 and 4.9 indicates that somewhat the better results for the final displacements were obtained by using the infinite element boundaries than the viscous boundaries. So, choosing the boundary condition is very important too.

MNSLAB

Introduction

Load transfer is the mechanism by which stresses due to wheel loads are conveyed from one slab to the next. It is generally achieved by either aggregate interlock of the two abutting joint faces or through the use of mechanical load transfer devices, the most common of which are cylindrical steel dowel bars. One aspect of MNSLAB focuses on modeling the dowel bar load transfer mechanism, which is an important consideration in the design of jointed concrete pavements. One numerical example was chosen from Guo [1992]. This was done to compare MNSLAB results to those from Guo [1992] (static finite element model results). The displacements along the joint (both the loaded side and unloaded side) will be presented and compared. Stresses along the longitudinal edge will be presented and compared to the results from JSLAB.

Descriptions of the Numerical Example

The pavement model and finite element mesh are present in Figure 4.10. There are two whole slabs and two one-third slabs connected only by a dowel bar load transfer system (the effects of aggregate interlock are neglected). An 18,000 lb single axle load is located at the transverse joint and one tire is at the longitudinal edge as shown in Figure 4.10. The load configuration is given in Figure 4.11. The nodal force $P = p^*A_I$, where p is a uniform pressure of 100 psi, A_I is the area attributed to the node. The load time variation is shown in Figure 4.12. The boundary conditions are: the edges y = 0.0 inches and y = 144.0 inches which are considered to be free, the edges x = 0.0 inches and x = 480.0 inches which are

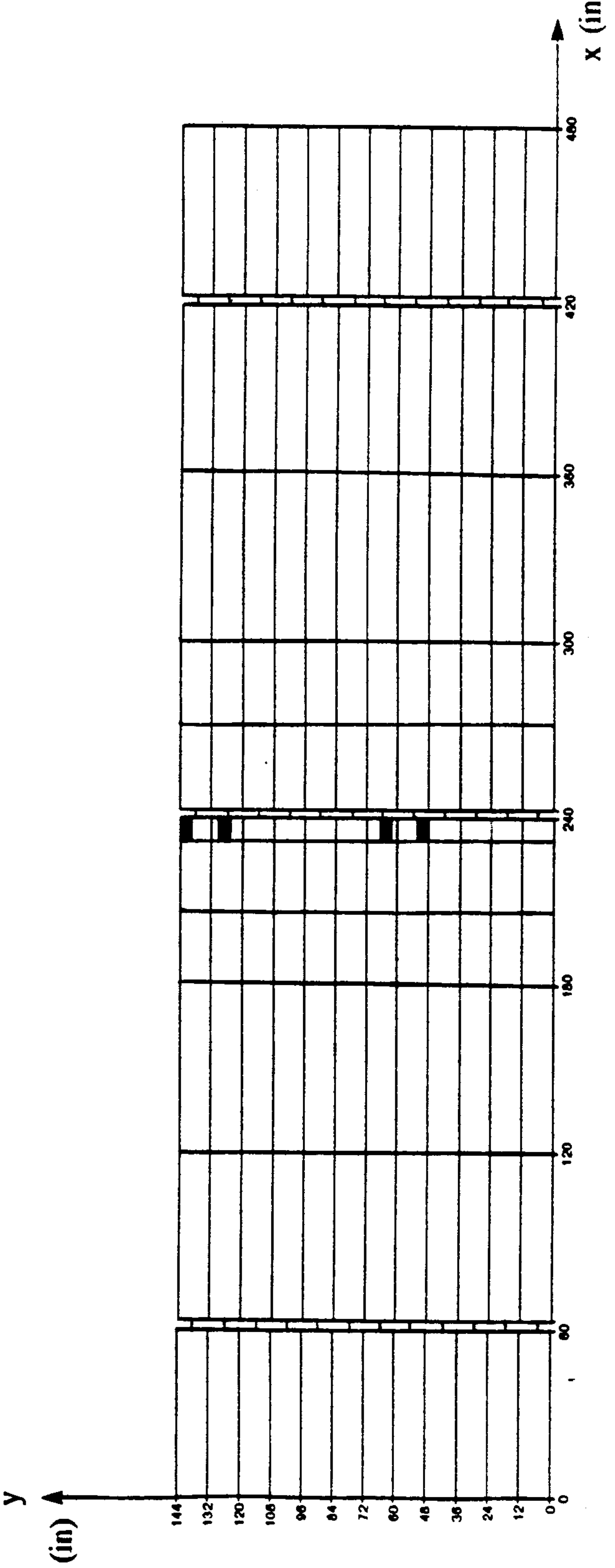

Figure 4.10. Finite element mesh and load location.

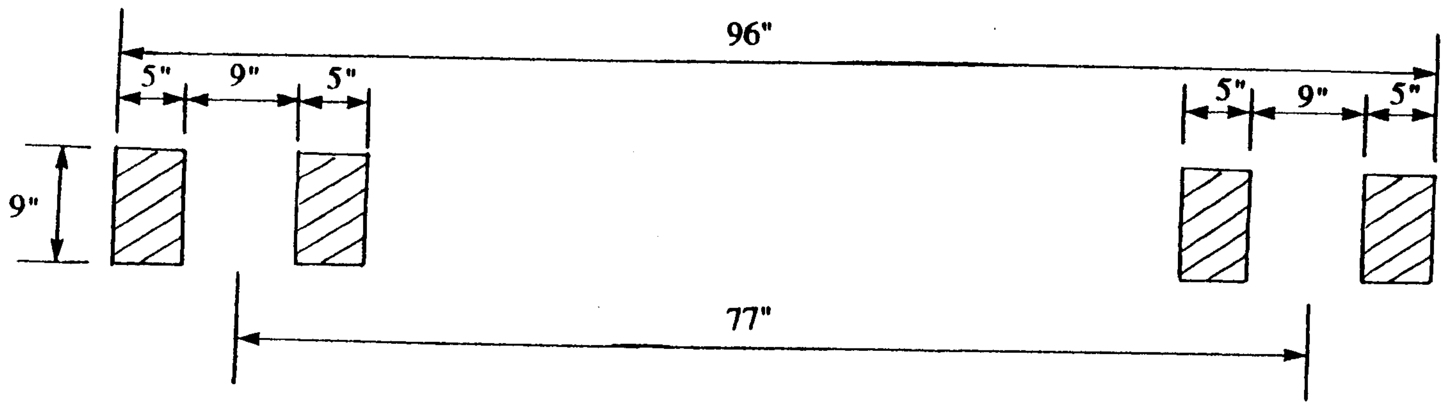

Figure 4.11. Configuration of single axle load: 18 kips, p = 100 psi.

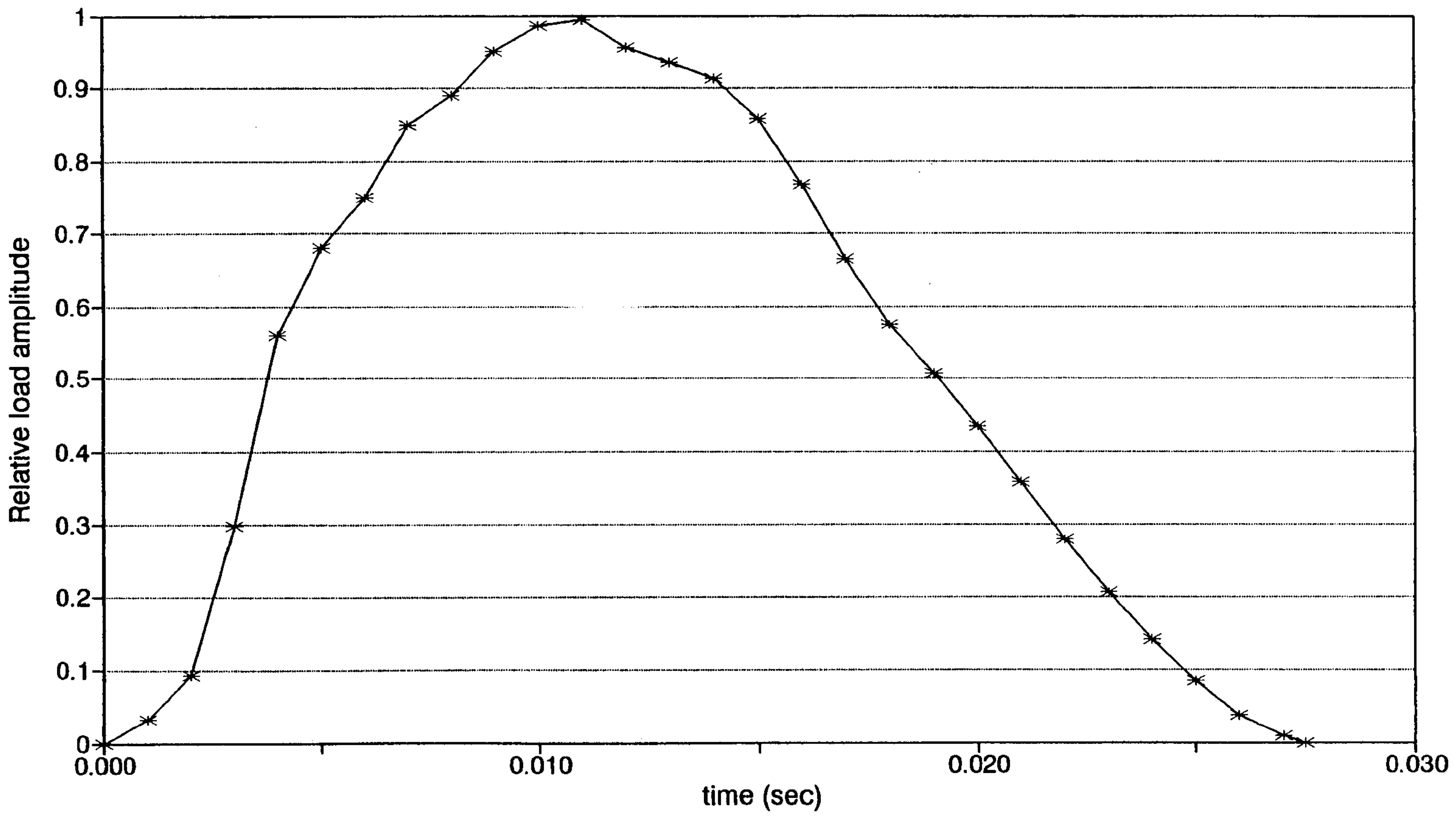

Figure 4.12. The relationship between relative load amplitude and time.

considered to be simply supported.

The major input data are listed below:

Length of each slab	180 inch
Width of slab	144 inch
Thickness of slab	10 inch
Elastic modulus of concrete	5,000,000 psi
Poisson's ratio of concrete	0.15
Subgrade reaction K-value	200 pci
Unit weight of concrete	0.09 pci
Dowel bar diameter	1.25 inch
Dowel bar spacing	12 inch
Elastic modulus of dowel bar steel	29,000,000 psi
Width of joint	0.25 inch
Poisson's ratio of steel	0.30

Results and Comparisons

Figures 4.13 and 4.14 present the displacements along the joint x =240.0 inches on the loaded side and unloaded side, respectively. The relationships between displacement and time of the points on the joint at x = 240.0 inches for both loaded side and unloaded sided are shown in Figure 4.15 and Figure 4.16. The maximum displacement of the joint at x = 240.0 inches on the loaded side is 0.03595 inches. The maximum displacement of the joint at x = 240.0 inches on the unloaded side is 0.02795 inches. However, the maximum displacements on the

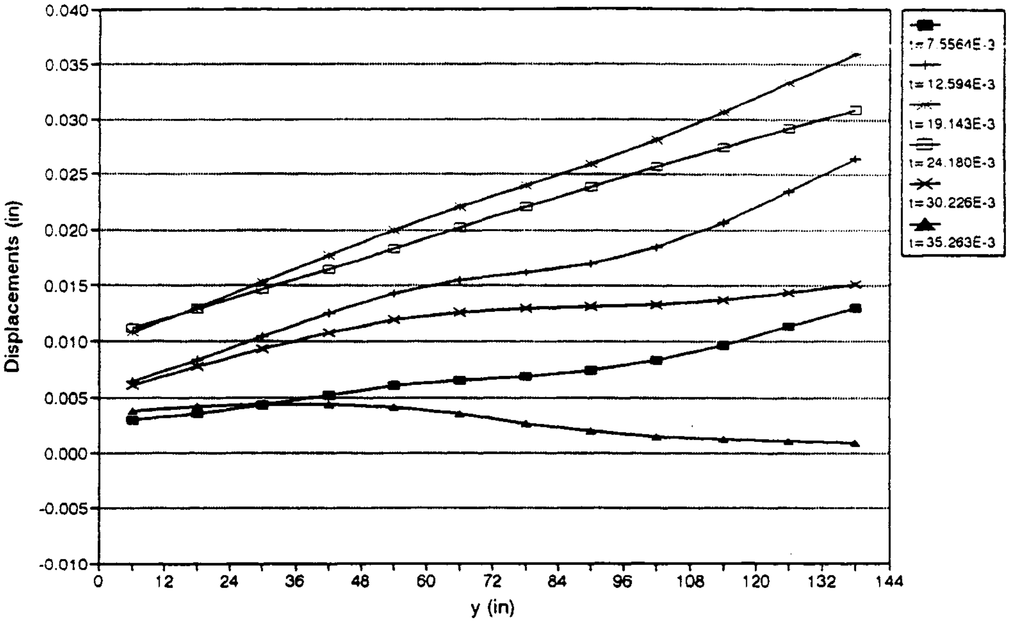

Figure 4.13. Displacements along the joint x = 240.0 inches (loaded side).

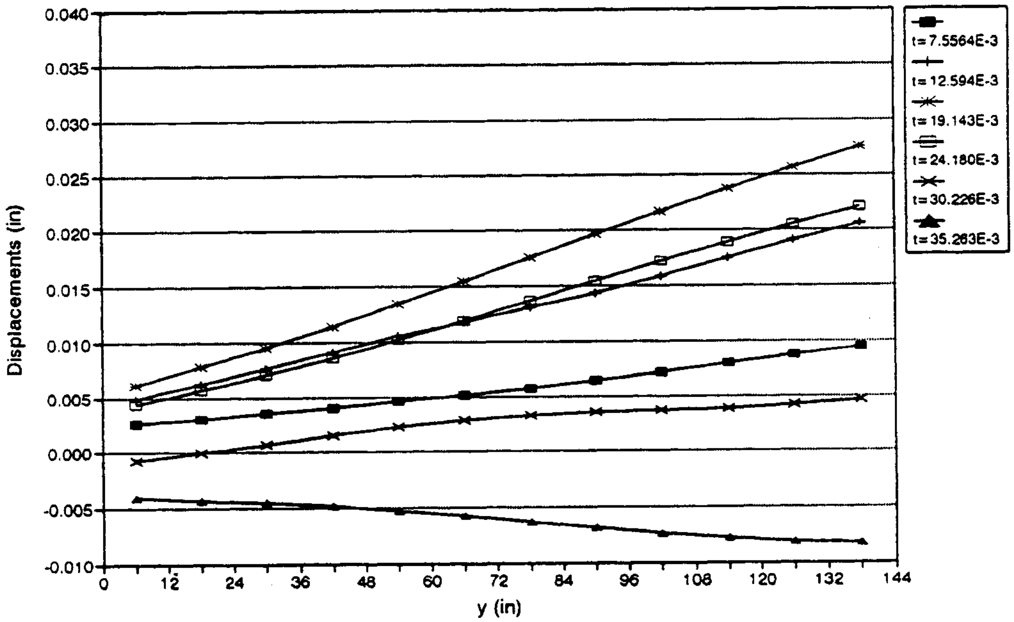

Figure 4.14. Displacements along the joint x = 240.0 inches (unloaded side).

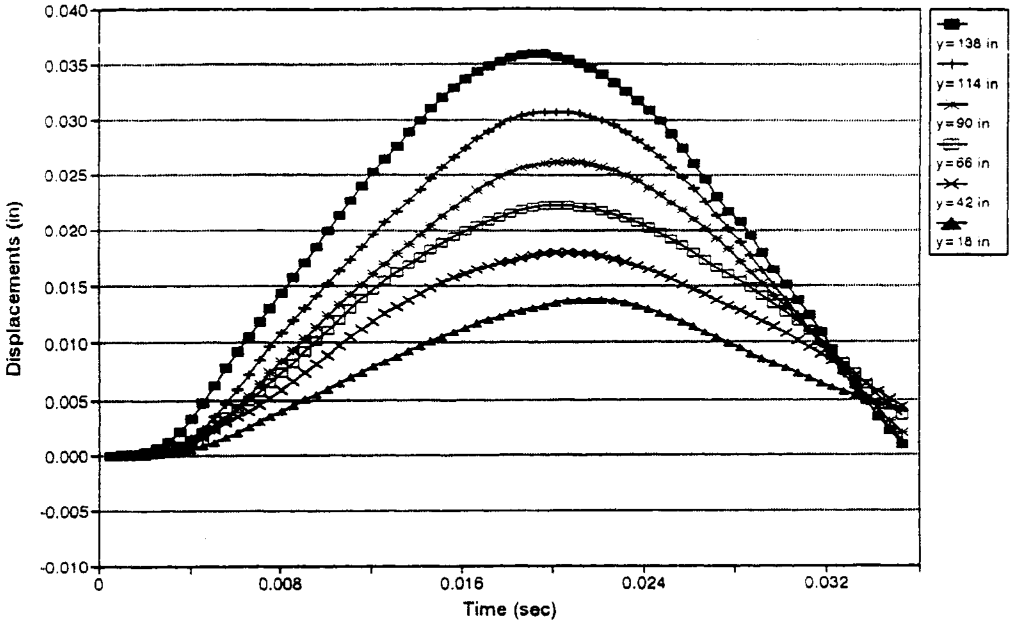

Figure 4.15. Time history of the selected displacements at the joint x = 240.0 inches (loaded side).

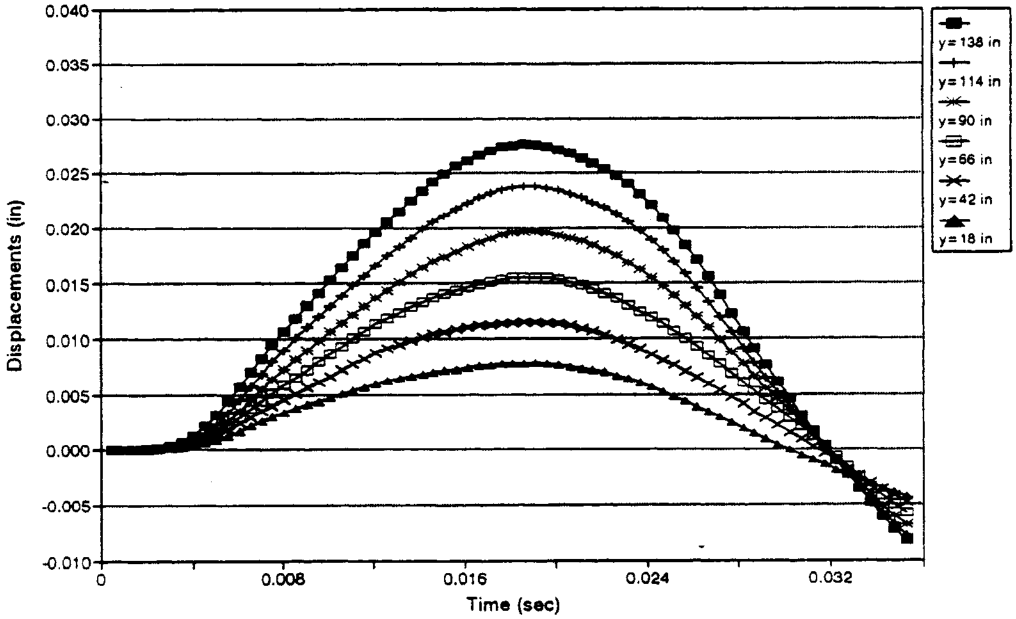

Figure 4.16. Time history of the selected displacements at the joint x = 240.0 inches (unloaded side).

loaded side and on the unloaded side are on the order of 0.0234 inches and 0.0199 inches, respectively, in Guo [1992] (the effects of aggregate interlock are also neglected). The joint efficiency is typically defined as the ratio of the displacement of the unloaded side to displacement of the loaded side of the joint. Therefore the joint efficiencies are (0.02795 / 0.03595) x 100% = 77.75% as obtained by using the program MNSLAB and (0.0199 / 0.0234) x 100% = 85.04% as obtained from Guo [1992]. It is generally desirable to maintain displacement load transfer efficiency above 75 percent to ensure good long-term pavement performance (i.e., to prevent pumping and faulting).

Figure 4.17 presents the comparison of longitudinal stress distributions in the x direction at y = 141.46 inches (y = 144.0 inches for JSLAB (static) case). Due to the effects of the dynamic load, the longitudinal stress distributions are quite different at different times. In Figure 4.17, the longitudinal distribution represented by the filled square symbols was obtained by using the program JSLAB [Guo, 1992], which is a static program. The maximum longitudinal stress in Figure 4.17 for the dynamic load was 189.924 psi which is larger than the static case.

Discussion

The displacements obtained from MNSLAB for both loaded side and unloaded side of the joint are larger than the results in Guo [1992]. The efficiency of load transfer obtained by using MNSLAB is slightly lower than the result in Guo [1992]. As expected the longitudinal stress distributions obtained by using MNSLAB and JSLAB also do not quite match. The reason is that MNSLAB is a dynamic program, which may be closer to a realistic situation, the

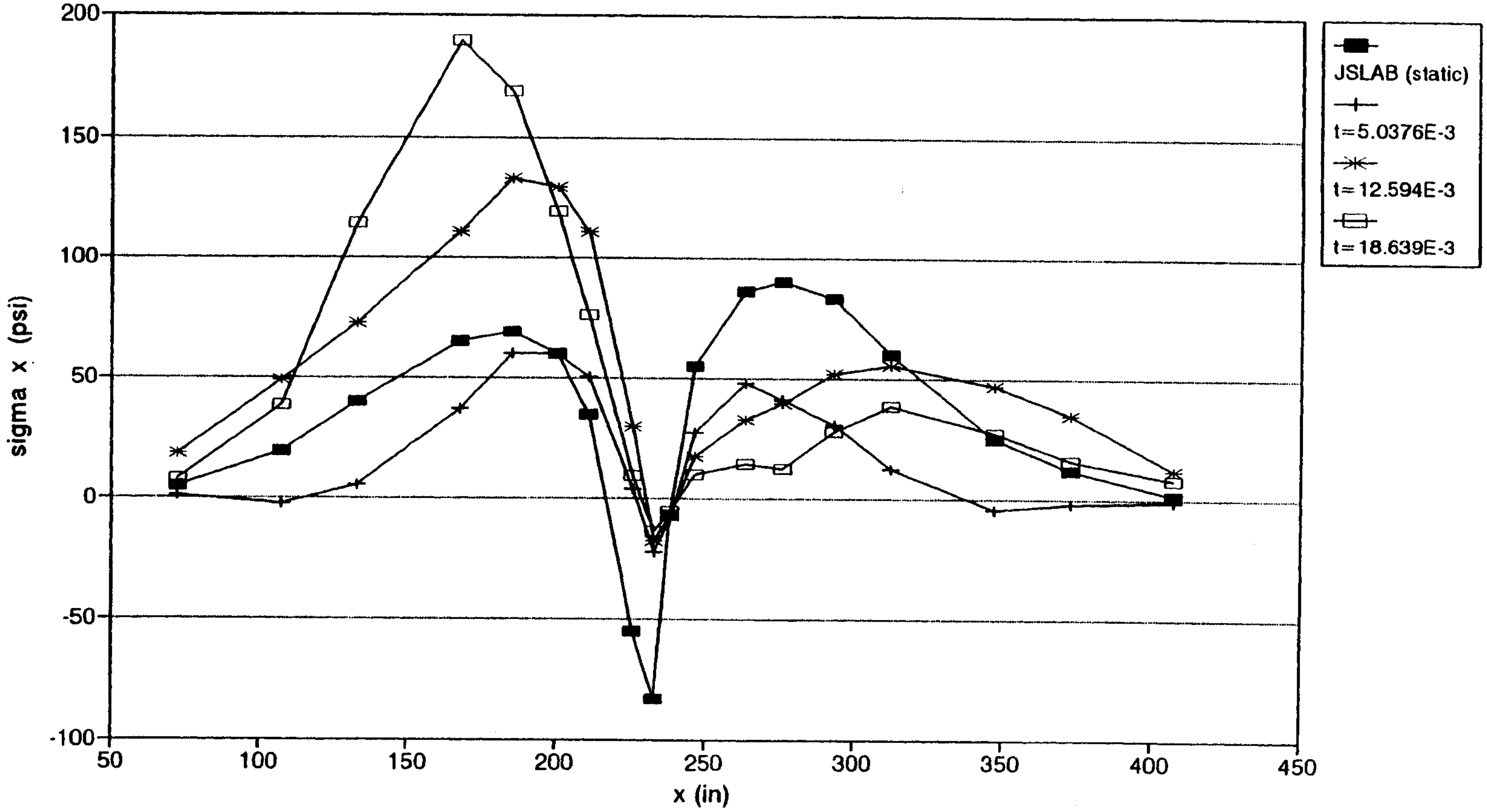

Figure 4.17. Longitudinal stresses along the line y = 141.46 inches (JSLAB (static) case, y = 144.0 inches).

program in Guo [1992] and JSLAB are static programs. Another very important reason may be that each of the above approaches employs the dowel bar stiffness matrix derived by using different methods produces different results. The dowel bar stiffness matrix plays significant role in model and leads to different results. The dowel bar stiffness matrix in MNSLAB was derived theoretically as presented in Appendix D, where the simplifying assumptions are also explained. The dowel bar stiffness matrices in Guo [1992] and JSLAB on the other hand include some adjustable coefficients to fit the empirical results.

For modeling the dowel bar load transfer mechanism, MNSLAB may be a good modeling program. But MNSLAB cannot consider other effects of rigid pavements, such as aggregate interlock, moisture effects, drainability, etc., so MNSLAB needs to be modified further in the future. Further studies with the application of MNSLAB are possible, they may, for example, include effects of different lengths of dowel bars and different dowel bar diameters. These were not included in this report.

CHAPTER 5

CONCLUSIONS AND RECOMMENDATIONS

The program MNROAD which originally modelled linear elastic materials with viscous boundaries, was modified and named MNROAD-93 in which elasto-plastic materials and infinite element boundaries were used for pavements. A new 2-dimensional, linear elastic, dynamic program, MNSLAB, was developed to simulate the load transfer mechanism of rigid pavements. The results obtained from MNROAD-93 were compared with FWD test data, and the results from MNSLAB were compared with the results in Guo [1992].

CONCLUSIONS

MNROAD-93 Model:

1. Among all combinations of linear elastic and elasto-plastic materials (including perfectly plastic, linear hardening, N segments hardening and N segments softening) and viscous boundaries and infinite element boundaries, there was no single combination which would provide consistently good results for problems discussed in this report.
2. In order to obtain better simulated results, accurate material properties are important.
3. Better monitoring the magnitude of the load and its distribution from the experimental results may be necessary. The assumption of uniform load distribution under the plate is probably incorrect.
4. Consideration of slip and separation between different pavement layers might improve the results obtained in the present calculations significantly.

5. An axi-symmetric model may suit the test configuration better, although in reality the geometry of the pavement structure is better modelled by a three-dimensional representation.
6. The infinite element boundaries provide better agreement with experiments than viscous boundaries.
7. Accepting certain errors in the results one can say that the best choice may be the elastic material model and infinite element boundaries.

MNSLAB Model:

1. The calculated displacements on both the loaded and unloaded sides of a joint are larger than results obtained from the static program.
2. The joint efficiency is lower than the results obtained from the static program.
3. The maximum longitudinal stress is almost two times the magnitude of the results obtained from the static program.
4. The longitudinal stress distributions are quite different at different times due to the effects of the dynamic load.
5. The key aspect related to model the dowel bar load transfer system is the proper formulation of the dowel bar stiffness matrix.
6. To further improve the results, incorporation of the aggregate interlock may be necessary.
7. Since the dowel bar length is very small relative to slab dimension and consequent on its high stiffness, the time step in our explicit integration is very small and the total time

needed for calculation is significantly increased. In this context the implicit time integration may turn out to be competitive.

RECOMMENDATIONS

MNROAD-93 Model:

1. The accurate material properties, such as Young'modulus, E, Poisson's ratio, ν, internal friction, ϕ, and cohesion, C, etc., have to be obtained and incorporated into the analysis.
2. The effects of slip and separation between various layers should be investigated.
3. Experimental data with respect to load magnitude, its distribution and its variations with time, has to be better incorporated into analysis.
4. An axi-symmetric model may be considered, it may better suit the experiment configuration.
5. Material non-linearities, such as nonlinear elastic and visco-elastic, have to be considered in the analysis.

MNSLAB Model:

1. The effects of aggregate interlock and a combination of dowel bars and aggregate interlock should be investigated.
2. Another time integration method should be assessed and possibly should replace the central difference method to avoid using the excessive computer time.

3. Many modifications should be made in order to improve MNSLAB capabilities, such as:
    a. Moisture effects and climatic variables.
    b. Consideration of a combination of slabs such as multiple traffic lanes, traffic lanes and shoulders, or a series of transverse cracks.
    c. Variable subgrade support conditions, including complete loss of support at any location or combination of locations beneath the slab.
    d. Other foundations such Vlasov (two-parameter system) and the resilient subgrade formulations.

REFERENCES

ABAQUS, Finite Element Computer Program. Version 4.9. Hibbitt, Karlsson and Sorensen, Inc., 1989.

Barksdale, R.D., "Analysis of Layered Systems," Georgia Institute of Technology, 1969.

Bathe,K-J., "Finite Element Procedures in Engineering Analysis," Prentice-Hall, Inc., 1982.

Chen, W.F., and Han, D.J., "Plasticity for Structural Engineers," Spriner-Verlag, 1988.

Chen, W.F., and Mizuno, E., "Nonlinear Analysis in Soil Mechanics, Theory and Implementation," Developments in Geotechnical Engineering 53, Elsevier, 1990.

Chou, Y.T., "Structural Analysis Computer Programs for Rigid Multi-Component Structures with Discontinuities--WESLIQUID and WESLAYER," Technical Report GL-80, U.S. Army Engineer Waterways Experiment Station, Vicksburg, Miss., Sept. 1980.

Cook, R.D., Malkus, D.S., and Plesha, M.E., "Concepts and Applications of Finite Element Analysis," Third edition, John Wiley & Sons, Inc., New York, 1989.

Duncan, J.M., Monismith, C.L., and Wilson, E.L., "Finite Element Analysis of Pavements," Highway Research Record 228, Highway Research Board, Washington, D.C., 1968.

Guo, E.H., Sherwood, J.A., and Snyder, M.B., "Dowel Bar Modeling in Finite Element Programs for PCC Pavement Analysis," Prepared for workshop on load equivalency, mathematical modeling of PCC pavements, Feb. 25-26, 1992.

Harichandran, R.S., and Yeh, M-S., "Flexible Boundary in Finite Element Analysis of Pavements," Transportation Research Record 1207, TRB, National Research Council, Washington, D.C., 1988, pp. 50-60.

Harichandran, R.S., Yeh, M-S., and Baladi, G.Y., "MICH-PAVE: A Nonlinear Finite Element Program for Analysis of Flexible Pavements," Transportation Research Record 1286, TRB, National Research Council, Washington, D.C., 1990, pp. 123-131.

Heinrichs, K.W., Lui, M.J., Darter, M.I., Carpenter, S.H.,-and Ioannides,A.M., "Rigid Pavement Analysis and Design," Federal Highway Administration, FHWA-RD-88-068, July 1989.

Hicks, R.G., Swait, J.D., Jr., and Chastian, E.O., "Use of Layered Theory in the Design and Evaluation of Pavement Systems," Department of Civil Engineering, Oregon State University, Corvallis, Oregon, January, 1978.

Hoffman, M.S., and Thompson, M.R., "Backcalculating Nonlinear Resilient Moduli from Deflection Data," Transportation Research Record 852, Transportation Research Board, Washington, D.C., 1982, pp. 42-51.

Huang, Y.H. and Wang, S.T., "Finite Element Analysis of Concrete Slabs and Its Implication for Rigid Pavements," Highway Research Record 466, HRB, National Research Council, Washington, D.C., 1973, pp. 55-69.

Hughes, J.R. Thomas., "The Finite Element Method Linear Static and Dynamic Finite Element Analysis," Prentice-Hall, Inc., 1987.

Ioannidis, A.M., Barenberg, E.J., and Thompson, M.R., "Finite Element Model with Stress Dependent Support," Transportation Research Record 954, TRB, National Research Council, Washington, D.C., 1984, pp. 10-16.

Ioannides, A.M., and Donnelly, J.P., "Three-Dimensional Analysis of Slab on Stress-Dependent Foundation," Transportation Research Record 1196, TRB, National Research Council, Washington, D.C., 1988, pp. 72-84.

Kopperman, S., Tiller, G., and Tseng, M., "Purdue Pumping Model: PMARP and PEARDARP Interactive Microcomputer Version," Federal Highway Administration, FHWA Contract DTFH61-85-C-00051, 1986.

Kumar, P., "Analysis of Flexible Pavements Using Finite and Infinite Elements," Australian Road Research, Australian Road Research Board, North Melbourne, Vol. 16, March 1986, pp.18-24.

Larralde, J., "PMARP User's Manual," Federal Highway Administration, FHWA Contract DTFH61-85-C-00051, 1985.

Majidzadeh, K., Ilves, G.J., and Sklyut, H., "Mechanistic Design of Rigid Pavements; Volume I: Development of the Design Procedure; Volume II: Design and Implementation Manual," Federal Highway Administration, FHWA Contract DTFH-11-9568, June 1984.

Marques, J.M.M.C., and Owen, D.R.J., "Infinite Elements in Quasi-Static Materially Nonlinear Problems," Computers & Structeres, Vol. 18, No. 4, 1984, pp.739-751.

Mueller, A.L., Peshkin, D.G., Smith, K.D., and Darter, M.I., "Performance of Jointed Concrete Pavements," Volume VI, FHWA-RD-89-141, July, 1990.

Nasim, M.A., Karamihas, S.M., Gillespie, T.D., Hansen, W., and Cebon, D., "Behavior of a Rigid Pavement Under Moving Dynamic Loads," Transportation Research Record 1307, TRB, National Research Council, Washington, D.C., 1991, pp. 129-135.

Owen, D.R.J., and Hinton,E., "Finite Elements in Plasticity: Theory and Practice," Pineridge Press Limited, Swansea, U. K. 1980.

Prakasha, K.S., "Development of Simulation Software for Finite Modelling of Flexible Pavement Responses," M.S. Thesis, University of Minnesota, Minneapolis, Minnesota, 1990.

Raman, Pichumani, "Application of Computer Codes to the Analysis of Flexible Pavements," Proceedings, Third International Conference on the Structural Design of Asphalt Pavements, 1972, London, England, p 506-520.

Tabatabaie, A.M., and Barenberg, E.J., "Finite Element Analysis of Jointed or Cracked Concrete Pavements," Transportation Research Record 671, TRB, National Research Council, Washington, D.C., 1978, pp. 11-19.

Tayabji, S.D., and Colley, B.E., "Analysis of Jointed Concrete Pavements," Federal Highway Administration, FHWA/RD-86/041, February 1986.

Thompson, M.R., "ILLI-PAVE User's Manual," Transportation Facilities Group, Department of Civil Engineering, University of Illinois, Urbana, Illinois, 1982.

Tia, M., Armaghani, J.M., Wu, C.L., Lei, S., and Toye, K.L., "FEACONS III Computer Program for Analysis of Jointed Concrete Pavements," Transportation Research Record 1136, TRB, National Research Council, Washington, D.C., 1987, pp. 12-22.

Weeks, W., Valliappan, S., and Lee, I.C., "Unified Boundary for Finite Dynamic Models," Journal of the Engineering Mechanics Division, ASCE, Oct. 1977.

Wilson, E.L., "A Digital Computer Program for the Finite Element Analysis of Solids with Non-linear Material properties," University of California, 1965.

Zaghloul, S. and White, T., "Use of a Three-Dimensional, Dynamic Finite Element Program for Analysis of Flexible Pavement," Transportation Research Record 1388, TRB, National Research Council, Washington, D.C., 1993, pp.60-69.

APPENDIX A

FORCE EQUILIBRIUM EQUATION

In the program MNROAD-93, modified from the MNROAD program [Prakasha,1990], the flexible pavement structure is modelled as a three-dimensional, elasto-plastic model, subjected to dynamic loads. The analysis is carried out by solving the force equilibrium equation through the central difference method.

The force equilibrium equation is expressed as

$$\underset{\sim}{M}\,\ddot{\underset{\sim}{d}} + \underset{\sim}{C}\,\dot{\underset{\sim}{d}} + \underset{\sim}{f}^{int}(\underset{\sim}{d}) = \underset{\sim}{f}^{ext}(t) \qquad \text{(A.1)}$$

where

$\underset{\sim}{d}$ = displacement vector

$\dot{\underset{\sim}{d}} = \underset{\sim}{v}$ = velocity vector

$\ddot{\underset{\sim}{d}}$ = acceleration vector

$\underset{\sim}{M}$ = mass matrix (diagonal)

$\underset{\sim}{C}$ = damping coefficient matrix (diagonal)

$\underset{\sim}{f}^{int}(\underset{\sim}{d})$ = nodal internal force vector

$\underset{\sim}{f}^{ext}(t)$ = the applied external force vector

The above matrix differential equation is solved through the central difference method. Each equation, considered at time t_n, has the form

$$\underset{\sim}{M}\,\ddot{\underset{\sim}{d}}_n + \underset{\sim}{C}\,\dot{\underset{\sim}{d}}_n + \underset{\sim}{f}^{int}(\underset{\sim}{d}_n) = \underset{\sim}{f}^{ex}(t_n) \qquad \text{(A.2)}$$

The velocities are averaged based on the finite difference formula since, as shown below, this formula uses velocities at the half step.

$$\underset{\sim}{M}\,\ddot{\underset{\sim}{d}}_{n} + \underset{\sim}{C}\,\frac{\dot{\underset{\sim}{d}}_{n-\frac{1}{2}} + \dot{\underset{\sim}{d}}_{n+\frac{1}{2}}}{2} + \underset{\sim}{f}^{int}(\underset{\sim}{d}_{n}) = \underset{\sim}{f}^{ext}(t_n) \tag{A.3}$$

Since

$$\dot{\underset{\sim}{d}}_{n+\frac{1}{2}} = \dot{\underset{\sim}{d}}_{n-\frac{1}{2}} + \Delta t\,\ddot{\underset{\sim}{d}}_{n} \tag{A.4}$$

where Δt is the time step increment, the following expression is obtained

$$(\underset{\sim}{M} + \frac{\Delta t}{2}\underset{\sim}{C})\,\ddot{\underset{\sim}{d}}_{n} + \underset{\sim}{C}\,\dot{\underset{\sim}{d}}_{n-\frac{1}{2}} + \underset{\sim}{f}^{int}(\underset{\sim}{d}_{n}) = \underset{\sim}{f}^{ext}(t_n) \tag{A.5}$$

If $\underset{\sim}{d}_{n}$ is known, the displacement vector at the next time step, $\underset{\sim}{d}_{n+1}$ can be calculated using the relationship

$$\begin{aligned} \underset{\sim}{d}_{n+1} = {} & (\Delta t)^2\,[\underset{\sim}{M} + (\frac{\Delta t}{2})\,\underset{\sim}{C}]^{-1}\,[\underset{\sim}{f}^{ext}(t_n) - \underset{\sim}{f}^{int}(\underset{\sim}{d}_{n}) \\ & - \underset{\sim}{C}\,\dot{\underset{\sim}{d}}_{n-\frac{1}{2}}] + \Delta t\,\dot{\underset{\sim}{d}}_{n-\frac{1}{2}} + \underset{\sim}{d}_{n} \end{aligned} \tag{A.6}$$

This takes into account the lag of the velocity vector by half-time step.

APPENDIX B

ELASTO-PLASTIC MATERIAL MODEL

EVALUATION OF INTERNAL FORCE VECTOR

The internal force vector for each element can be evaluated by

$$\underset{\sim}{f}^{int} = \int_{\Omega} \underset{\sim}{B}^{T} \underset{\sim}{\sigma} \, d\Omega \tag{B.1}$$

where

$\underset{\sim}{B}$ = the standard B matrix which relates strains and displacements

$\underset{\sim}{\sigma}$ = stress vector

Ω = the element volume

If the pavement material is considered to be linear elastic

$$\underset{\sim}{\sigma} = \underset{\sim}{D} \, \underset{\sim}{\epsilon} \tag{B.2}$$

$$\underset{\sim}{\epsilon} = \underset{\sim}{B} \, \underset{\sim}{d} \tag{B.3}$$

where

$\underset{\sim}{D}$ = the constitutive matrix representing material properties which include Young's modulus E and Poisson's ratio ν

$\underset{\sim}{\epsilon}$ = strain vector

If the pavement material is considered to be elasto-plastic

$$\underset{\sim}{\sigma} = \underset{\sim}{D} \, \underset{\sim}{\epsilon}^{e} \tag{B.4}$$

$$\underset{\sim}{\epsilon}^{e} = \underset{\sim}{\epsilon} - \epsilon^{p} \tag{B.5}$$

where

$\underset{\sim}{\epsilon}^{e}$ = elastic strain vector

$\underset{\sim}{\epsilon}^{p}$ = plastic strain vector

The plastic strain vector can be evaluated according to the associated flow rule. The associated flow rule can be written in the form

$$\underset{\sim}{\epsilon}^{p} = \lambda \frac{\partial F}{\partial \underset{\sim}{\sigma}} \tag{B.6}$$

where

λ = a positive scalar factor of proportionality

F = a yield function

INCREMENTAL STRESS-STRAIN RELATIONSHIPS

In an elasto-plastic analysis by a numerical approach, the most common technique is the incremental method [Chen,1988, pp. 207].

The elastic strain increment vector is equal to the total strain increment vector minus the plastic strain increment vector

$$\Delta \underset{\sim}{\epsilon}^{e} = \Delta \underset{\sim}{\epsilon} - \Delta \underset{\sim}{\epsilon}^{p} \tag{B.7}$$

where

$$\Delta \underset{\sim}{\epsilon} = \underset{\sim}{B} \, \Delta \underset{\sim}{d} \tag{B.8}$$

$$\Delta \underset{\sim}{\epsilon}^{p} = \Delta\lambda \frac{\partial F}{\partial \underset{\sim}{\sigma}} \tag{B.9}$$

The stress increment vector can be expressed as

$$\Delta \underset{\sim}{\sigma} = \underset{\sim}{D}\, \Delta \underset{\sim}{\epsilon}^{e} = \underset{\sim}{D}\, (\Delta \underset{\sim}{\epsilon} - \Delta\lambda \frac{\partial F}{\partial \underset{\sim}{\sigma}}) \tag{B.10}$$

The stress vector at time t_{n+1} can be calculated by

$$\underset{\sim}{\sigma}_{n+1} = \underset{\sim}{\sigma}_{n} + \Delta \underset{\sim}{\sigma} \tag{B.11}$$

YIELD CRITERION

The yield criterion can generally be expressed as [Chen, 1988, pp. 72]

$$F\,(\underset{\sim}{\sigma}, k_1, k_2 \ldots) = 0 \tag{B.12}$$

where k_1, k_2 ... are material constants.

For practical purposes, a smooth surface is often used to approximate the yield surface with singularities in elasto-plastic finite-element analyses under a more general stress condition. The Drucker-Prager criterion has been established as an approximation of the Coulomb criterion by a simple smooth function. It has the simple form (Figure B.1) [Chen and Mizuno, 1990, pp.143-146]

$$F = \alpha\, I_1 + \sqrt{J_2} - \kappa \tag{B.13}$$

where

α, κ = two material constants

I_1 = the first invariant of stress tensor

J_2 = the second invariant of deviatoric stress tensor

$$I_1 = \sigma_{xx} + \sigma_{yy} + \sigma_{zz} \tag{B.14}$$

$$J_2 = \frac{1}{6} [(\sigma_{xx} - \sigma_{yy})^2 + (\sigma_{yy} - \sigma_{zz})^2 + (\sigma_{zz} - \sigma_{xx})^2] + \sigma_{xy}^2 + \sigma_{yz}^2 + \sigma_{zx}^2 \tag{B.15}$$

The two Drucker-Prager parameters α and κ can be expressed by the given Coulomb constants C and ϕ, cohesion and internal friction, respectively. In the three dimensional principal stress space, the Drucker-Prager criterion can be matched with the apex of the Coulomb criterion for either Point A or B on its π-plane as shown in Figure B.2. So the parameters α and κ, which correspond to the outer cone, are

$$\alpha = \frac{2 \sin \phi}{\sqrt{3}\ (3 - \sin \phi)} \tag{B.16}$$

$$\kappa = \frac{6\ C \cos \phi}{\sqrt{3}\ (3 - \sin \phi)} \tag{B.17}$$

The parameters α and κ, which correspond to the inner cone, are

$$\alpha = \frac{2 \sin \phi}{\sqrt{3}\ (3 + \sin \phi)} \tag{B.18}$$

$$\kappa = \frac{6\ C \cos \phi}{\sqrt{3}\ (3 + \sin \phi)} \tag{B.19}$$

PERFECTLY PLASTIC MODEL

In the most fundamental sense, the subgrade of the pavement behaves as an elasto-plastic

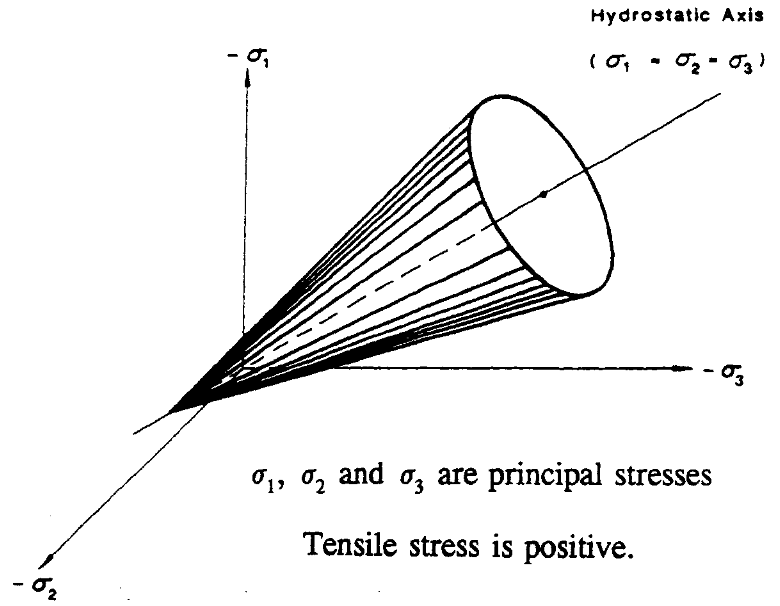

σ_1, σ_2 and σ_3 are principal stresses

Tensile stress is positive.

Figure B.1. Drucker-Prager criterion [after Chen and Mizuno, 1988].

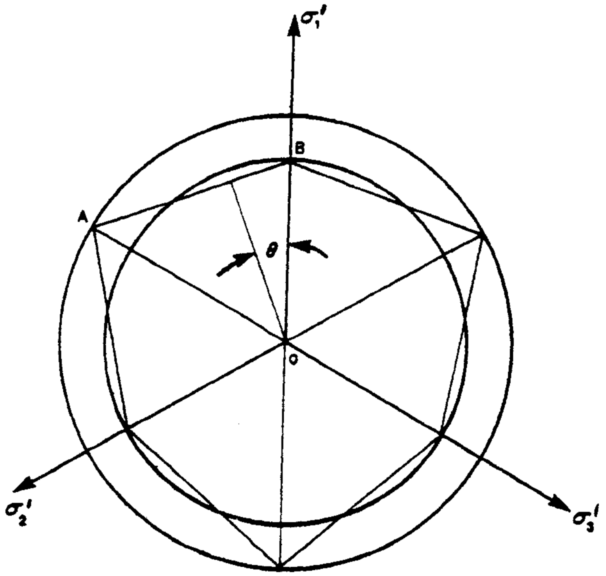

Figure B.2. Shape of yield criterion on the π-plane [after Chen and Mizuno, 1990].

material, i.e., soil deformations are basically inelastic since upon load removal, unloading follows an entirely different path from that followed by loading. For soils, perfect plasticity is used as a design simplification, while more complex stress-strain behaviors of soil may be approximated by the more sophisticated hardening plasticity theory.

The stress vector σ^* is on the yield surface if

$$F\,(\underset{\sim}{\sigma}^*) = 0 \tag{B.20}$$

The stress vector $\underset{\sim}{\sigma}^* + \Delta\underset{\sim}{\sigma}$ existing after the incremental change $\Delta\underset{\sim}{\sigma}$ has taken place still satisfies the yield criterion. Therefore, the following consistency condition must be satisfied.

$$F\,(\underset{\sim}{\sigma}^* + \Delta\underset{\sim}{\sigma}) \approx F\,(\underset{\sim}{\sigma}^*) + \{\frac{\partial F}{\partial \underset{\sim}{\sigma}}|_{\underset{\sim}{\sigma}^*}\}^T \Delta\underset{\sim}{\sigma} = 0 \tag{B.21}$$

From Eqs.(B.20) and (B.21), the linearized consistency condition is obtained in the form

$$\{\frac{\partial F}{\partial \underset{\sim}{\sigma}}|_{\underset{\sim}{\sigma}^*}\}^T \Delta\underset{\sim}{\sigma} = 0 \tag{B.22}$$

Substituting Eq.(B.10) into Eq.(B.22),

$$\Delta\lambda = \frac{\{\frac{\partial F}{\partial \underset{\sim}{\sigma}}|_{\underset{\sim}{\sigma}^*}\}^T \underset{\sim}{D}\, \Delta\underset{\sim}{\epsilon}}{\{\frac{\partial F}{\partial \underset{\sim}{\sigma}}|_{\underset{\sim}{\sigma}^*}\}^T \underset{\sim}{D}\, \{\frac{\partial F}{\partial \underset{\sim}{\sigma}}|_{\underset{\sim}{\sigma}^*}\}} \;. \tag{B.23}$$

WORK-HARDENING MODEL

For the work-hardening material, the Drucker-Prager yield function can be expressed as

$$F\,(\underset{\sim}{\sigma},\ \kappa\,(e^p)\,) = \alpha\, I_1 + \sqrt{J_2} - \kappa\,(e^p) \tag{B.24}$$

where e^p is the effective plastic strain given by

$$e^p = \sqrt{\frac{2}{3}\{\underset{\sim}{\epsilon}^p\}^T\ \underset{\sim}{\epsilon}^p} \tag{B.25}$$

Its incremental form is

$$\Delta e^p = \sqrt{\frac{2}{3}\{\Delta \underset{\sim}{\epsilon}^p\}^T\ \Delta \underset{\sim}{\epsilon}^p} \tag{B.26}$$

At time t_{n+1}, the effective plastic strain is

$$e^p_{n+1} = e^p_n + \Delta e^p \tag{B.27}$$

Usually, κ can be expressed as

$$\kappa = \kappa_0 + H'\, e^p \tag{B.28}$$

where

κ_0 = the same expression as κ in Eq.(B.17) or Eq.(B.19)

H' = the plastic modulus

The consistency condition for an isotropic work-hardening material is

$$\Delta F = \{\frac{\partial F}{\partial \underset{\sim}{\sigma}}|_{\underset{\sim}{\sigma}^*}\}^T\ \Delta \underset{\sim}{\sigma} + \frac{\partial F}{\partial \kappa}\ \Delta \kappa = 0 \tag{B.29}$$

From Eq.(B.28), using Eq.(B.26) and the flow rule Eq.(B.9),

$$\Delta\kappa = H\,\Delta e^{p} = H\,\Delta\lambda\sqrt{\frac{2}{3}\{\frac{\partial F}{\partial \underset{\sim}{\sigma}}|_{\underset{\sim}{\sigma}^{*}}\}^{T}\{\frac{\partial F}{\partial \underset{\sim}{\sigma}}|_{\underset{\sim}{\sigma}^{*}}\}} \tag{B.30}$$

From the Eq.(B.24),

$$\frac{\partial F}{\partial \kappa} = -1 \tag{B.31}$$

Substituting Eq.(B.10), Eq.(B.30) and Eq.(B.31) into Eq.(B.29), $\Delta\lambda$ is obtained

$$\Delta\lambda = \frac{\{\frac{\partial F}{\partial \underset{\sim}{\sigma}}|_{\underset{\sim}{\sigma}^{*}}\}^{T}\underset{\sim}{D}\,\Delta\underset{\sim}{\epsilon}}{\{\frac{\partial F}{\partial \underset{\sim}{\sigma}}|_{\underset{\sim}{\sigma}^{*}}\}^{T}\underset{\sim}{D}\{\frac{\partial F}{\partial \underset{\sim}{\sigma}}|_{\underset{\sim}{\sigma}^{*}}\} + H\sqrt{\frac{2}{3}\{\frac{\partial F}{\partial \underset{\sim}{\sigma}}|_{\underset{\sim}{\sigma}^{*}}\}^{T}\{\frac{\partial F}{\partial \underset{\sim}{\sigma}}|_{\underset{\sim}{\sigma}^{*}}\}}} \tag{B.32}$$

EVALUATION OF THE STRESS VECTOR $\underset{\sim}{\sigma}^{*}$

In Figure B.3, the following relationship is evident

$$\underset{\sim}{\sigma}^{trial}_{n+1} = \underset{\sim}{\sigma}_{n} + \Delta\underset{\sim}{\sigma}^{trial} \tag{B.33}$$

where

$$\Delta\underset{\sim}{\sigma}^{trial} = \underset{\sim}{D}\,\Delta\underset{\sim}{\epsilon} \tag{B.34}$$

The stress vector $\underset{\sim}{\sigma}^{*}$ on the yield surface can be calculated

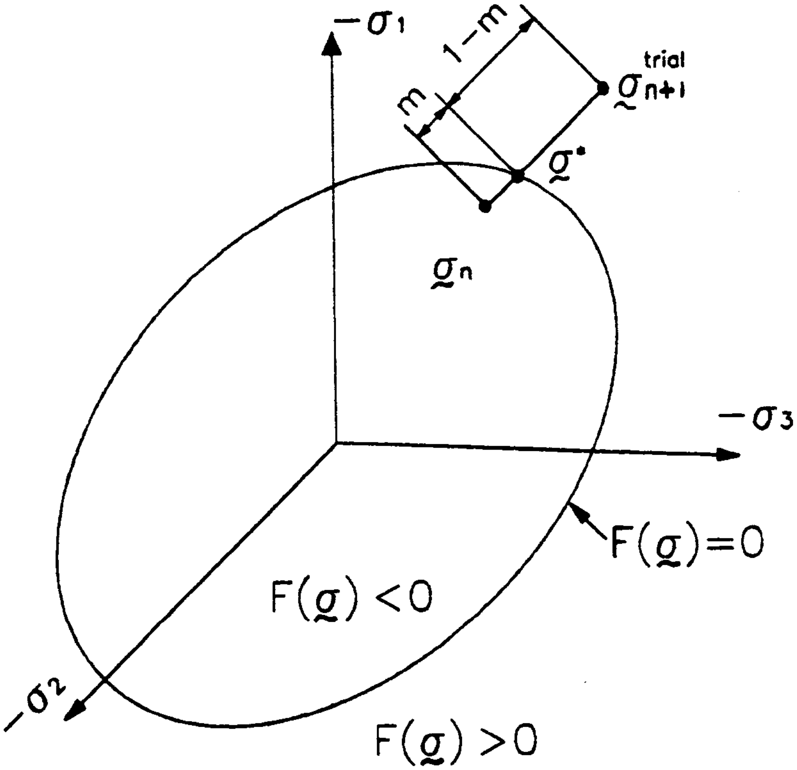

Figure B.3. The stress vector $\underset{\sim}{\sigma}^*$.

$$\underset{\sim}{\sigma}^{*} = \underset{\sim}{\sigma}_{n} (1 - m) + \underset{\sim}{\sigma}^{trial}_{n+1} m \tag{B.35}$$

Substituting Eq.(B.35) into Eq.(B.20), m can be calculated.

APPENDIX C

INFINITE ELEMENTS

INTRODUCTION

One of the problems in dynamic pavement simulation is the elimination of the wave reflection from the boundaries of the model. Viscous boundaries accomplish that to some extent but the use of infinite elements seems to be an alternative that should be explored. The subgrade layer of a pavement structure is an unbounded medium. A finite element model must be terminated somewhere short of infinity. Simple truncation at a rigid boundary is usually adequate in static problems. However, it is unclear where the rigid boundary should be placed, and the analysis may be expensive because many elements are used. In dynamic problems a rigid boundary reflects a wave, regardless of the size of the mesh, therefore, the model misrepresents reality.

In formulating an infinite element, one makes use of two sets of shape functions. These are the standard shape functions $[N]$ and "growth" shape functions $[M]$, which grow without limit as a coordinate approaches infinity. $[N]$ is applied to the field variable and $[M]$ to geometry, so that the element grows to infinite size. This method yields what are called "mapped" infinite elements [Cook et al., 1989].

ONE DIMENSIONAL MAPPED INFINITE ELEMENT

The one dimensional element [Marques and Owen,1984] forms the basis of the three-dimensional versions described subsequently. The element extending from node 1 through node 2 to the point 3 at infinity is mapped as illustrated in Figures C.1.(a)(b) onto the parent element defined by the local coordinate system $-1 \leq \xi \leq 1$. The position of the pole, 0, is arbitrary with $x_0 \leq x_1$. The interpolation from local to global positions can be performed in the standard

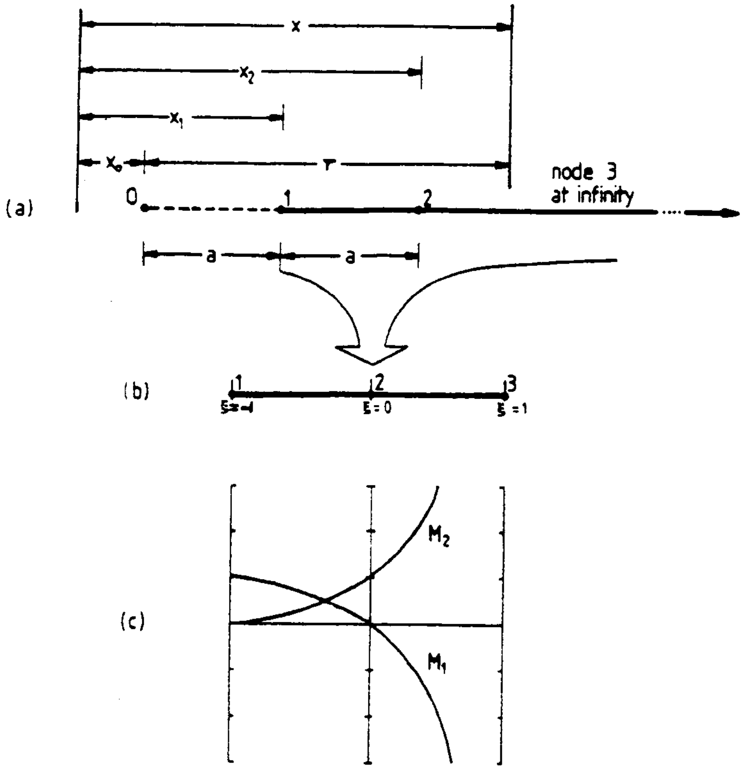

(a) Global representation

(b) Local representation

(c) Geometric mapping functions

Figure C.1. One dimensional infinite element

[after Marques and Owen, 1984].

finite element manner as

$$x\ (\xi) = \sum_{i=1}^{2} M_i(\xi)\ x_i \tag{C.1}$$

where summation extends over the finite nodes only and the mapping functions M_i are given by

$$\begin{aligned} M_1\ (\xi) &= -2\xi\ /\ (1 - \xi) \\ M_2\ (\xi) &= (1 + \xi)\ /\ (1 - \xi) \end{aligned} \tag{C.2}$$

Examining the above mapping, it can be readily seen that $\xi = -1,\ 0,\ +1$ correspond respectively to the global positions $x = x_1,\ x_2,\ \infty$. Shape functions M_1 and M_2 are shown in Figure C.1.(c). The requirement that the mapping must be independent of the choice of coordinate system necessitates that $M_1 + M_2 = 1$.

The basic field variable ϕ can be interpolated using standard shape functions which for the three-nodes element of Figure C.1 gives

$$\phi = \sum_{i=1}^{3} N_i(\xi)\ \phi_i \tag{C.3}$$

where the standard shape functions are given by

$$\begin{aligned} N_1(\xi) &= \frac{1}{2}\xi(\xi - 1) \\ N_2(\xi) &= 1 - \xi^2 \\ N_3(\xi) &= \frac{1}{2}\xi(\xi + 1) \end{aligned} \tag{C.4}$$

THREE DIMENSIONAL MAPPED INFINITE ELEMENTS

Extension of the procedure described in the previous section to three-dimensional situations can be accomplished by taking shape function products [Marques and Owen, 1984]. Elements may be generated which are singly, doubly or triply infinite.

Singly Infinite Element

The singly infinite element is used to denote elements which extend to infinity in one direction only (chosen to be the ζ direction). The 8-node Lagrangian isoparametric element is shown in Figure C.2 and its shape and mapping functions are shown in Table C.1. This element is regarded as a 12-node Lagrangian finite element in which the four nodes associated with $\zeta = +1$ are positioned at infinity, bilinear in ξ and η and quadratic in ζ. The eight shape functions $N_i(\xi, \eta, \zeta)$ are the appropriate finite elements values. The mapping functions $M_i(\xi, \eta, \zeta)$ are a product of linear expressions $M_j'(\xi)$ in the ξ direction, $M_k''(\eta)$ in the η direction and singularity functions $M_l'''(\zeta)$ of the same form as Eq.(C.2) in the ζ direction. In particular

$$\begin{aligned} M_1'(\xi) &= (1-\xi)/2 \qquad \xi_i = -1 \\ M_2'(\xi) &= (1+\xi)/2 \qquad \xi_i = +1 \end{aligned} \tag{C.5}$$

$$\begin{aligned} M_1''(\eta) &= (1-\eta)/2 \qquad \eta_i = -1 \\ M_2''(\eta) &= (1+\eta)/2 \qquad \eta_i = +1 \end{aligned} \tag{C.6}$$

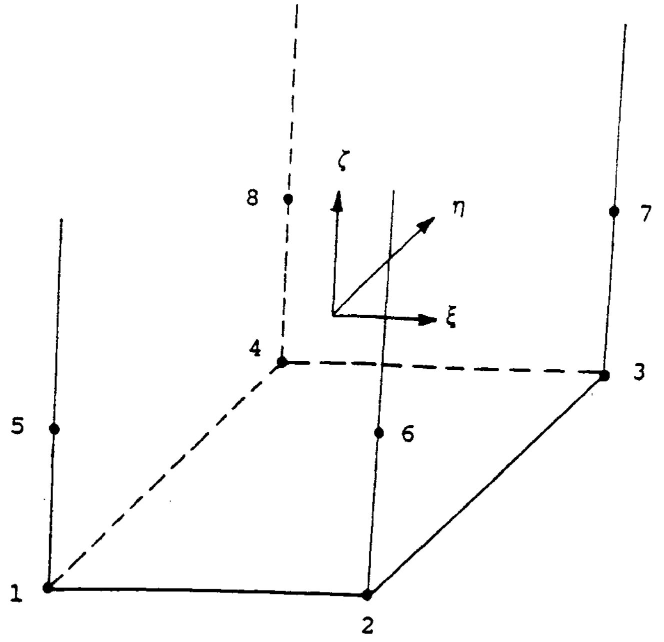

Figure C.2. Singly infinite 8-node Lagrangian isoparametric element.

Table C.1. Shape and mapping functions for 3-D singly infinite element.

Shape Functions	Mapping Functions
$N_1=(1-\xi)(1-\eta)(\zeta\zeta-\zeta)/8$	$M_1=(1-\xi)(1-\eta)(-\zeta)/[2(1-\zeta)]$
$N_2=(1+\xi)(1-\eta)(\zeta\zeta-\zeta)/8$	$M_2=(1+\xi)(1-\eta)(-\zeta)/[2(1-\zeta)]$
$N_3=(1+\xi)(1+\eta)(\zeta\zeta-\zeta)/8$	$M_3=(1+\xi)(1+\eta)(-\zeta)/[2(1-\zeta)]$
$N_4=(1-\xi)(1+\eta)(\zeta\zeta-\zeta)/8$	$M_4=(1-\xi)(1+\eta)(-\zeta)/[2(1-\zeta)]$
$N_5=(1-\xi)(1-\eta)(1-\zeta\zeta)/4$	$M_5=(1-\xi)(1-\eta)(1+\zeta)/[4(1-\zeta)]$
$N_6=(1+\xi)(1-\eta)(1-\zeta\zeta)/4$	$M_6=(1+\xi)(1-\eta)(1+\zeta)/[4(1-\zeta)]$
$N_7=(1+\xi)(1+\eta)(1-\zeta\zeta)/4$	$M_7=(1+\xi)(1+\eta)(1+\zeta)/[4(1-\zeta)]$
$N_8=(1-\xi)(1+\eta)(1-\zeta\zeta)/4$	$M_8=(1-\xi)(1+\eta)(1+\zeta)/[4(1-\zeta)]$

$$
\begin{array}{ll}
M_1'''(\zeta) = -2\zeta / (1 - \zeta) & \zeta_i = -1 \\
M_2'''(\zeta) = (1 + \zeta) / (1 - \zeta) & \zeta_i = 0
\end{array}
\tag{C.7}
$$

Doubly Infinite Element

The doubly infinite element is used to denote elements which extend to infinity in two directions. They can be used as "edge" elements in a mesh where transition is needed between zones extending to infinity along different directions. The 8-node Lagrangian isoparametric element is shown in Figure C.3 and its shape and mapping functions are shown in Table C.2. This element originates from the 18-node Lagrangian finite element in which the ten nodes associated with $\xi = +1$ and $\eta = +1$ are positioned at infinity, quadratic in ξ and η and linear in ζ. The eight shape functions $N_i(\xi, \eta, \zeta)$ are appropriately selected from the 18-node Lagrangian finite element. The both auxiliary functions $M_j'(\xi)$ and $M_k''(\eta)$ exhibit singular values for ξ and η equal to $+1$ and are given, from Eq.(C.2), by

$$
\begin{array}{ll}
M_1'(\xi) = -2\xi / (1 - \xi) & \xi_i = -1 \\
M_2'(\xi) = (1 + \xi) / (1 - \xi) & \xi_i = 0
\end{array}
\tag{C.8}
$$

$$
\begin{array}{ll}
M_1''(\eta) = -2\eta / (1 - \eta) & \eta_i = -1 \\
M_2''(\eta) = (1 + \eta) / (1 - \eta) & \eta_i = 0
\end{array}
\tag{C.9}
$$

The linear functions $M_l'''(\zeta)$ have the same form as Eq.(C.5).

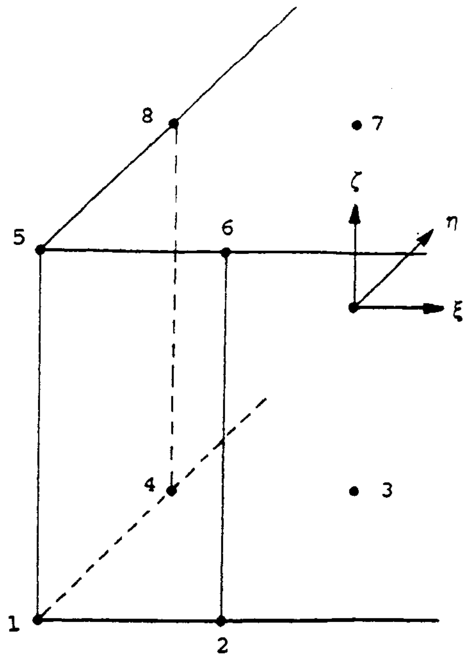

Figure C.3. Doubly infinite 8-node Lagrangian isoparametric element.

Table C.2. Shape and mapping functions for 3-D doubly infinite element.

Shape Functions	Mapping Functions
$N_1=(\xi\xi-\xi)(\eta\eta-\eta)(1-\zeta)/8$	$M_1=2\xi\eta(1-\zeta)/[(1-\xi)(1-\eta)]$
$N_2=(1-\xi\xi)(\eta\eta-\eta)(1-\zeta)/4$	$M_2=(1+\xi)(-\eta)(1-\zeta)/[(1-\xi)(1-\eta)]$
$N_3=(1-\xi\xi)(1-\eta\eta)(1-\zeta)/2$	$M_3=(1+\xi)(1+\eta)(1-\zeta)/[2(1-\xi)(1-\eta)]$
$N_4=(\xi\xi-\xi)(1-\eta\eta)(1-\zeta)/4$	$M_4=(-\xi)(1+\eta)(1-\zeta)/[(1-\xi)(1-\eta)]$
$N_5=(\xi\xi-\xi)(\eta\eta-\eta)(1+\zeta)/8$	$M_5=2\xi\eta(1+\zeta)/[(1-\xi)(1-\eta)]$
$N_6=(1-\xi\xi)(\eta\eta-\eta)(1+\zeta)/4$	$M_6=(1+\xi)(-\eta)(1+\zeta)/[(1-\xi)(1-\eta)]$
$N_7=(1-\xi\xi)(1-\eta\eta)(1+\zeta)/2$	$M_7=(1+\xi)(1+\eta)(1+\zeta)/[2(1-\xi)(1-\eta)]$
$N_8=(\xi\xi-\xi)(1-\eta\eta)(1+\zeta)/4$	$M_8=(-\xi)(1+\eta)(1+\zeta)/[(1-\xi)(1-\eta)]$

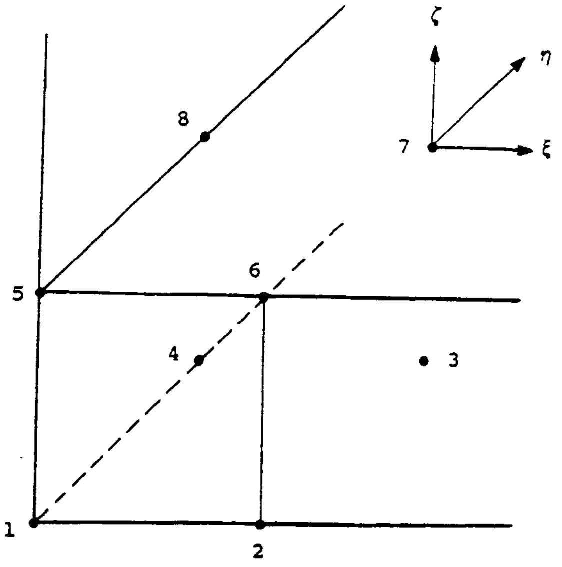

Figure C.4. Triply infinite 8-node Lagrangian isoparametric element.

Table C.3. Shape and mapping functions for 3-D triply infinite element.

Shape Functions	Mapping Functions
$N_1=(\xi\xi-\xi)(\eta\eta-\eta)(\zeta\zeta-\zeta)/8$	$M_1=-8\xi\eta\zeta/[(1-\xi)(1-\eta)(1-\zeta)]$
$N_2=(1-\xi\xi)(\eta\eta-\eta)(\zeta\zeta-\zeta)/4$	$M_2=4(1+\xi)\eta\zeta/[(1-\xi)(1-\eta)(1-\zeta)]$
$N_3=(1-\xi\xi)(1-\eta\eta)(\zeta\zeta-\zeta)/2$	$M_3=-2(1+\xi)(1+\eta)\zeta/[(1-\xi)(1-\eta)(1-\zeta)]$
$N_4=(\xi\xi-\xi)(1-\eta\eta)(\zeta\zeta-\zeta)/4$	$M_4=4\xi(1+\eta)\zeta/[(1-\xi)(1-\eta)(1-\zeta)]$
$N_5=(\xi\xi-\xi)(\eta\eta-\eta)(1-\zeta\zeta)/4$	$M_5=4\xi\eta(1+\zeta)/[(1-\xi)(1-\eta)(1-\zeta)]$
$N_6=(1-\xi\xi)(\eta\eta-\eta)(1-\zeta\zeta)/2$	$M_6=-2(1+\xi)\eta(1+\zeta)/[(1-\xi)(1-\eta)(1-\zeta)]$
$N_7=(1-\xi\xi)(1-\eta\eta)(1-\zeta\zeta)$	$M_7=(1+\xi)(1+\eta)(1+\zeta)/[(1-\xi)(1-\eta)(1-\zeta)]$
$N_8=(\xi\xi-\xi)(1-\eta\eta)(1-\zeta\zeta)/2$	$M_8=-2\xi(1+\eta)(1+\zeta)/[(1-\xi)(1-\eta)(1-\zeta)]$

Triply Infinite Element

The triply infinite element is used to denote elements which extend to infinity in three directions. They can be used as "corner" elements in a mesh where transition is needed between zones extending to infinity along different directions. The 8-node Lagrangian isoparametric element is shown in Figure C.4 and its shape and mapping functions are shown in Table C.3. This element may be regarded as a 27-node Lagrangian finite element in which the nineteen nodes associated with $\xi = +1$, $\eta = +1$ and $\zeta = +1$ are positioned at infinity, quadratic in ξ, η and ζ. The eight shape functions $N_i(\xi, \eta, \zeta)$ are appropriately selected from the 27-node Lagrangian finite element. The auxiliary functions $M'_j(\xi)$, $M''_k(\eta)$ and $M'''_l(\zeta)$ exhibit singular values for ξ, η and ζ equal to $+1$ and are given, from Eq.(C.2), by

$$\begin{aligned} M'_1(\xi) &= -2\xi \,/\, (1 - \xi) & \xi_i &= -1 \\ M'_2(\xi) &= (1 + \xi) \,/\, (1 - \xi) & \xi_i &= 0 \end{aligned} \tag{C.10}$$

$$\begin{aligned} M''_1(\eta) &= -2\eta \,/\, (1 - \eta) & \eta_i &= -1 \\ M''_2(\eta) &= (1 + \eta) \,/\, (1 - \eta) & \eta_i &= 0 \end{aligned} \tag{C.11}$$

$$\begin{aligned} M'''_1(\zeta) &= -2\zeta \,/\, (1 - \zeta) & \zeta_i &= -1 \\ M'''_2(\zeta) &= (1 + \zeta) \,/\, (1 - \zeta) & \zeta_i &= 0 \end{aligned} \tag{C.12}$$

APPENDIX D

JOINTED CONCRETE PAVEMENT MODEL

INTRODUCTION

Jointed concrete pavement is modelled in a two-dimensional (plates are usually discretized into two-dimensional finite element elements such as Mindlin element and Kirchhoff element), linear elastic model (Figure D.1), subjected to dynamic loads. The model consists of nine-node Lagrangian quadratic elements. Only one layer (slab) can be modelled. The subbase and subgrade are considered as a Winkler foundation by the composite modulus of subgrade reaction, k. Slabs are assumed to be connected with dowel bars, which are represented in such way that the relative deformation between the dowel bars and the concrete slabs is taken into account. The analysis is carried out by solving the force equilibrium equation through the central difference method as described in the first section of this chapter. The force equilibrium equations are solved to find the displacements field, which in turn are used to calculate the stresses and strains field.

The complete finite element model for analysis of pavement response consists of the following two submodels

1. Concrete Slabs Connected by Dowel Bars Model;
2. Dowel Bar and Slab Interaction Analysis Model.

CONCRETE SLABS CONNECTED BY DOWEL BARS MODEL

Quadratic Elements and Shape Functions

The slab is divided into 9-node quadrilateral elements (Figure D.2). The quadratic Lagrange shape functions are used in the analysis. Shape functions relate the displacements (or any other quantities) at any point within the element to the nodal displacements (or any other (a). Plane

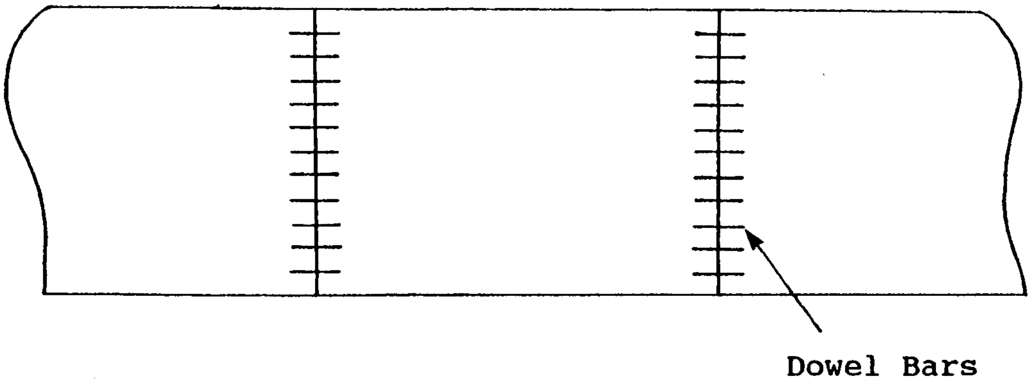

(b). Section

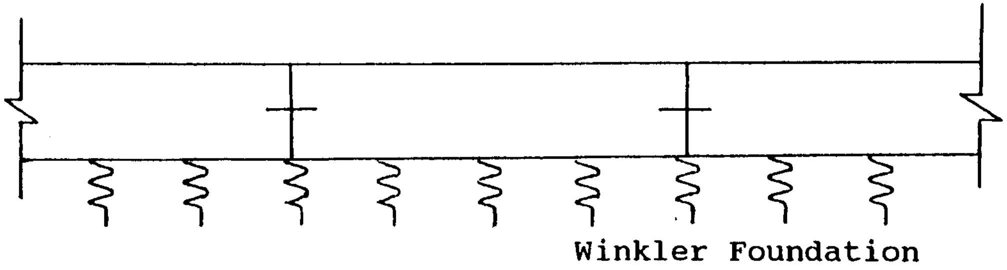

Figure D.1. Jointed concrete pavement model configuration.

quantities). One dimensional Lagrange functions can be written as

$$\begin{aligned} N_i\ (\xi)\big|_{i=1} &= \frac{1}{2}\ \xi\ (\xi - 1) \\ N_i\ (\xi)\big|_{i=2} &= 1 - \xi^2 \\ N_i\ (\xi)\big|_{i=3} &= \frac{1}{2}\ \xi\ (\xi + 1) \end{aligned} \tag{D.1}$$

$$\begin{aligned} N_j\ (\eta)\big|_{j=1} &= \frac{1}{2}\ \eta\ (\eta - 1) \\ N_j\ (\eta)\big|_{j=2} &= 1 - \eta^2 \\ N_j\ (\eta)\big|_{j=3} &= \frac{1}{2}\ \eta\ (\eta + 1) \end{aligned} \tag{D.2}$$

So, two dimensional Lagrange functions can be expressed as

$$N_I\ (\xi,\eta) = N_i(\xi)\ N_j(\eta) \tag{D.3}$$

The identification of i, j and node number I is shown in Table D.1. These shape functions are also used in isoparametric mapping. The mesh generation algorithm is based on the principle of isoparametric mapping.

Table D.1. The identification of i, j and node number I.

i	1	3	3	1	2	3	2	1	2
j	1	1	3	3	1	2	3	2	2
I	1	2	3	4	5	6	7	8	9

Winkler (Elastic) Foundation

The subbase and subgrade are assumed to be a Winkler foundation (Figure D.1 (b)) characterized by the composite modulus of subgrade reaction, k. The Winkler foundation is unable to transfer shear stresses which means that the reaction at any point under the slab (vertical pressure) is proportional only to the deflection of the slab at that point. In this work, the Winkler foundation is adopted for the foundation representation, mainly because of its ease of formulation.

Slab Element Stiffness

The element is formulated following Mindlin-Reissner thick plate theory, which assumes that a line that is straight and normal to the midsurface before loading is to remain straight but not necessarily normal to the midsurface after loading. For convenience of notation, it is assumed that all three degrees of freedom ω_I, θ_{xI} and θ_{yI}, shown in Figure D.3, are present at every node I. The shape functions N_I $(I = 1, 9)$ are used to interpolate ω, θ_x and θ_y from nodal values of these quantities, that is

$$\left\{ \begin{matrix} \omega \\ \theta_x \\ \theta_y \end{matrix} \right\} = \begin{bmatrix} N_1 & 0 & 0 & N_2 & 0 & 0 & \dots & N_9 & 0 & 0 \\ 0 & N_1 & 0 & 0 & N_2 & 0 & \dots & 0 & N_9 & 0 \\ 0 & 0 & N_1 & 0 & 0 & N_2 & \dots & 0 & 0 & N_9 \end{bmatrix}_{3 \times 27} \underset{\sim}{d} = \underset{\sim}{N}\underset{\sim}{d} \tag{D.4}$$

where

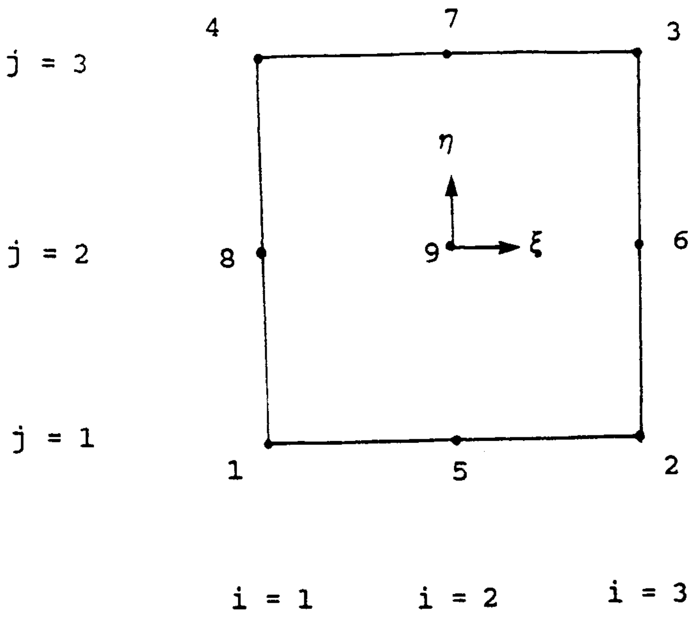

Figure D.2. 9-node quadratic element.

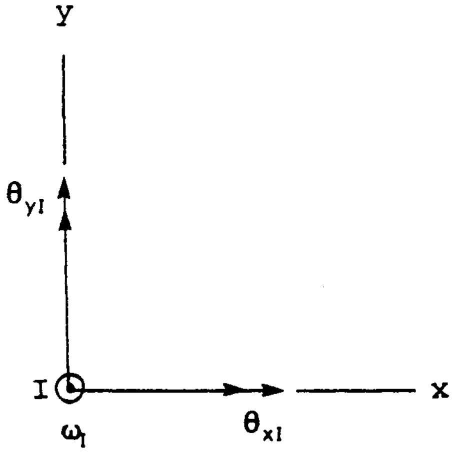

Figure D.3. Notation and sign convention for the degrees of freedom at a typical node I. The symbol ⊙ indicates an arrow directed out of the paper.

$$\underset{\sim}{d}^T = \left[\omega_1\ \ \theta_{x1}\ \ \theta_{y1}\ \ \omega_2\ \ \theta_{x2}\ \ \theta_{y2}\ \ \cdots\ \ \omega_9\ \ \theta_{x9}\ \ \theta_{y9}\right]_{1\times 27} \tag{D.5}$$

Curvatures and transverse shear strains can be written as

$$\underset{\sim}{\kappa} = \begin{Bmatrix} \kappa_x \\ \kappa_y \\ \kappa_{xy} \end{Bmatrix} = \begin{Bmatrix} \theta_{y,x} \\ -\theta_{x,y} \\ -\theta_{x,x} + \theta_{y,y} \end{Bmatrix} = \underset{\sim}{B_b}\ \underset{\sim}{d} \tag{D.6}$$

$$\underset{\sim}{\gamma} = \begin{Bmatrix} \gamma_x \\ \gamma_y \end{Bmatrix} = \begin{Bmatrix} \theta_y + \omega_{,x} \\ -\theta_x + \omega_{,y} \end{Bmatrix} = \underset{\sim}{B_s}\ \underset{\sim}{d} \tag{D.7}$$

where

$$\underset{\sim}{B_b} = \begin{bmatrix} 0 & 0 & N_{1,x} & 0 & 0 & N_{2,x} & \cdots & 0 & 0 & N_{9,x} \\ 0 & -N_{1,y} & 0 & 0 & -N_{2,y} & 0 & \cdots & 0 & -N_{9,y} & 0 \\ 0 & -N_{1,x} & N_{1,y} & 0 & -N_{2,x} & N_{2,y} & \cdots & 0 & -N_{9,x} & N_{9,y} \end{bmatrix}_{3\times 27} \tag{D.8}$$

$$\underset{\sim}{B_s} = \begin{bmatrix} N_{1,x} & 0 & N_1 & N_{2,x} & 0 & N_2 & \cdots & N_{9,x} & 0 & N_9 \\ N_{1,y} & -N_1 & 0 & N_{2,y} & -N_2 & 0 & \cdots & N_{9,y} & -N_9 & 0 \end{bmatrix}_{2\times 27} \tag{D.9}$$

The lateral displacement ω can be written as

$$\omega = \left[N_1\ \ 0\ \ 0\ \ N_2\ \ 0\ \ 0\ \ \ldots\ \ N_9\ \ 0\ \ 0\right]_{1\times 27}\ \underset{\sim}{d} = \underset{\sim}{N_\omega}\ \underset{\sim}{d} \tag{D.10}$$

The starting point for formulating an element stiffness matrix $\underset{\sim}{K}$ is an expression for strain energy U

$$U = \frac{1}{2}\int_A \underset{\sim}{\kappa}^T \underset{\sim}{D}_b \underset{\sim}{\kappa}\, dA + \frac{1}{2}\int_A \underset{\sim}{\gamma}^T \underset{\sim}{D}_s \underset{\sim}{\gamma}\, dA + \frac{1}{2}\int_A \omega\, k\, \omega\, dA \tag{D.11}$$

where the term $\frac{1}{2}\int_A \omega\, k\omega\, dA$ is the effect of the elastic foundation and A is the area of the element and matrices $\underset{\sim}{D}_b$ and $\underset{\sim}{D}_s$ are specified in the sequel. Substituting expressions (D.6), (D.7) and (D.10) into (D.11), then we get

$$\begin{aligned} U = {} & \frac{1}{2}\int_A \underset{\sim}{d}^T \underset{\sim}{B}_b^T \underset{\sim}{D}_b \underset{\sim}{B}_b \underset{\sim}{d}\, dA + \frac{1}{2}\int_A \underset{\sim}{d}^T \underset{\sim}{B}_s^T \underset{\sim}{D}_s \underset{\sim}{B}_s \underset{\sim}{d}\, dA \\ & + \frac{1}{2}\int_A \underset{\sim}{d}^T \underset{\sim}{N}_\omega^T\, k\, \underset{\sim}{N}_\omega \underset{\sim}{d}\, dA \end{aligned} \tag{D.12}$$

And finally, the element stiffness $\underset{\sim}{K}$ can be obtained

$$\underset{\sim}{K} = \underset{\sim}{K}_b + \underset{\sim}{K}_s + \underset{\sim}{K}_f \tag{D.13}$$

where $\underset{\sim}{K}_b$ is a bending stiffness, $\underset{\sim}{K}_s$ is a transverse shear stiffness and $\underset{\sim}{K}_f$ is a stiffness of the elastic foundation

$$\begin{aligned} \underset{\sim}{K}_b &= \int_A \underset{\sim}{B}_b^T \underset{\sim}{D}_b \underset{\sim}{B}_b\, dA \\ \underset{\sim}{K}_s &= \int_A \underset{\sim}{B}_s^T \underset{\sim}{D}_s \underset{\sim}{B}_s\, dA \\ \underset{\sim}{K}_f &= \int_A \underset{\sim}{N}_w^T\, k\, \underset{\sim}{N}_w\, dA \end{aligned} \tag{D.14}$$

where

$$\underset{\sim}{D}_b = \underset{\sim}{D} \int_{-h/2}^{h/2} z^2 \, dz = \frac{h^3}{12} \underset{\sim}{D} \tag{D.15}$$

$$\underset{\sim}{D}_s = \int_{-h/2}^{h/2} G \, dz \begin{bmatrix} 1 & 0 \\ 0 & 1 \end{bmatrix} = G \, h \begin{bmatrix} 1 & 0 \\ 0 & 1 \end{bmatrix} \tag{D.16}$$

$$\underset{\sim}{D} = \frac{E}{1 - \nu^2} \begin{bmatrix} 1 & \nu & 0 \\ \nu & 1 & 0 \\ 0 & 0 & \dfrac{1 - \nu}{2} \end{bmatrix} \tag{D.17}$$

$$G = \frac{E}{2 \, (1 + \nu)} \tag{D.18}$$

E is the Young's modulus, ν is the Possion's ratio and h is the thickness of the concrete slab.

The integral in (D.14) is evaluated by the reduced Gauss integration procedure using 2 × 2 integration points. The dowel bar element stiffness matrix and the modified dowel bar element stiffness matrix will be explained later.

Mass Matrix

The consistent nodal mass matrix is evaluated using the relationship

$$\underset{\sim}{M} = \underset{\sim}{M}_\omega + \underset{\sim}{M}_\theta = \rho h \int_A \underset{\sim}{N}_\omega^T \underset{\sim}{N}_\omega \, dA + \frac{\rho h^3}{12} \int_A \underset{\sim}{N}_\theta^T \underset{\sim}{N}_\theta \, dA \tag{D.19}$$

where ρ is a density of the concrete slab of the element. From expression (D.4), rotations can be expressed as

$$\left\{ \begin{matrix} \theta_x \\ \theta_y \end{matrix} \right\} = \underset{\sim}{N_\theta}\ \underset{\sim}{d} \tag{D.20}$$

where

$$\underset{\sim}{N_\theta} = \begin{bmatrix} 0 & N_1 & 0 & 0 & N_2 & 0 & \dots & 0 & N_9 & 0 \\ 0 & 0 & N_1 & 0 & 0 & N_2 & \dots & 0 & 0 & N_9 \end{bmatrix}_{2\times 27} \tag{D.21}$$

The integral in (D.19) is evaluated using the Gauss integration procedure with 2 × 2 integration points. To simplify calculations and to make the equations uncoupled, the mass matrix is reduced to the diagonal form by lumping the total mass of the element at the nodes in direct proportion of the diagonal terms. Dowel bar mass can be neglected, because it is so small.

Moments and Shear Forces

After knowing the displacements, curvatures and transverse shear strains can be easily found using Eqs.(D.6) and (D.7). Moments and shear forces can be found from the relations

$$\underset{\sim}{M} = \underset{\sim}{D_b}\ \underset{\sim}{\kappa} \quad , \qquad \underset{\sim}{Q} = \underset{\sim}{D_s}\ \underset{\sim}{\gamma} \tag{D.22}$$

Internal Force Vector

The internal force vector for each element can be evaluated using the relation

$$\underset{\sim}{f}^{int} = \int_A \underset{\sim}{B}_b^{\,T} \underset{\sim}{M}\, dA + \int_A \underset{\sim}{B}_s^{\,T} \underset{\sim}{Q}\, dA + \int_A \underset{\sim}{N}_\omega^{\,T} k\omega\, dA \tag{D.23}$$

where $\underset{\sim}{M}$ and $\underset{\sim}{Q}$ are obtained from equation (D.22).

The integral in (D.23) is evaluated by the reduced Gauss integration procedure using 2 × 2 integration points.

Force Equilibrium Equation

The basic equation solved in the analysis is the force equilibrium equation like Eq.(A.1), but here it does not include the damping term.

If d_n is known, the displacement vector at the next time step d_{n+1} can be calculated using the relationship

$$\underset{\sim}{d}_{n+1} = (\Delta t)^2 \underset{\sim}{M}^{-1} [\underset{\sim}{f}^{ext}(t_n) - \underset{\sim}{f}^{int}(\underset{\sim}{d}_n)] + \Delta t\, \dot{\underset{\sim}{d}}_{n-\frac{1}{2}} + \underset{\sim}{d}_n \tag{D.24}$$

DOWEL BAR AND SLAB INTERACTION ANALYSIS MODEL

Introduction

The dowel bar and slab interaction analysis model is illustrated in Figure D.4, where moment *M* and vertical force *F* are given. The objective of this model is to find out the relative deformations between dowel bars and the concrete slabs. This is a three-dimensional, linear and static problem.

3-node Dowel Bar Quadratic Element Stiffness Matrix

Dowel bar element is considered as a three-node, quadratic element shown in Figure D.5. $2L$ is the length of the dowel bar element, Coordinate ξ is a natural coordinate. Shape functions are same as Eq.(D.1), which are

$$\begin{aligned} N_1(\xi) &= \frac{1}{2}\xi(\xi - 1) \\ N_2(\xi) &= 1 - \xi^2 \\ N_3(\xi) &= \frac{1}{2}\xi(\xi + 1) \end{aligned} \tag{D.25}$$

The displacement V and the rotation θ are expressed as

$$\begin{aligned} V &= \sum_{I=1}^{3} V_I \, N_I(\xi) \\ \theta &= \sum_{I=1}^{3} \theta_I \, N_I(\xi) \end{aligned} \tag{D.26}$$

where V_I and θ_I are the displacement and rotation of node I (I = 1, 2, and 3). The curvature κ and the shear strain γ can be derived as

$$\begin{aligned} \kappa &= \theta_{,x} = \frac{1}{L}\,\theta_{,\xi} = \frac{1}{L}\sum_{I=1}^{3} \theta_I \, N_{I,\xi} \\ \gamma &= \theta + V_{,x} = \sum_{I=1}^{3} \theta_I \, N_I + \frac{1}{L}\sum_{I=1}^{3} V_I \, N_{I,\xi} \end{aligned} \tag{D.27}$$

In the matrix forms

$$\kappa = \underset{\sim}{B_b}\,\underset{\sim}{d} \quad , \qquad \gamma = \underset{\sim}{B_s}\,\underset{\sim}{d} \tag{D.28}$$

where

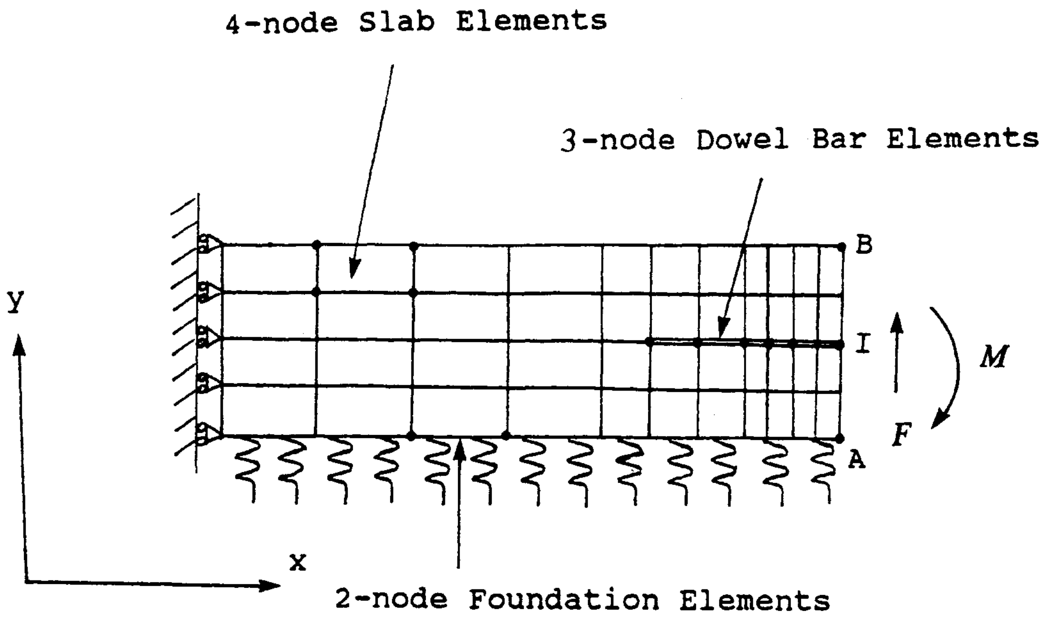

Figure D.4.. Dowel bar and slab interaction analysis model configuration.

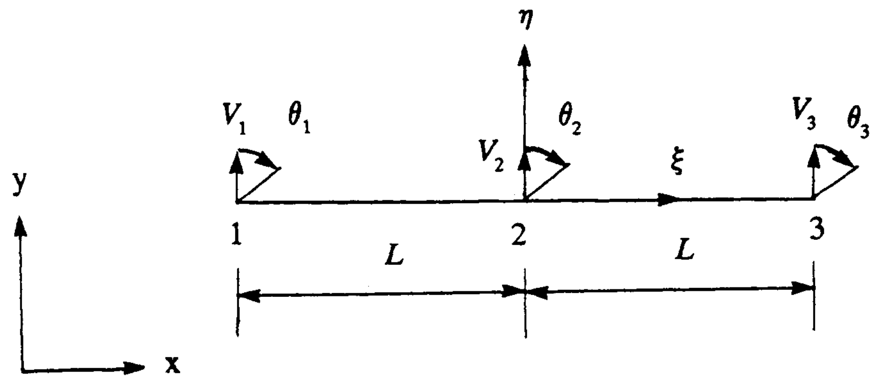

Figure D.5. Dowel bar element.

$$
\begin{aligned}
\underset{\sim}{B_b} &= \frac{1}{L}\begin{bmatrix} 0 & N_{1,\xi} & 0 & N_{2,\xi} & 0 & N_{3,\xi} \end{bmatrix} \\
\underset{\sim}{B_s} &= \begin{bmatrix} \frac{1}{L}N_{1,\xi} & N_1 & \frac{1}{L}N_{2,\xi} & N_2 & \frac{1}{L}N_{3,\xi} & N_3 \end{bmatrix} \\
\underset{\sim}{d}^T &= \begin{bmatrix} V_1 & \theta_1 & V_2 & \theta_2 & V_3 & \theta_3 \end{bmatrix}
\end{aligned}
\tag{D.29}
$$

The stiffness matrix for each dowel bar element is

$$
\underset{\sim}{K} = \underset{\sim}{K_b} + \underset{\sim}{K_s} \tag{D.30}
$$

where

$$
\begin{aligned}
\underset{\sim}{K_b} &= LEI \int_{-1}^{1} \underset{\sim}{B_b}^T \, \underset{\sim}{B_b} \, d\xi \\
\underset{\sim}{K_s} &= LGA \int_{-1}^{1} \underset{\sim}{B_s}^T \, \underset{\sim}{B_s} \, d\xi
\end{aligned}
\tag{D.31}
$$

where E is the Young's modulus, G is the shear modulus, I is the moment of inertia and A is the circular cross section area. The integration in (D.31) is evaluated by 3 Gauss integration points.

4-node Slab Element Stiffness Matrix

We assume that the displacements in slab are (Figure D.6)

$$
\begin{aligned}
u &= u(x,y,z) = \frac{1}{2}U(x,y)(1 + \cos\frac{\pi z}{C}) \\
v &= v(x,y,z) = \frac{1}{2}V(x,y)(1 + \cos\frac{\pi z}{C}) \\
w &= w(x,y,z) = W(x,y)\, \sin\frac{\pi z}{C}
\end{aligned}
\tag{D.32}
$$

where $-C < z < C$, C is the space between two dowel bars (usually 30 cm). The trigonometric approximation in the above equation is introduced to avoid consuming too much time for three-dimensional calculations of the problem. It is felt that this approximation should provide adequate representation of the phenomena. Fully three-dimensional finite element analysis, including interaction between dowel bars, is another alternative way to model this problem. The strains can be calculated as

$$\underset{\sim}{\epsilon} = \begin{Bmatrix} \epsilon_x \\ \epsilon_y \\ \epsilon_z \\ \gamma_{xy} \\ \gamma_{xz} \\ \gamma_{yz} \end{Bmatrix} = \begin{Bmatrix} u_{,x} \\ v_{,y} \\ w_{,z} \\ u_{,y} + v_{,x} \\ u_{,z} + w_{,x} \\ v_{,z} + w_{,y} \end{Bmatrix} = \begin{Bmatrix} \frac{1}{2}U_{,x}(1 + \cos\frac{\pi z}{C}) \\ \frac{1}{2}V_{,y}(1 + \cos\frac{\pi z}{C}) \\ \frac{\pi}{C}W \cos\frac{\pi z}{C} \\ \frac{1}{2}(U_{,y} + V_{,x})(1 + \cos\frac{\pi z}{C}) \\ (-\frac{\pi}{2C}U + W_{,x}) \sin\frac{\pi z}{C} \\ (-\frac{\pi}{2C}V + W_{,y}) \sin\frac{\pi z}{C} \end{Bmatrix} \qquad (D.33)$$

The displacements $U(x,y)$, $V(x, y)$ and $W(x, y)$ in the x, y plane can be interpolated from nodal values (Figure D.4)

$$\begin{aligned} U &= \sum_{I=1}^{4} U_I \, N_I(\xi,\eta) \\ V &= \sum_{I=1}^{4} V_I \, N_I(\xi,\eta) \\ W &= \sum_{I=1}^{4} W_I \, N_I(\xi,\eta) \end{aligned} \qquad (D.34)$$

where $N_I(\xi,\eta)$ (I = 1, 4) are the shape functions of the plane bilinear isoparametric element.

The individual shape functions are

$$\begin{aligned} N_1 &= \frac{1}{4}(1 - \xi)(1 - \eta) \qquad & N_2 &= \frac{1}{4}(1 + \xi)(1 - \eta) \\ N_3 &= \frac{1}{4}(1 + \xi)(1 + \eta) \qquad & N_4 &= \frac{1}{4}(1 - \xi)(1 + \eta) \end{aligned} \tag{D.35}$$

There are three degrees of freedom at node I, so the displacement vector at node I can be expressed as

$$\underset{\sim}{d}_I^{\,T} = \begin{bmatrix} U_I & V_I & W_I \end{bmatrix} \tag{D.36}$$

and there are 12 degrees of freedom on each element, so the displacement vector at each element can be written as

$$\underset{\sim}{d}^T = \begin{bmatrix} \underset{\sim}{d}_1^{\,T} & \underset{\sim}{d}_2^{\,T} & \underset{\sim}{d}_3^{\,T} & \underset{\sim}{d}_4^{\,T} \end{bmatrix} \tag{D.37}$$

The strains can be expressed in matrix form

$$\underset{\sim}{\epsilon} = \underset{\sim}{B}\underset{\sim}{d} \tag{D.38}$$

where

$$\underset{\sim 6 \times 12}{B} = \begin{bmatrix} \underset{\sim}{B}_1 & \underset{\sim}{B}_2 & \underset{\sim}{B}_3 & \underset{\sim}{B}_4 \end{bmatrix} \tag{D.39}$$

From (D.33) and (D.34),

$$\underset{\sim 6\times 3}{B_I} = \begin{bmatrix} \frac{1}{2}N_{I,x}\ (1+\cos\frac{\pi z}{C}) & 0 & 0 \\ 0 & \frac{1}{2}N_{I,y}\ (1+\cos\frac{\pi z}{C}) & 0 \\ 0 & 0 & \frac{\pi}{C}N_I\ \cos\frac{\pi z}{C} \\ \frac{1}{2}N_{I,y}\ (1+\cos\frac{\pi z}{C}) & \frac{1}{2}N_{I,x}\ (1+\cos\frac{\pi z}{C}) & 0 \\ -\frac{\pi}{2C}N_I\ \sin\frac{\pi z}{C} & 0 & N_{I,x}\ \sin\frac{\pi z}{C} \\ 0 & -\frac{\pi}{2C}N_I\ \sin\frac{\pi z}{C} & N_{I,y}\ \sin\frac{\pi z}{C} \end{bmatrix} \qquad (D.40)$$

The stiffness matrix of each element can calculated by

$$\underset{\sim 12\times 12}{K} = \int_A \int_{-C}^{C} \underset{\sim}{B}^T\ \underset{\sim}{D}\ \underset{\sim}{B}\ dz dA \qquad (D.41)$$

This integral can be evaluated analytically. $\underset{\sim}{D}$ (6×6) in (D.41) is a constitutive matrix representing material properties.

2-node Foundation Element Stiffness Matrix

One 2-node (node I and node J) foundation element is shown in Figure D.7. According to the assumption (D.32),

$$v(\xi,\eta,z) = \frac{1}{2}V(\xi,\eta)(1\ +\ \cos\frac{\pi z}{C}) \qquad (D.42)$$

The foundation element is on the foundation surface that makes contact with an element of slab, so $\eta = -1$, then

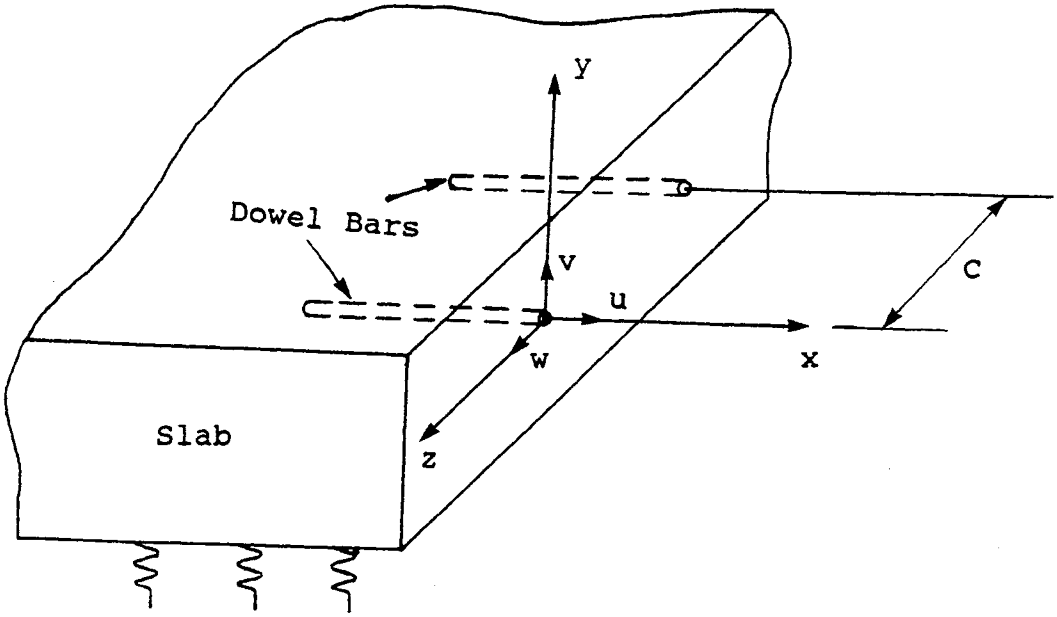

Figure D.6. Coordinate system and sign convention.

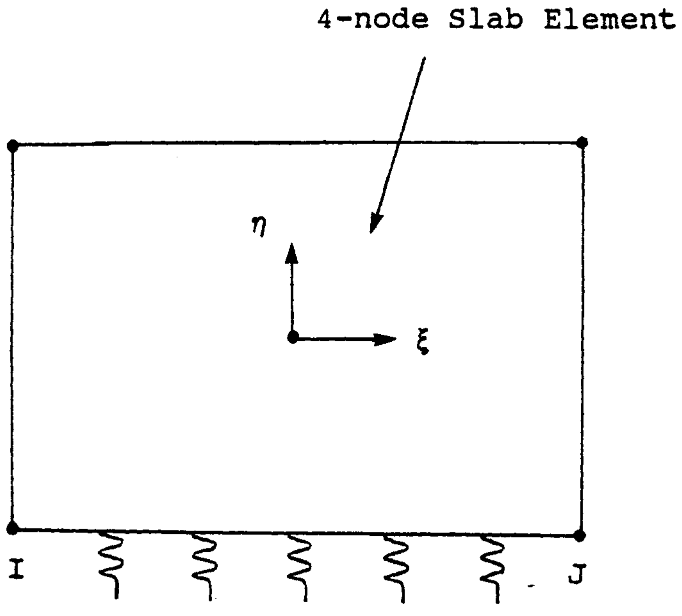

Figure D.7. 2-node foundation element.

$$v(\xi,-1,z) = \frac{1}{2}V(\xi,-1)(1 + \cos\frac{\pi z}{C}) \tag{D.43}$$

where

$$V(\xi,-1) = V_I\,\frac{1-\xi}{2} + V_J\,\frac{1+\xi}{2} \tag{D.44}$$

The Winkler foundation modulus is k, a vertical force is $-kv$ when deflected vertically an amount v. An increment of a work of the force in the foundation can be expressed as

$$\delta W = \int_{-C}^{C}\int_{-1}^{1} -kv\;\delta v\;\frac{L}{2}\;d\xi dz \tag{D.45}$$

Substituting (D.43) into (D.45), we obtain

$$\delta W = \delta \underset{\sim}{d}^{T}\;\underset{\sim}{K}\;\underset{\sim}{d} \tag{D.46}$$

where $\underset{\sim}{d}$ is a displacement vector, $\underset{\sim}{d}^{T} = \begin{bmatrix} V_I & V_J \end{bmatrix}$, $\underset{\sim}{K}$ is the foundation element stiffness, which is

$$\underset{\sim}{K} = \int_{-C}^{C}\int_{-1}^{1} -\frac{1}{16}k(1+\cos\frac{\pi z}{C})^{2} \begin{bmatrix} (1-\xi)^2 & 1-\xi^2 \\ 1-\xi^2 & (1+\xi)^2 \end{bmatrix} \frac{L}{2}\;d\xi dz \tag{D.47}$$

where L is a length of the element. This integration can be evaluated analytically.

DOWEL BAR ELEMENT STIFFNESS MATRIX

The 2-node (node I and node J) dowel bar element which connects two slabs is shown in Figure D.8.

2-node Dowel Bar (Beam) Element Stiffness Matrix

The dowel bar element between the slabs is considered as a two-node, isoparametric element shown in Figure D.9. L is the length of the dowel bar element, Coordinate ξ is a natural coordinate. The displacement V and the rotation θ are expressed as

$$\begin{aligned} V &= V_I(1-\xi) + V_J\,\xi \\ \theta &= \theta_I(1-\xi) + \theta_J\,\xi \end{aligned} \tag{D.48}$$

where V_I, θ_I and V_J, θ_J are the displacements and rotations of node I and node J respectively. The curvature κ and the shear strain γ can be derived as

$$\begin{aligned} \kappa &= \theta_{,x} = \frac{1}{L}\,\theta_{,\xi} = \frac{1}{L}(\theta_J - \theta_I) \\ \gamma &= \theta + V_{,x} = \theta_I(1-\xi) + \theta_J\,\xi + \frac{1}{L}(V_J - V_I) \end{aligned} \tag{D.49}$$

In the matrix forms

$$\kappa = \underset{\sim}{B}_b\,\underset{\sim}{d} \quad , \qquad \gamma = \underset{\sim}{B}_s\,\underset{\sim}{d} \tag{D.50}$$

where

$$\begin{aligned} \underset{\sim}{B}_b &= \frac{1}{L}\begin{bmatrix} 0 & -1 & 0 & 1 \end{bmatrix} \\ \underset{\sim}{B}_s &= \begin{bmatrix} -\frac{1}{L} & 1-\xi & \frac{1}{L} & \xi \end{bmatrix} \\ \underset{\sim}{d}^T &= \begin{bmatrix} V_I & \theta_I & V_J & \theta_J \end{bmatrix} \end{aligned} \tag{D.51}$$

The stiffness matrix for each dowel bar element is

$$\underset{\sim}{K} = \underset{\sim}{K}_b + \underset{\sim}{K}_s \tag{D.52}$$

where

$$\begin{aligned} \underset{\sim}{K_b} &= \int_0^1 \underset{\sim}{B_b}^T \, EI \, \underset{\sim}{B_b} \, L \, d\xi \\ \underset{\sim}{K_s} &= \int_0^1 \underset{\sim}{B_s}^T \, GA \, \underset{\sim}{B_s} \, L \, d\xi \end{aligned} \tag{D.53}$$

where E is the Young's modulus, G is the shear modulus, I is the moment of inertia and A is the circular cross section area. Substituting (D.51) into (D.53) and using reduced one Gauss point integration, we obtain

$$\underset{\sim}{K_b} = \frac{EI}{L} \begin{bmatrix} 0 & 0 & 0 & 0 \\ 0 & 1 & 0 & -1 \\ 0 & 0 & 0 & 0 \\ 0 & -1 & 0 & 1 \end{bmatrix} \tag{D.54}$$

$$\underset{\sim}{K_s} = LGA \begin{bmatrix} \frac{1}{L^2} & -\frac{1}{2L} & -\frac{1}{L^2} & -\frac{1}{2L} \\ -\frac{1}{2L} & \frac{1}{4} & \frac{1}{2L} & \frac{1}{4} \\ -\frac{1}{L^2} & \frac{1}{2L} & \frac{1}{L^2} & \frac{1}{2L} \\ -\frac{1}{2L} & \frac{1}{4} & \frac{1}{2}L & \frac{1}{4} \end{bmatrix} \tag{D.55}$$

2-node Modified Dowel Bar Element Stiffness Matrix

Using "dowel bar and slab interaction analysis model" (Figure D.4), some deformation relationships between dowel bar and concrete can be found.

According to the Mindlin-Reissner thick plate theory assumption, a straight line that is normal to the midsurface before loading is to remain straight after loading. As a measure of displacement and rotation of that line the following displacement V^c and rotation θ^c at node I are defined

$$V^c = \frac{V_A + V_B}{2} \quad , \quad \theta^c = \frac{U_A - U_B}{h} \tag{D.56}$$

where U_A, V_A, U_B and V_B are horizontal and vertical displacements at node A and node B, respectively.

The displacement V^d and rotation θ^d at node I of the dowel bar can be calculated when force F and moment M at node I are given and the displacement V^c and rotation θ^c at node I of the concrete are fixed. The following relationship can be found

$$\underset{\sim}{d}{}_I^{\,d} = \begin{Bmatrix} V^d \\ \theta^d \end{Bmatrix}_I = \begin{bmatrix} p_{11} & p_{12} \\ p_{21} & p_{22} \end{bmatrix}_I \begin{Bmatrix} F \\ M \end{Bmatrix}_I = \underset{\sim}{P}{}_I \, \underset{\sim}{F}{}_I \tag{D.57}$$

Similarly, the displacement $\bar{V}^d$ and rotation $\bar{\theta}^d$ at node I of the dowel bar can be calculated when force F and moment M at node I are zero and the displacement V^c and rotation θ^c at node I of the concrete are given. A similar relationship can be found

$$\underset{\sim}{\bar{d}}{}_I^{\,d} = \begin{Bmatrix} \bar{V}^d \\ \bar{\theta}^d \end{Bmatrix}_I = \begin{bmatrix} D_{11} & D_{12} \\ D_{21} & D_{22} \end{bmatrix}_I \begin{Bmatrix} V^c \\ \theta^c \end{Bmatrix}_I = \underset{\sim}{D}{}_I \, \underset{\sim}{d}{}_I^{\,c} \tag{D.58}$$

For node J (Figure D.8), we have similar relationships

$$\underset{\sim J}{d}{}^{d} = \begin{Bmatrix} V^{d} \\ \theta^{d} \end{Bmatrix}_{J} = \begin{bmatrix} p_{11} & -p_{12} \\ -p_{21} & p_{22} \end{bmatrix}_{J} \begin{Bmatrix} F \\ M \end{Bmatrix}_{J} = \underset{\sim J}{P}\;\underset{\sim J}{F} \tag{D.59}$$

$$\underset{\sim J}{\bar{d}}{}^{d} = \begin{Bmatrix} \bar{V}^{d} \\ \bar{\theta}^{d} \end{Bmatrix}_{J} = \begin{bmatrix} D_{11} & -D_{12} \\ -D_{21} & D_{22} \end{bmatrix}_{J} \begin{Bmatrix} V^{c} \\ \theta^{c} \end{Bmatrix}_{J} = \underset{\sim J}{D}\;\underset{\sim J}{d}{}^{c} \tag{D.60}$$

As shown in Figure D.10(a), the dowel bar itself will have displacement $\hat{V}^{d}$ and rotation $\hat{\theta}^{d}$ due to its own deformation under the force $-F$ and moment $-M$ at node I. In agreement with the linear approximation resulting in Eqs.(D.54) and (D.55) these are

$$\begin{Bmatrix} \hat{V}^{d} \\ \hat{\theta}^{d} \end{Bmatrix}_{I} = - \begin{bmatrix} \dfrac{GA}{L} & -\dfrac{GA}{2} \\ -\dfrac{GA}{2} & \dfrac{LGA}{4} + \dfrac{EI}{L} \end{bmatrix}^{-1} \begin{Bmatrix} F \\ M \end{Bmatrix}_{I} = \underset{\sim}{B}\,\underset{\sim I}{F} \tag{D.61}$$

The force F and moment M at node I and node J satisfy the equilibrium condition, so

$$\begin{Bmatrix} F \\ M \end{Bmatrix}_{J} = \begin{bmatrix} -1 & 0 \\ -L & -1 \end{bmatrix} \begin{Bmatrix} F \\ M \end{Bmatrix}_{I} \tag{D.62}$$

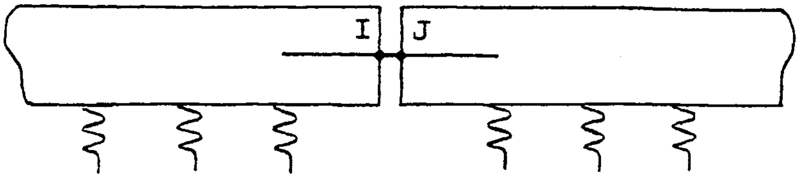

Figure D.8. Dowel bar element which connects two slabs.

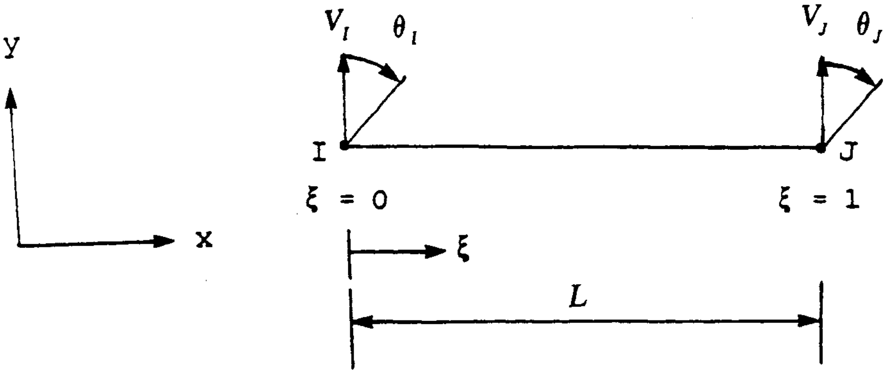

Figure D.9. 2-node dowel bar element.

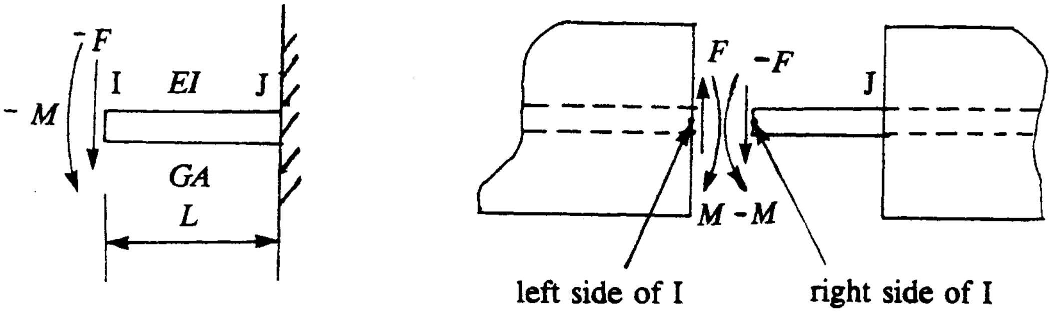

(a) (b)

Figure D.10. Analysis of forces applied on node I.

As shown in Figure D.10(b), the basic compatibility condition for the entire problem is that the displacements of left side of node I are equal to the right side of node I,

$$\begin{Bmatrix} V^d \\ \theta^d \end{Bmatrix}_I^{left} = \begin{Bmatrix} V^d \\ \theta^d \end{Bmatrix}_I^{right} \tag{D.63}$$

where

$$\begin{Bmatrix} V^d \\ \theta^d \end{Bmatrix}_I^{left} = \begin{Bmatrix} V^d \\ \theta^d \end{Bmatrix}_I + \begin{Bmatrix} \bar{V}^d \\ \bar{\theta}^d \end{Bmatrix}_I = \underset{\sim}{P}_I \underset{\sim}{F}_I + \underset{\sim}{D}_I \underset{\sim}{d}^c_I \tag{D.64}$$

$$\begin{aligned} \begin{Bmatrix} V^d \\ \theta^d \end{Bmatrix}_I^{right} &= \begin{Bmatrix} \hat{V}^d \\ \hat{\theta}^d \end{Bmatrix}_I + \begin{bmatrix} 1 & L \\ 0 & 1 \end{bmatrix} \left(\begin{Bmatrix} V^d \\ \theta^d \end{Bmatrix}_J + \begin{Bmatrix} \bar{V}^d \\ \bar{\theta}^d \end{Bmatrix}_J \right) \\ &= \underset{\sim}{B} \underset{\sim}{F}_I + \begin{bmatrix} 1 & L \\ 0 & 1 \end{bmatrix} \left(\underset{\sim}{P}_J \underset{\sim}{F}_J + \underset{\sim}{D}_J \underset{\sim}{d}^c_J \right) \\ &= \underset{\sim}{B} \underset{\sim}{F}_I + \underset{\sim}{\bar{P}}_J \underset{\sim}{F}_I + \underset{\sim}{\bar{D}}_J \underset{\sim}{d}^c_J \end{aligned} \tag{D.65}$$

where

$$\underset{\sim}{\bar{P}}_J = \begin{bmatrix} 1 & L \\ 0 & 1 \end{bmatrix} \underset{\sim}{P}_J \begin{bmatrix} -1 & 0 \\ -L & -1 \end{bmatrix} \tag{D.66}$$

$$\underset{\sim}{\bar{D}}_J = \begin{bmatrix} 1 & L \\ 0 & 1 \end{bmatrix} \underset{\sim}{D}_J \tag{D.67}$$

Substituting (D.64) and (D.65) into (D.63), we obtain

$$\underset{\sim}{F}_{I} = \underset{\sim}{A}^{-1} \begin{bmatrix} -\underset{\sim}{D}_{I} & \underset{\sim}{\bar{D}}_{J} \end{bmatrix} \begin{Bmatrix} \underset{\sim}{d}^{c}_{I} \\ \underset{\sim}{d}^{c}_{J} \end{Bmatrix} = \begin{bmatrix} -\underset{\sim}{S}_{I} & \underset{\sim}{S}_{J} \end{bmatrix} \begin{Bmatrix} \underset{\sim}{d}^{c}_{I} \\ \underset{\sim}{d}^{c}_{J} \end{Bmatrix}$$

where

$$\underset{\sim}{A} = \underset{\sim}{P}_{I} - \underset{\sim}{B} - \underset{\sim}{\bar{P}}_{J} \quad , \quad \underset{\sim}{S}_{I} = \underset{\sim}{A}^{-1} \underset{\sim}{D}_{I} \quad , \quad \underset{\sim}{S}_{J} = \underset{\sim}{A}^{-1} \underset{\sim}{\bar{D}}_{J} \tag{D.69}$$

Dowel bar strain energy can be expressed as

$$U = \frac{1}{2} \underset{\sim}{F}_{I}^{T} \begin{bmatrix} \frac{GA}{L} & -\frac{GA}{2} \\ -\frac{GA}{2} & \frac{LGA}{4} + \frac{EI}{L} \end{bmatrix}^{-1} \underset{\sim}{F}_{I} = \frac{1}{2} \underset{\sim}{F}_{I}^{T} \underset{\sim}{W} \underset{\sim}{F}_{I} \tag{D.70}$$

Substituting (D.68) into (D.70), then

$$U = \frac{1}{2} \underset{\sim}{d}^{cT} \begin{bmatrix} -\underset{\sim}{S}_{I}^{T} \\ \underset{\sim}{S}_{J}^{T} \end{bmatrix} \underset{\sim}{W} \begin{bmatrix} -\underset{\sim}{S}_{I} & \underset{\sim}{S}_{J} \end{bmatrix} \underset{\sim}{d}^{c} = \frac{1}{2} \underset{\sim}{d}^{cT} \underset{\sim}{\bar{K}} \underset{\sim}{d}^{c} \tag{D.71}$$

where

$$\underset{\sim}{d}^{c} = \begin{Bmatrix} \underset{\sim}{d}^{c}_{I} \\ \underset{\sim}{d}^{c}_{J} \end{Bmatrix} \tag{D.72}$$

From Eq.(D.71), it follows that the modified stiffness matrix $\bar{\underset{\sim}{K}}$ is

$$\bar{\underset{\sim}{K}} = \begin{bmatrix} \underset{\sim}{S}_I^T \, \underset{\sim}{W} \, \underset{\sim}{S}_I & -\underset{\sim}{S}_I^T \, \underset{\sim}{W} \, \underset{\sim}{S}_J \\ -\underset{\sim}{S}_J^T \, \underset{\sim}{W} \, \underset{\sim}{S}_I & \underset{\sim}{S}_J^T \, \underset{\sim}{W} \, \underset{\sim}{S}_J \end{bmatrix} \tag{D.73}$$